NATURAL CONVECTION AND RADIATION HEAT LOSS IN SOLAR CAVITY RECEIVERS – NUMERICAL MODELLING, PERFORMANCE ENHANCEMENT AND OPTIMISATION

by

Chabala Lloyd Ngo

Submitted in partial fulfilment of the requirements for the degree

Doctor of Philosophy in Engineering

in the

Faculty of Engineering, Built Environment and Information Technology

University of Pretoria
Pretoria

2016

ABSTRACT

TITLE: **NATURAL CONVECTION AND RADIATION HEAT LOSS IN SOLAR CAVITY RECEIVERS – NUMERICAL MODELLING, PERFORMANCE ENHANCEMENT AND OPTIMISATION**

AUTHOR: Chabala Lloyd Ngo

SUPERVISORS: Prof Tunde Bello-Ochende and Prof Josua P Meyer

DEPARTMENT: Mechanical and Aeronautical Engineering

UNIVERSITY: University of Pretoria

DEGREE: Doctor of Philosophy (Mechanical Engineering)

Energy access is increasingly seen as a vital catalyst to wider social and economic development, which enables education, health and sustainable agriculture, and creates jobs. Therefore, sustainable growth and development in society needs energy supply that is readily available, affordable, renewable and efficient without causing many negative societal impacts, such as environmental pollution and its consequences. In this regard, concentrating solar power technology has great potential to be used for energy production and it is a promising alternative to conventional fossil fuel-based energy technologies,

such as coal power plants, due to the abundance of solar energy as an energy resource, as well as its minimal impact on the environment. The parabolic dish receiver assembly is one such promising concentrating solar power technology. It usually consists of a reflector in the form of a dish with a downward-facing receiver at the focus of the dish. A cavity receiver is used to maximise the absorption of the concentrated flux. However, the receiver is subjected to environmental variations, as well as changes in receiver inclination angle, which lead to heat losses that affect the overall receiver's performance.

The need for the commercialisation of economically viable parabolic dish systems necessitates further in-depth investigation into cavity receiver designs. As the cavity receiver plays a critical role in transferring solar heat to the engine, any heat loss from the cavity receiver can significantly reduce the efficiency and, consequently, the system's cost effectiveness. It is therefore essential to assess and effectively minimise heat loss in the cavity receiver to improve the thermal performance of the system, which can contribute to the commercialisation of this type of technology.

The present study has therefore focused on developing novel approaches aimed at improving thermal performance for this type of concentrated solar thermal system through the reduction of heat loss in the cavity receiver.

This research focused on the modified cavity receivers that are employed in medium- and high-temperature solar dish systems with operating temperatures of up to 1 200 K. Firstly, a three-dimensional numerical investigation was conducted on a modified cavity receiver to quantify the natural convection heat loss, and to determine the effects of the operating temperature, receiver inclination angle and aperture size on heat loss. Furthermore, visualisation results, such as temperature contours, were presented to gain insight into the

effects of natural convection. The Boussinesq and non-Boussinesq fluid models were used in the numerical investigation and a comparison was made between them.

Secondly, a novel approach of suppressing natural convection heat loss in a cavity receiver was investigated. The proposed model has not been observed in literature. A cavity receiver with plate fins attached to the inner aperture surface was investigated as a possible low-cost means of suppressing natural convection heat loss in a cavity receiver. Employing air as the working fluid, laminar natural convection heat transfer from the cavity receiver with plate fins attached to the inner aperture surface was investigated for a range of Rayleigh numbers, inclination angles, and fin heights and thicknesses. Furthermore, visualisation results, such as fluid flow and temperature contours, were presented to gain insight into the suppression of natural convection. In addition, a numerical optimisation tool was used to select the best plate fin geometric configuration that improves cavity receiver performance at minimum natural convection heat loss.

Finally, a numerical study and optimisation of the combined laminar natural convection and surface radiation heat transfer in the cavity receiver with plate fins were conducted, and a three-dimensional simulation model was developed to estimate and optimise the convective and radiative heat loss. The influence of operating temperature, emissivity of the surface, orientation and the geometric parameters on total heat loss (convection and radiation) from the receiver were investigated. The results in steady state were obtained for a Rayleigh number range of 10^5 to 10^7. The overall thermal efficiency of the receiver was also analysed at different operating temperatures.

From this research, it can be concluded that there is a significant deviation between the Boussinesq and non-Boussinesq models of up to 20% at high temperatures. Therefore, natural convection at high temperature differences can accurately be predicted using the

non-Boussinesq model. It was also observed that a significant reduction in natural convection heat loss (up to 20%) from the cavity receiver can be achieved through plate fins, which act as heat suppressors. The results obtained provide a novel approach for improving the design of cavity receivers for optimal performance.

When natural convection was studied together with radiation, the overall cavity efficiency marginally increased by approximately 2% with the insertion of fin plates in the cavity receiver, although the convective heat loss was suppressed by about 20%. This is due to the fact that radiation heat loss dominates at high operating temperatures compared to convective heat loss.

Keywords: parabolic dish; cavity receiver; natural convection; radiation; plate fin; Rayleigh number.

DEDICATION

This thesis is dedicated to:

My daughters, Natasha Mapalo Ngo and Natwange Kunda Ngo.

ACKNOWLEDGEMENTS

I thank the Almighty God for His guidance and wisdom throughout the duration of this research.

This work is dedicated to my daughters, Natasha Ngo and Natwange Ngo, who were born during the course of my PhD studies. I hope this will be an inspiration to them and their siblings to achieve much more in their lives.

I wish to express my gratitude to my supervisor, Prof Tunde Bello-Ochende, for his technical guidance and support throughout the research work. My deepest thanks to my co-supervisor and Head of the Department of Mechanical and Aeronautical Engineering, Prof Josua P Meyer, for believing in me, and for his technical and financial support, which allowed the successful completion of this study.

I sincerely appreciate the efforts of the Thermofluids Research Group to make this work more fulfilling. My gratitude to all my fellow postgraduate colleagues in the Department of Mechanical and Aeronautical Engineering, as well as to senior students Lanre and Bode – who have since obtained their doctorates – for welcoming me. I also want to thank my colleagues, Aggrey, Jeff, Saheed, Jean-Mark, Willem, Noah and many others, as well as the departmental administrative officers, Tersia Evans, Elzabé Pieterse and Ntsindy Mnyamena.

I wish to thank my wife for her support and understanding during this period. To my parents, siblings, cousins, nephews and nieces, I thank you dearly for your love and moral support. You have been a source of joy and stability to me.

I thank my friends in Pretoria – Sidney Kabwe, Adam Kapata, Gabriel Mwanza, McDonnald Chimbeya, Alfred Chimbila, Dennis Sinkonde and their spouses, my cousin Kasonde and her husband Richard – for their consistent encouragement, as well as for their generous emotional support.

I would like to acknowledge the financial support of the University of Pretoria, the National Research Foundation (NRF), the Department of Science and Technology (DST) and the Solar Hub at Stellenbosch University.

I also wish to thank my employer, the University of Johannesburg, for allowing me study leave in the first semester to complete this thesis.

TABLE OF CONTENTS

LIST OF FIGURES

LIST OF TABLES

NOMENCLATURE

A	Surface of area, m^2
$ConstntViolation_j$	Amount by which the j-th constraint is violated
CO_2	Carbon dioxide
c_p	Specific heat capacity, J/Kg-K
D	Opening aperture diameter, m
D	cavity diameter, m
$\frac{du}{dy}$	Velocity gradient
dS	Elemental surface, m^2
E	Emissivity power vector
F	View factor
F_{peak}	Peak flux
$f(\mathbf{x})$	Objective function
$f(x^*)$	Lowest function value
g	Gravitational acceleration
$g_j(\mathbf{x})$	j-th inequality constraint function
Gr	Grashof number
h	Heat transfer coefficient, W/m^2-K
H	Fin height, m
H_j/W	Dimensionless height

J	Radiosity vector
$h_k(\mathbf{x})$	k-th equality constraint function
k	Thermal conductivity, W/m-K
K	$N \times N$ matrix
L	Characteristic length, m
L	Thickness, m
$Ncon$	Number of constraints
$Nobj$	Number of objectives
N_{rc}	Radiation-conduction number
Nu	Nusselt number
Obj_i	Response value for the i-th objective
Pr	Prandtl number
p	Pressure, Pa
P	Power, W
Q_c	Convection heat loss, W
$\dot{Q}_{cond}$	Heat transfer rate by conduction, W
$\dot{Q}_{conv}$	Heat transfer rate by convection, W
$\dot{Q}_{rad}$	Heat transfer rate by radiation, W
q	Energy flux, W/m^2
Ra	Rayleigh number
R	Surface resistance to radiation

S	Surface, m^2
S	Space between to two fins, m
S_i	i-th objective
T	Temperature, K
t	Fin thickness, m
t_j/W	Dimensionless thickness
$Trget_j$	Target value of the j-th constraint.
T_s	Surface temperature, K
T_∞	Ambient temperature, K
U_∞	Free stream velocity, m/s
V	Volume, m^3
$\mathbf{V}$	Velocity vector, m/s
$\mathbf{X}$	Mass force vector, N/kg
x_i	i-th design variable
x^*	Optimum vector
x,y,z	Cartesian coordinates, m
i,j,k,N	Positive integers

Greek symbols

α	Absorptivity
α	Thermal diffusivity, m^2/s

β	Angle, degree
β	Volume expansion coefficient, 1/K
∂	Differential operator or gradient function
σ	Stefan-Boltzmann constant ($W/m^2. K^4$)
ε	Emissivity
∇	Differential operator or gradient function
Δ	Difference
τ	Shear stress, N/m^2
μ	Dynamic viscosity, Pa-s
υ	Kinematic viscosity, m^2/s
η	Efficiency, %
ρ	Fluid density, kg/m^3
μ	Dynamic viscosity, kg/(m.s)
λ	Standard deviation
θ	Inclination angle, degree

Subscript

anal	Analytical
cond	Conduction
conv	Convection
c	Convection
D	Diameter, m

eff	Effective
exp	Experimental
num	Numerical
L	Length, m
min	Minimum
opt	Optimum
p	Pressure
rc	Radiation-conduction
Rad	Radiation
s	Surface
∞	Free stream
I,j,k,N	Positive integers

Superscripts

T	Transpose
N	Positive integer

Acronyms

ANU	Australia National University
BC	Before Christ
CAD	Computer-aided drawing
CFD	Computation Fluid Dynamics
CLFR	Compact linear Fresnel reflector
CPC	Compound parabolic concentrator
CPU	Computer processing unit
CSP	Concentrated solar power
GW	Gigawatts
HEEDS	Hierarchical Evolutionary Engineering Design System
HTF	Heat transfer fluid
IEA	International Energy Agency
K	Kelvin
kWh	Kilowatt hour
mb/d	Million barrels per day
MCRT	Monte Carlo Ray Tracing Method
MDGs	Millennium Development Goals
Na	Sodium
PDE	Partial differential equation
PV	Photovoltaic
Ra	Rayleigh number

RPC	Reticulate porous ceramic
SEGS	Solar Energy Generating Systems
SHERPA	Systematic Hybrid Exploration that is Robust, Progressive and Adaptive
S2S	Surface-to-surface
TFM	Transfer Function Method
TW	Terawatt
USA	United States of America

PUBLICATIONS IN JOURNALS AND CONFERENCE PROCEEDINGS

Articles in refereed journals

1. ***L. C. Ngo***, T. Bello-Ochende and J. P. Meyer, Numerical investigation of natural convection of cavity receiver for low-power application, (Accepted for publication in the special issue of *International Journal for Green Energy*) – accepted 4 August 2014.
2. ***L. C. Ngo,*** T. Bello-Ochende and J. P. Meyer, Numerical modelling and optimisation of natural convection heat loss suppression in a solar cavity receiver with plate fins. *Renewable Energy* 2015; 74: 95-105: doi:10.1016/j.renene.2014.07.047.
3. ***L. C. Ngo***, T. Bello-Ochende and J. P. Meyer, Three-dimensional analysis and numerical optimisation of combined natural convection and radiation heat loss in solar cavity receiver with plate fins insert. *Energy Conversion and Management Journal* 2015; 101: 757-766: doi: 10.1016/j.enconman.2015.05.061

Papers in refereed conference proceedings

1. ***L. C. Ngo***, T. Bello-Ochende and J. P. Meyer, Numerical investigation of natural convection of cavity receiver for low-power application, *Proceedings of the International Conference on Applied Energy* ICAE2013, Pretoria, South Africa, Jul 1–4, 2013.
2. ***L. C. Ngo,*** T. Bello-Ochende and J. P. Meyer, Numerical investigation of natural convection heat loss suppression in a solar cavity receiver with plate fins, *Proceedings of the 2nd Southern Africa Solar Energy Conference*, Port Elizabeth, South Africa, Jan 28–30, 2014.
3. ***L. C. Ngo,*** T. Bello-Ochende and J. P. Meyer, Numerical modelling of combined natural convection and surface radiation heat transfer in cavity receiver with plate fins, *Proceedings of International Heat Transfer Conference* (IHTC-15), Japan.
4. ***L. C. Ngo,*** T. Bello-Ochende and J. P. Meyer, Exergetic analysis and optimisation of a parabolic dish collector for low-power application, *Proceedings of the Centre for Renewable and Sustainable Energy Studies Symposium*, Stellenbosch, South Africa, Nov 22–23, 2012.

1

CHAPTER 1: INTRODUCTION

1.0 BACKGROUND

Despite the vast technological advances in today's world energy market, 1.3 billion people worldwide still do not have access to electricity and 2.6 billion people lack clean cooking facilities [1]. Africa is home to nearly half of those without access to electricity and one-quarter of those who rely on the traditional use of biomass for cooking [2]. Their chance to break out of poverty is severely constrained without modern energy services for productive uses, such as working, learning or operating a business.

Energy access is increasingly seen as a vital catalyst to wider social and economic development. It enables education, health and sustainable agriculture, and creates jobs. Energy for productive uses is particularly important to enable local business innovation and create a more vibrant economy for communities and countries, while providing societal benefits as well. Therefore, sustainable growth and development in society needs an energy supply that is readily available, affordable, renewable and efficient without causing many negative societal impacts, such as environmental pollution and its consequences. This can consequently contribute to achieving Sustainable Energy for All targets, which are essential to reach the Millennium Development Goals (MDGs), while growing our economies and safeguarding the environment [3].

Globally, most modern energy is obtained from fossil fuels (oil, coal and natural gas) with implications for the links between energy, the environment and climate change [1]. The share of fossil fuels in the global energy mix currently stands at 82%, which is as high as it was 25 years ago. According to the International Energy Agency (IEA), despite the sharp increase, the use of renewable energy sources will only reduce the share of fossil fuels in the energy mix to around 75% in 2035. Furthermore, the demand for oil and natural gas is set to grow by over 50% from 87.4 million barrels per day (mb/d) in 2011 to 99.7 mb/d in 2035. Consequently, the associated carbon dioxide (CO_2) emissions will more than double by the year 2050 [2].

It is evident that the cause of climatic change is CO_2. The burning of fossil fuels for the energy sector (power generation) and the transport sector contribute at least 90% of its emission [4]. It is undisputed that the continuous accumulation of CO_2 in the atmosphere is the cause of global temperature rise, the melting of the polar ice caps and the surge in the extreme weather events worldwide [4]. If not mitigated, the effects of climate change will result in increased risks, such as desertification, deforestation, flooding, water shortages and severe environmental pollution that are expected to cause an estimated 150 000 additional deaths every year [5].

For this reason, the issue of climate change has become a major issue of concern to governments, policy makers, researchers and environmentalists. This has led to an emphasis on the development of carbon-free energy sources that are environmentally friendly, sustainable and readily available to reduce the amount of pollutants that are

emitted into the atmosphere. However, despite the negative effects of fossil fuels on the environment, it is worth mentioning that their use has led to an incomparable rise in the standard of living, which has resulted in an increased life expectancy for part of the world's population [6].

Despite the dominance of fossil fuels, it is important to also note that the global energy mix is steadily changing with renewable energy becoming a greater part of it, especially in the power sector and in regions where measures have been put in place to encourage its deployment. The last decade has seen double digit growth rates for some renewable energy technologies and this is projected to grow strongly until 2035, as long as the necessary supporting measures remain in place [1]. However, the situation revolves around the three main energy uses: electricity, heat and transport, with electricity generation from renewable sources growing rapidly for most technologies, while renewable energy use for heat is growing more slowly and remains under-exploited. The IEA predicts that clean, sustainable energy sources will contribute about 50% of the new power infrastructures and, as such, renewable energy will become the world's second-largest source of power generation by 2015, contributing about 30% of the electricity requirements by the year 2035 [1].

Therefore, the drive today, is to seek sustainable development through the utilisation of energy sources that have little or no adverse impact on the environment [7]. These renewable energy sources are easily replenished once consumed, unlike finite fossil fuels.

The available renewable energy sources include solar energy, wind energy and geothermal energy.

Compared to other renewable energy sources, solar energy has great potential to be used for energy production and is a promising alternative to conventional fossil fuel-based energy technologies, such as coal power plants, due to its abundance, as well as its minimal impact on the environment. It is estimated that 1.75×10^5 TW of sunlight continuously strikes the earth's atmosphere. Assuming 60% transmittance through the atmospheric cloud cover, an estimated 1.05×10^5 TW reaches the earth's surface continuously. If the irradiance on only 1% of the earth's surface could be converted into electric energy with only 10% efficiency, it would provide a resource base of 105 TW, while the total global energy needs for 2050 are projected to be about 25 to 30 TW [8].

In terms of the impact on the environment, it is estimated that solar energy plants emit 15 to 20 g CO_2-equivalent/kWh of greenhouse gases, depending on site conditions and technology, which is much lower when compared to CO_2 emissions from fossil-fired plants, which are in the range of 400 to 1000 g/kWh [9].

1.1 SOLAR ENERGY CONVERSION

Solar energy is believed to be the oldest source of energy ever used, with drying food for preservation as the first known practical application [8]. The oldest known large-scale application can be traced back to Archimedes, the Greek mathematician and philosopher (287 to 212 BC). He was the first person to use mirrors to concentrate the sun's rays [8].

Solar energy can be converted into a useful form of energy through different types of solar energy systems. Figure 1.1 shows a block diagram of three of the most basic solar conversion system types. Figure 1.1 (a) shows that the solar resource is captured and converted into heat. The heat is then supplied to a demand for thermal energy (thermal load), such as hot water heating, house heating, or as heat for industrial processes. This type of configuration may or may not include thermal storage and usually includes an auxiliary source of energy so that the demand may be met during long periods with no sunshine [10].

On the other hand, if the demand that has to be met is electricity (an electrical load) rather than heat, two main methods can be used to convert solar energy into electricity. With the first method, concentrated solar power (CSP) concentrates solar energy and collects it as high temperature heat that is converted into electricity using a typical power plant or engine. With the other method, photovoltaic (PV) cells are used to convert solar energy directly into electricity. Figure 1.1 (b) illustrates the two methods schematically. This study focuses on CSP and further details are given in the subsequent sections.

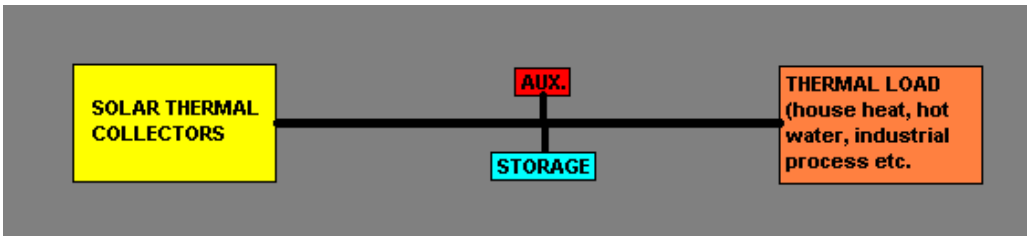

(a)

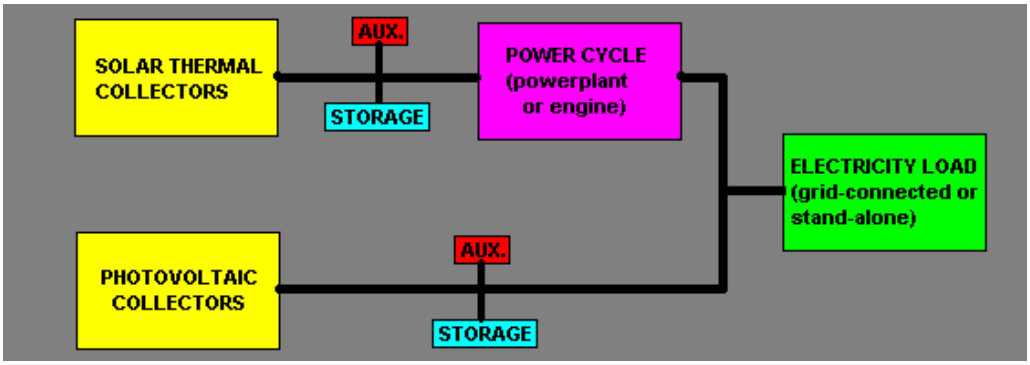

(b)

Figure 1.1: Diagrams of basic solar energy conversion systems. The AUX. box represents some auxiliary source of thermal or electrical energy [10]

1.2 CSP TECHNOLOGIES

There are four main competing CSP designs that have shown successful application either for demonstration projects or commercial purposes: parabolic trough, solar tower (also known as central receiver), linear Fresnel and parabolic dish/cavity systems. These designs are briefly discussed in the following sections.

1.2.1 Parabolic trough systems

Trough systems use linear parabolic concentrators to focus sunlight along the focal lines of the collectors and account for the largest CSP capacity worldwide. The parabolic trough technology employs long rows of single-axis sun-tracking parabolic concentrating

mirrors as shown in Figure 1.2. The mirrors focus and concentrate incident solar radiation on a linear heat-absorbing target (a receiver) that conveys a liquid heat transfer fluid. The fluid is heated as it flows through the receiver and is then used as a heat source for a power generation system. To reduce the convective heat losses from the heat collection element, an evacuated tube can be installed around the inner tube that contains the working fluid. Synthetic oils are commonly used as the heat transfer fluid due to their low freezing temperature (14 °C) and advantageous heat transfer properties [11].

Figure 1.2: 30 MW parabolic trough Solar Energy Generating Systems (SEGS) plant in Kramer Junction, California [11]

1.2.2 Linear Fresnel systems

Similar to the parabolic trough system, the linear Fresnel collector heats a linear receiver element that carries a liquid or gaseous heat transfer medium (usually water/steam). Instead of parabolic concentrators, the solar radiation is reflected by a series of parallel, long and flat mirrors that focus the radiation on a single line collector that is placed above

the mirror field as shown in Figure 1.3. It is estimated that linear Fresnel collector systems achieve only approximately 70% of the thermal efficiencies accomplished with parabolic trough systems. However, due to simpler component geometry and mechanics, the capital and operating costs are lower compared to the trough technology [11].

Figure 1.3: Compact linear Fresnel collector in Bakersfield, California by Ausra [11]

1.2.3 Central receiver systems

Solar tower power plants are in the class of central receiver systems that employ an elevated solar receiver, which is the focal point of a field of mirrors (heliostats). They concentrate the radiation onto the receiver's heat-absorbing surfaces, as shown in Figure 1.4. The receiver surface is usually constructed with welded absorber tubes that absorb the concentrated solar radiation from the heliostat field and transfer the absorbed thermal energy to a coolant that is pumped through the tubing system. The high-temperature heat

transfer fluid can then be used to drive a conventional power cycle or can be stored in tanks for later use [11].

Figure 1.4: Abengoa's PS10 11MW solar power tower in Sanlucar la Mayor, Spain [11]

1.2.4 Parabolic dish/receiver systems

Parabolic dish/receiver systems are compact CSP plants that use a concentrating surface ideally shaped like a paraboloid of revolution that focuses the solar radiation onto a receiver located at the focal point of the dish mirror as shown in Figure 1.5. The receiver transfers heat to an engine that converts the thermal energy to electrical energy [11]. Compared to the other CSP technologies, a parabolic dish receiver is a very promising system and is the focus of this study. It has demonstrated the highest efficiency, producing concentration ratios of more than 3 000 and operating at temperatures of more than 750 ^{o}C at annual efficiencies of 23% [12].

Figure 1.5: Parabolic dish systems at the Sandia Laboratory in Albuquerque, USA [11]

Due to their modular design, the systems provide flexibility for implementation in small-scale power generation, as well as utility-scale electricity generation when installed in a field arrangement with large numbers of dish receiver modules. Water is not required for the energy conversion process, in contrast to the conventional power cycles that are employed in the other CSP technologies. This is an advantage, especially in warm, arid areas that have a high solar irradiance throughout the year, but are also most suitable for CSP plants due to their low flora and population density. However, despite the high conversion efficiencies, the technology has not proven to be competitive and reliable for long-term operation and large-scale applications.

1.3 CSP TECHNOLOGY OUTLOOK

Currently, the deployment of CSP technology is growing more rapidly than any other renewable technology. This is because CSP offers an integrated solution to the coming

decade's global problems, including climate change and the associated shortages of energy and water [2], [13].

CSP-installed capacity was just 2.8 GW at the end of 2012, even though the first commercial plant started operating in 1986, and despite a wave of construction in Spain and the USA during the mid-2000s [13]. In the long run, the IEA estimates that CSP would need to meet 8 to 10% of the global electricity demand by 2050 if it is to contribute to the decarbonised energy system that is likely to limit the average global temperature increase to 2 ^{o}C [13].

The ability of CSP plants to store energy gives CSP a significant advantage over intermittent renewables. CSP with thermal storage avoids balancing needs and associated costs incurred by the solar PV and wind farms and can even act as a dispatchable plant to help integrate intermittent sources of supply [9], [13].

1.4 ANALYSIS OF A PARABOLIC DISH SYSTEM

The focus of this research is the parabolic dish/cavity system. The main components of a parabolic dish/cavity system (the concentrator/reflecting surface, tracking system, receiver and engine) are discussed.

Figure 1.6 illustrates the main components of a parabolic dish/receiver system.

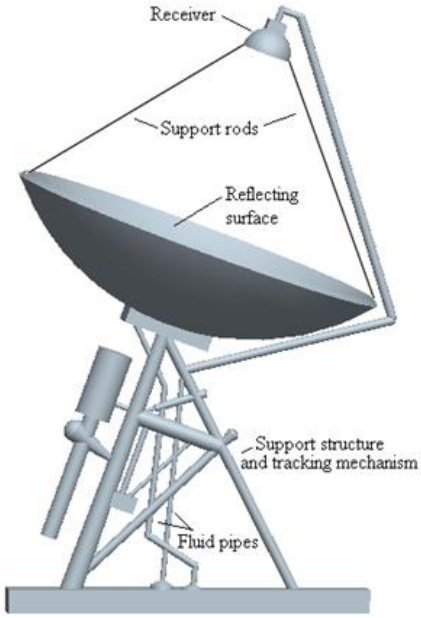

Figure 1.6: The main components of a parabolic/receiver system [14]

1.4.1 The concentrator/reflecting surface

The concentrator for the dish systems uses parabolic mirrors mounted on a structure that tracks the sun by pivoting on two axes [15]. The most durable mirror surfaces employ silver/glass mirrors and the solar reflectance of the silvered mirrors ranges between 91 and 95%. There have been attempts, but with limited success, to produce low-cost reflective polymer films. Stretched membranes are used in most of the innovative parabolic mirrors where the reflective membrane is stretched across a hoop or rim and a second membrane is placed behind the first. This creates a partial vacuum that pulls the first membrane into a parabolic shape [16].

To effectively capture the sun, the concentrator is designed with a tracking system. The dual-axis solar tracking of the parabolic dish system is accomplished through azimuth

elevation tracking or polar tracking. Azimuth elevation tracking rotates the concentrator in a plane parallel to the earth (azimuth) and in another plane perpendicular to the earth (elevation). For polar tracking, the concentrator rotates in a plane parallel to the rotation of the earth at a constant rate of 15° per hour, and the declination axis rotates perpendicularly to the polar axis by slowly varying between ±23.5° over the year. Larger dishes normally use azimuth elevation tracking, while smaller dish systems use polar tracking [15].

1.4.2 Cavity receiver

Two main types of receivers are used with parabolic solar concentrator systems: external (omni-directional) receivers and cavity (focal plane) receivers. External receivers are considered to be omni-directional receivers, since the absorbing surface is in direct view of the concentrator and depends on direct radiation absorption. For the capture of punctually concentrated sunlight, cavity receivers (as shown in Figure 1.7) are preferred in a parabolic dish solar thermal power system. This is due to their many advantages over other types of receivers, such as less thermal and optical losses, reduced direct heat flux density on the absorber, a nearly uniform internal wall temperature, steady thermal performance, high solar absorption efficiency, as well as low costs and maintenance fees [10].

Cavity receivers have an aperture through which the reflected solar radiation passes. The aperture in a receiver is located at the focal point of the parabolic concentrator to reduce radiation and convection losses. The aperture must be large enough to enable a significant

fraction of reflected radiation from the concentrator to be transmitted onto the absorber, although there is a drawback to designing it to be too large. Increasing the aperture size will increase the amount of solar radiation intercepted by the receiver, but will also increase losses due to convection and radiation out of the aperture [10].

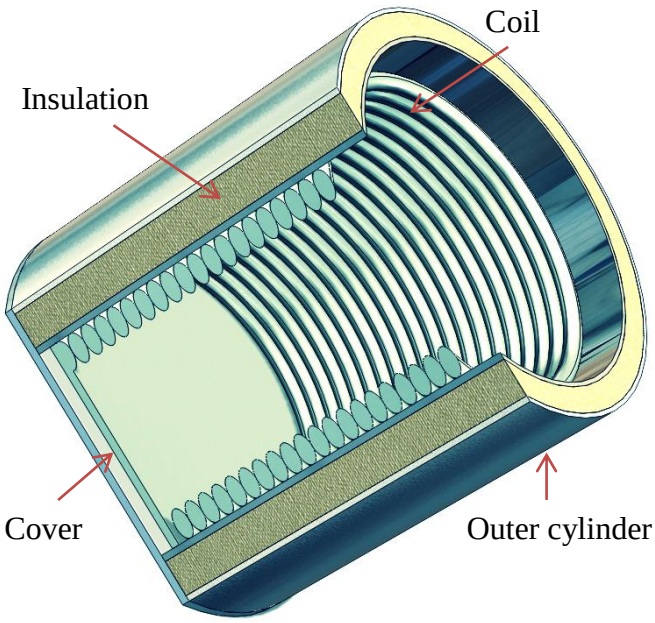

Figure 1.7: Cavity receiver [17]

Once inside the cavity, internal reflection ensures that the majority of the radiation that has entered the cavity is absorbed on the internal absorbing surface [10] and the absorbed thermal energy is transferred to the working fluid in the receiver.

1.4.3 Parabolic dish engine

In the parabolic dish systems, three main power cycles are used to produce electricity using concentrated solar thermal energy. These are the Rankine, Stirling and Brayton cycles [12]. The Brayton and Stirling engines provide high engine efficiencies, but are

limited by low gas heat transfer coefficients, which would require large receivers. The Rankine cycle allows for small receivers, which can use fluids with high heat transfer coefficients [18]. The parabolic concentrator is usually sized to deliver about four times more thermal energy than the rated electrical output due to an average net system efficiency of around 25% [19]. Existing parabolic dish systems have been built to provide 10 and 25 kW of electricity with the approximate diameter of the parabolic dish being 7.5 and 11 m respectively [20].

1.5 CAVITY RECEIVER LOSSES

The heat losses associated with the cavity receiver, a major component of a parabolic dish system, are discussed in this section. It has been established that the receiver is responsible for the majority of the thermal losses that occur before solar energy is converted into electricity in the parabolic dish system [21]. The thermal losses in the receiver are estimated to contribute about 51 to 76% of the total system losses [21]. These losses need to be reduced to enhance the performance of the system. Heat mechanisms that contribute to the total receiver thermal loss include conduction through the receiver housing, convection, and radiation through the aperture opening to the ambient environment. Figure 1.8 shows a schematic diagram of the energy balance with the loss mechanisms for a cavity receiver.

Conduction losses through the receiver housing represent a small fraction of the total receiver loss, natural convection losses represent about 40% of the receiver losses, and radiation is the primary receiver loss mechanism. Radiation represents the largest fraction

of receiver losses during mid-day periods when the receiver faces downward and convection losses are reduced, but convection can represent the majority of losses during the morning or evening when the aperture is oriented sideward [21].

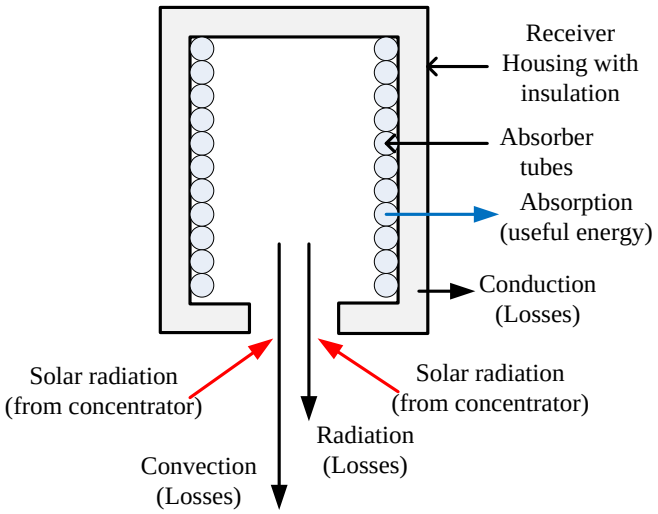

Figure 1.8: Receiver energy balance for a parabolic dish system

The radiation heat loss depends on the cavity wall temperature, the shape factors and the emissivity/absorptivity of the receiver walls, while conduction heat loss depends on the receiver wall temperature and the insulation material. However, heat loss occurs mainly through natural convection and surface radiation, since the cavity is insulated. As a result, it is very important to understand the behaviour of this type of heat transfer mechanism. With parabolic dish cavity receivers, conduction and radiation can readily be determined analytically [22].

On the other hand, determining convection heat loss is rather difficult due to the complexity of the temperature and velocity fields in and around the cavity. Successfully

determining the convection heat loss relies on semi-empirical models. Too many factors, such as the air temperature within the cavity, the inclination of the cavity, the external wind conditions and the cavity geometries, influence the convection heat loss of cavity receivers. In terms of cavity receiver geometry, the three most important features include the aperture diameter, cavity average diameter and cavity surface area. Natural convection and radiation heat losses in a cavity receiver are discussed in detail in this study.

1.6 MOTIVATION

The receiver plays an important role in transferring the concentrated solar heat to the engine in the parabolic dish system, and as such, heat losses from the receiver can significantly reduce the thermal performance and consequently the cost effectiveness of the system. It is therefore important to assess and subsequently improve the thermal performance of the receiver [23]. This necessitates further in-depth research into cavity receiver designs to understand and offer solutions aimed at improving the performance of parabolic dish systems. Heat loss reduction in the cavity receiver is seen as an effective way to improve the performance of a parabolic dish system and achieve commercialisation at low cost to compete favourably with fossil fuel-based technologies.

Some research has been done to predict heat losses in the cavity receiver, but very little has focused on reducing these losses to enhance the performance of this type of CSP. As a result, performance improvement of cavity receivers is still an open research area. The present study has therefore focused on developing novel approaches aimed at enhancing thermal performance and optimisation for this type of system through the reduction of

heat losses in the cavity receiver. Optimal system design can be achieved to help achieve the goal of parabolic dish system commercialisation.

Two primary approaches can be used to achieve this goal. The first would be to design, build and experimentally test systems to evaluate performance. The second would be simulation through numerical modelling.

The first approach usually yields useful and physically representative information of the phenomenon in the real system, but is costly and time consuming [7]. The modelling approach can provide much-needed insight into the phenomena that characterise cavity receivers at a reduced cost and time. In the research studies reported in this thesis, the numerical approach was used with the help of a unique combination of Computation Fluid Dynamics (CFD) code and a robust automated optimisation tool to gain deeper understanding of how cavity receiver parameters interact to improve overall performance. Few models have been developed in the past with the aim of enhancing the thermal performance of solar cavity receivers. This research is one of the efforts channelled in that direction by introducing a more novel approach coupled with optimisation techniques to improve the performance of cavity receivers.

1.7 OBJECTIVES

The main aim of this research is to investigate new approaches towards performance enhancement in cavity receivers through numerical modelling and optimisation. It is anticipated that this will provide insight into new approaches for solar cavity receiver

design technology. It is hoped that this information will be useful to improve cavity receiver performance and ultimately contribute to the commercialisation of this type of CSP technology. In order to realise the above mentioned aim, this study will focus on the following specific research activities:

- To numerically predict natural convection heat loss under different operating conditions using a CFD code taking into account the effects of the variation of air properties.

- To develop a novel design approach that can suppress natural convection heat loss, hence improving the performance of the cavity receiver, as well as to optimise the geometric parameters considered for maximum heat transfer suppression using an automated optimisation program with a search algorithm.

- To numerically predict and optimise combined natural convection and radiation heat losses in a cavity receiver with plate fins under different operating conditions, taking into account the effects of the variation of air properties.

- To carry out the numerical model validations on the investigated cavity receivers.

The attainment of these objectives will provide a comprehensive understanding of how different parameters interact to improve the performance of cavity receivers. In summary,

results from this study will lead to improved performance and the design information needed for solar cavity receiver manufacturers, which can be applied for better designs.

1.8 OUTLINE

The focus of this study was the modified cavity receiver proposed by Reddy and Sendhil Kumar [24]. It is employed in medium- and high-temperature solar dish systems with operating temperatures of up to 1 200 K. The thesis is presented in a multiple manuscript format for better organisation and readability. Chapters 5, 6 and 7 are written as individual research papers. The thesis consists of the following chapters:

Chapter 1 introduces solar energy technology and the importance of the study carried out in this thesis. It also includes the motivation and objectives of this study.

Chapter 2 discusses the literature review of pure natural convection heat transfer with and without radiation interaction inside a cavity receiver. It discusses the literature review of previous studies on the numerical, experimental and enhancement work of such cavity receivers.

Chapter 3 explains the theoretical background of natural convection heat transfer and radiation heat transfer as applicable to cavity receivers.

Chapter 4 explains the numerical model that was used for the cavity receiver and its governing equations and polynomials, which are used to account for air property

variations. Furthermore, the optimisation tool used for the optimisation part of this study is discussed in detail.

Chapter 5 deals with the three-dimensional numerical study of a modified cavity receiver on the effects of key operating parameters that impact on natural convection heat loss and the performance of solar cavity receivers. The parameters investigated are both design and physical parameters. This chapter also discusses the numerical results for both Boussinesq and non-Boussinesq models for pure natural convection.

Chapter 6 numerically investigates the natural convection heat loss from a cavity receiver with plate fins inserted in the surface of the cavity aperture. This is aimed at improving the system performance through the suppression of natural convection heat loss. A numerical optimisation tool (Optimate) is used with a CFD code to obtain the optimum parameters required to improve the cavity receiver's performance.

Chapter 7 numerically investigates and optimises the combined natural convection and radiation heat losses from a cavity receiver with plate fins inserted in the surface of the cavity aperture. The overall receiver efficiency is also estimated as a function of surface temperature and receiver aperture radius.

Chapter 8 summarises the important findings, the conclusions of this study and proposed future research.

2

CHAPTER 2: LITERATURE REVIEW

2.0 INTRODUCTION

In this section, a detailed literature review on past research investigations into cavity receiver heat loss and performance enhancement is performed. From the literature survey, it is evident that the type of cavity receivers that have been investigated both numerically and experimentally have been cylindrical, cubical, rectangular and hemispherical [23]. Most of these past studies investigated pure natural convection, while in reality heat transfer inside enclosed spaces occurs through a combination of natural convection and radiation. The following sections deal with specific literature relevant to pure natural convection heat transfer and combined natural convection and radiation heat transfer, in which related studies addressing the numerical, experimental and performance enhancement analysis of cavity receivers are discussed.

2.1 PURE NATURAL CONVECTION IN CAVITY RECEIVERS

Over the past decades, researchers have conducted both numerical and experimental investigations on natural convection heat transfer in cavities. With regard to the former, Le Quere, Humphery and Sherman [25] numerically analysed two-dimensional rectangular geometries with the aperture plane removed, and reported results for thermally driven laminar flow. Penot [26] numerically investigated natural convection

flow inside an isothermal open square cavity. The effects of the Grashof number and inclination of cavity were examined. Clausing [27], [28] and Clausing, Waldvogel and Lister [29] developed a model that was used to calculate the convection heat loss of a large cubical cavity. This model was based on the assumption that convection heat loss was governed by two factors: the ability to transfer mass and energy across the aperture, and the ability to heat air inside the cavity. Based on the above assumption, an analytical method was developed and it was concluded that the latter factor was of the greatest importance.

Harris and Lenz [30] investigated five cavity receivers with different geometries: cylindrical, conical, elliptical, heteroconical and spherical. They studied the thermal performance of these cavities and observed that the cavity geometry and rim angle have a substantial influence on the energy absorption efficiency. Siangsukone and Lovegrove [31] presented the work on modelling and simulation of the Australia National University (ANU) 400 m^2 parabolic dish concentrator system with a direct steam-generating cavity receiver and the steam line.

Sendhil Kumar and Reddy [32] investigated a two-dimensional cavity receiver based on the assumption of uniform and maximum solar distribution in the receiver. The results were presented in terms of Nusselt number correlations. Sendhil Kumar and Reddy [33] performed a comparative study to predict the natural convection heat loss from the cavity, modified cavity and semi-cavity receivers. A comparison of two- and three-dimensional natural convection heat loss from a modified cavity receiver was carried out by Reddy

and Sendhil Kumar [24]. Wu, Xiao and Li [34] performed a three-dimensional numerical study of a heat pipe receiver to investigate the influence of aperture size and position on natural convection heat loss, taking into account the effects of air property variation with temperature. Wu, Xiao, Cao and Li [23] summarised and presented a comprehensive review of the current research and progress on cavity receivers.

Paitoonsurikarn, Lovegrove, Hughes and Pye [35] numerically investigated natural convection heat loss from the cavity receivers of four different receiver geometries and validated the results using the published experimental results. They found some good agreement between the two results.

Xiao, Wu and Li [36] performed a three-dimensional numerical investigation to attain insight into the cavity aspect ratio on the natural convection heat loss of a cavity receiver for a high-temperature solar dish system. They proposed two correlations of Nusselt numbers by incorporating the cavity aspect ratio and the newly defined modified aperture ratio respectively.

Prakash, Kedare and Nayak [37] studied natural convection in three different cavity shapes: cubical, spherical and hemispherical with equal heat transfer areas. They observed that the spherical open cavity had the highest natural convection loss when compared to hemispherical and cubical shapes. Juárez, Hinojosa, Xamán and Tello [38] presented the numerical results of heat transfer calculations in an open cavity considering natural convection and temperature-dependent fluid properties.

With regard to experimental work, Pavlović and Penot [39] reported a detailed experimental study of heat transfer in an open isothermal cubic cavity for mixed natural and forced convection. This experimental study quantitatively confirmed the important influence of external flow on the heat transfer phenomenon in an open isothermal cubic cavity. A combined numerical and experimental study of natural convection in a side-facing open cavity was conducted by Skok, Ramadhyani and Schoenhals [40]. Numerical predictions that covered the Rayleigh number (Ra) range from 10^3 to 10^7 were in good agreement with experimental data for the back plate. It was underpredicted for the bottom plate and overpredicted for the top plate.

Prakash et al. [41] reported experimental and numerical studies of the steady-state convection heat losses that occurred from a downward-facing cylindrical cavity receiver. From all the data points, Nusselt number correlations, as a function of receiver aperture diameter, were proposed for natural convection heat losses. Prakash et al. [42] carried out experimental and numerical studies to identify the stagnation and convective zone in a downward-facing cylindrical cavity receiver. The effects of fluid inlet temperature and receiver inclination angle were investigated. It was observed that at 0^o inclination, convective zone covers the entire surface area of the receiver, while the percentage of the convective zone is the least at 90^o inclination.

Chakroun, Elsayed and Al-Fahed [43] carried out an experimental investigation to determine the heat transfer coefficient from a rectangular tilted cavity to the ambient environment due to the buoyancy-driven flow in the cavity. Taumoefolau and Lovegrove

[44] presented an experimental investigation based on an isothermal electrically heated model cavity receiver. The experimental system proved to be reliable and convection losses were determined with good accuracy.

Taumoefolau, Paitoonsurikarn, Hughes and Lovegrove [45] investigated the performance of cavity receivers using an electric heat source in their experiments. From this simple model, they were able to get accurate repeatable data of natural convection and established a relationship with the inclination of the receiver.

Reynolds, Jance, Behnia and Morrison [46] constructed an experimental apparatus to investigate heat transfer characteristics in a cavity with complex boundary conditions. They observed reasonable agreement between the experimentally determined heat losses and those predicted by the computational model. Melchior, Perkins, Weimer and Steinfeld [47] designed, fabricated and tested a lab-scale 5 kW prototype cylindrical cavity receiver and observed that the major heat losses were from re-radiation through the aperture and conduction through the reactor walls.

From their experimental investigations of a hemispherical cavity receiver with a diameter of 540 mm, Patil, Jahagirdar and Deore [48] observed that the heat loss was minimum at 90^{o} and maximum at 0^{o} inclination angles. An experimental investigation using an electrical heating method was carried out by Wu, Guan, Xiao, Shen and Xu [49] to explore the effects of surface boundary condition, tilt angle and heat flux on the heat loss of a fully open cylindrical cavity.

Zhang, Li, Wang, Chang and Liu [50] used the Transfer Function Method (TFM), a successful dynamic test method for solar collectors to estimate the outlet temperature of the molten salt cavity receiver. This was verified by indoor transient experiments. The results showed good agreement despite some errors.

2.2 COMBINED NATURAL CONVECTION AND RADIATION IN CAVITY RECEIVERS

Most of the past studies on cavities investigated pure natural convection, while in reality, heat transfer in cavities occurs through a combination of natural convection and radiation. Most studies on radiation heat transfer use thermal radiation, which is the form of radiation emitted by bodies because of their temperatures.

The thermal surface radiation occurs between two or more surfaces at different temperatures and it becomes extremely important if the temperature difference is high due to radiation's fourth-order dependence on temperature, which implies that radiation will dominate at high temperature differences. Both numerical and experimental investigations on combined natural convection and radiation heat transfer in cavities have been carried out by researchers. With regard to numerical studies, Lin, Ko and Xin [51] numerically investigated the steady turbulent-free convection in a two-dimensional open square cavity with and without surface radiation.

Balaji and Venkateshan [52] presented the results of a numerical study for natural convection in a square cavity. They emphasised the effects of surface radiation and

observed that calculations that included radiation heat transfer were more realistic, since it is impossible to have surfaces with zero emissivity in practice. Balaji and Venkateshan [53] presented numerical results on the influence of radiation on an open cavity. They observed that radiation enhanced the overall heat transfer significantly. Using a finite volume method, Balaji and Venkateshan [54] performed a numerical investigation of combined conduction, convection and radiation in a slot. From this study, they were able to demonstrate the importance of the conjugate coupling in determining the convective and radiative heat transfer rates. Singh and Venkateshan [55] reported results of a numerical study of steady combined laminar natural convection and surface radiation heat transfer for a two-dimensional open cavity using air as the fluid medium. They observed that surface radiation altered the flow patterns and the thermal performance significantly.

Hinojosa, Cabanillas, Alvarez and Estrada [56] conducted a numerical analysis of combined natural convection and surface thermal radiation in a tilted two-dimensional open cavity. They observed that cavity receiver inclination angle significantly influences the convective Nusselt number and not the radiation Nusselt number.

Hinojosa, Estrada, Cabanillas and Alvarez [57] used the Boussinesq approximation in the numerical study of natural convection and surface thermal radiation in an open cavity. Reddy and Sendhil Kumar [58] developed a two-dimensional simulation model for combined natural convection and surface radiation. They investigated the effects of operating temperature, emissivity of the surface, inclination and the geometry on the total heat loss from the cavity receiver of a solar parabolic dish collector. Using an asymptotic

CFD approach, Sendhil Kumar and Reddy [59] numerically investigated combined natural convection and radiation heat loss from the modified cavity receiver of a solar dish collector.

Gonzalez, Palafox and Estrada [60] presented numerical calculations for the heat transfer by natural convection and surface thermal radiation in a square open cavity receiver with large temperature differences and variable properties. They observed that radiative heat transfer is more important than convective heat transfer at larger temperature gradients.

Natarajan, Reddy and Mallick [61] presented a non-Boussinesq model for combined natural convection and surface radiation for a solar trapezoidal cavity absorber of a compact linear Fresnel reflector (CLFR). They studied the effects of the aspect ratio, absorber angle, Grashof number, surface emissivities and temperature ratio. They concluded that heat loss at a high receiver temperature can accurately be predicted using the non-Boussinesq model.

Wu, Guo and Xiao [62] presented a three-dimensional numerical investigation of combined natural convection and radiation heat losses in a cylindrical cavity with one open side and constant heat flux. They also considered conduction heat loss through insulation. Their numerical procedure was validated by their current experimental results.

Reddy and Ravi Kumar [63] carried out a two-dimensional numerical simulation of combined convective and radiative heat losses from the inverted trapezoidal cavity

receiver based on a non-Boussinesq approximation. They proposed an optimum configuration of the cavity receiver based on the numerical analysis.

In terms of experimental studies, Dehghan and Behnia [64] numerically and experimentally analysed the combined natural convection, conduction and radiation heat transfer in a discretely heated open-top cavity. A comparison of the numerical and experimental observations showed that the accurate prediction of the flow and thermal field is influenced by radiation heat transfer.

Ramesh and Merzkirch [65] experimentally studied the interaction of natural convection and surface radiation heat transfer on side-vented open cavities. They presented results that highlight the effect of interaction and concluded that the flow and temperature patterns were significantly influenced by the emissivity of the cavity wall.

2.3 CAVITY RECEIVER EFFICIENCY ENHANCEMENT AND PERFORMANCE

Minimising heat loss in cavity receivers is seen as an effective method to improve their thermal performance at low cost. Although some investigations have been reported on heat loss in cavity receivers, only a few studies have focused on their enhancement, performance and optimisation. Kribus, Doron, Rubin, Karni, Reuven, Duchan and Taragan [66] designed and demonstrated the operation of the multistage receiver under elevated temperatures, which divided the aperture into separate stages according to the irradiation distribution to achieve a high working temperature and thermal efficiency. Although the air exit temperatures reached up to 1000 ^{o}C in this test, they were able to

get much higher temperatures up to 1 200 ºC in their previous tests before the deterioration of the optical subsystem.

Hahm, Schmidt-Traub and Lebmann [67] fabricated a cone concentrator combined with a solar cavity receiver. They reported its performance and compared it to a single cavity receiver. They observed that the cone concentrator suffers from a high number of rejected rays if the exit aperture is too small. On the other hand, a larger exit aperture increases the thermal losses of the cavity. Therefore, optimum cone geometry has to be found.

Rubin, Karni and Kribus [68] designed a volumetric solar receiver, nicknamed Porcupine. They demonstrated Porcupine's ability to endure a concentrated solar flux of up to 4 MW/m^2 and produce exit working fluid temperatures of up to 940 ºC.

Reddy and Sendhil Kumar [69] performed a numerical analysis of the heat transfer behaviour of the modified cavity receiver with cone, compound parabolic concentrator (CPC) and trumpet reflectors. They observed a reduction in natural convection heat losses of 29.23%, 19.81% and 19.16% respectively, through the incorporation of reflectors in the modified cavity receiver for second-stage concentration.

Cui, He, Cheng and Li [70] presented a cavity receiver with a quartz glass cover for the dish concentrating system. They proposed using a quartz glass cover to separate the receiver cavity from the ambient air and its selective coating layer to intercept the infrared

radiation emitted from the inner surface of the cavity receiver, which greatly reduced the natural convection and surface radiation heat losses.

Montes, Rovira, Martinez-Val and Ramos [71] proposed a new design for the active absorber surface of cavity receivers with the fluid flow scheme based on vertical tubes. This new design optimises the heat transfer in the absorber surface and can provide uniform heat transfer fluid (HTF) at the receiver outlet.

Hischier, Hess, Lipiński, Modest and Steinfeld [72] proposed a novel receiver design for power generation via combined cycles, which consists of an annular reticulate porous ceramic (RPC) bounded by two concentric cylinders. They have reported results on the air outlet temperature of up 1000 °C and thermal efficiency of up to 78%.

Boerema, Morrison, Taylor and Rosengarten [73] developed a simple receiver model to establish the effects of the fluids' characteristics on receiver design and efficiency. They made a comparison between two HTFs, Hitec and liquid sodium (Na), based on their thermophysical properties to determine their suitability for use in high-temperature central receivers. They reported that liquid sodium will show greater potential as an alternative to molten salts in the future if its limitations can be overcome.

Behnia, Reizes and Davis [74] analysed a rectangular cavity filled with non-participating (transparent) fluid for radiation and natural convection heat transfer. They observed that

external convection tends to weaken the internal circulation, while radiation strengthens the flow.

Leibfried and Ortjohann [75] examined the spherical and hemispherical cavities, focusing on heat losses at different inclination angles. Based on the works of Stine and McDonald [76], they developed two algorithms that allowed the calculation of convective loss from upward-facing receivers.

The start-up thermal performance of a saturated steam solar cavity receiver with absorber tubes was numerically studied by Fang , Tu and Wei [77]. They used a six-sided prism solar cavity with inclined top and bottom faces. Three start-ups were studied and the aperture's energy need was calculated. They concluded that the convective heat loss is the most dominant at both the beginning of the start-up and at the end of the start-up, when compared to radiative heat loss. Ben-Zvi, Epstein and Segal [78] proposed and analysed a new hybrid concept for solar receivers comprising two parts: an external boiler for the steam and a cavity for the superheated steam. This novel arrangement allows high thermal efficiencies of up to 85% at the design point.

From their proposed silicon carbide receiver design, Neber and Lee [79] observed that decreasing aperture diameter requires higher concentrations to deliver a prescribed amount of power. The increased concentration increases receiver efficiency, which allows a higher optimal temperature to increase total efficiency.

Tu, Wei and Fang [80] numerically studied the thermal performance of a saturated water/steam solar cavity receiver with different depths. They concluded that there is a peak value of thermal efficiency as the receiver is stretched under the combined effect of reflective heat loss, radiative heat loss and convective heat loss. They also observed that when the receiver gets deeper, the distributions of the heat flux and wall temperature on the boiling panels are more uniform.

Cui, He, Cheng and Li [81] developed a new modelling coupling for the inhomogeneous radiation flux distribution for the dish receiver. They used the Monte Carlo Ray Tracing Method (MCRT) program to achieve the real heat flux distribution on the inner wall of the dish receiver. The simulation results showed that the heat transfer process is significantly influenced by the inhomogeneous heat flux boundary condition.

Zhilin, Yaoming, Deyou and Jun [82] reported the feasibility of a solar power tower system comprising a cavity air receiver. They discussed the simple method and adapted a process for the cavity receiver design. Yu, Wang and Xu [83] proposed an integrated receiver model to evaluate and simulate the dynamic process of the solar cavity receiver for the full range of operation conditions.

Fang, Wei, Dong and Wang [84] proposed a method for evaluating the thermal performance of a solar cavity receiver under windy conditions. They observed that the heat loss and air velocity of the solar cavity receiver were at their maximums when the wind came from the side of the receiver.

2.4 CONCLUSION

From the published literature, it is clear that some research has been done to predict the heat losses in cavity receivers, but very few have focused on the performance enhancement and optimisation of cavity receivers. As such, the performance improvement and optimisation of cavity receivers are still an open research area. The present study has therefore focused on developing novel approaches aimed at enhancing the thermal performance and optimisation of cavity receivers through the reduction of heat losses.

3

CHAPTER 3: THEORETICAL BACKGROUND

3.0 INTRODUCTION

The theoretical background of heat transfer mechanisms that contribute to the total cavity receiver thermal loss (convection heat transfer and radiation heat transfer) are discussed in this chapter. Although the total receiver heat loss also includes conduction through the receiver housing, it is not discussed in this study, since it is considered to be minimal as the receiver housing is normally insulated to reduce conduction losses.

3.1 CONVECTION HEAT TRANSFER

Convection heat transfer can be divided into two types according to the nature of flow. The first is called forced convection when the flow is driven by an external agent (pressure difference), such as a fan or a pump. The second is called free or natural convection and will be explained in detail in this study.

Equally, in a cavity receiver, convection heat transfer can be divided into natural convection due to buoyancy and forced convection driven by ambient winds. Convection driven by ambient winds has not been considered in this study. Natural convection flow is generated by density differences in different sections of a fluid.

This density difference, along with the effect of gravity, creates a buoyancy force that causes the heavier molecules in the fluid to move downward and the lighter molecules in the fluid to move upward, producing a buoyancy-driven flow. The density differences in natural convection flows may result from differences in temperature, the differences in the concentration of chemical species or the presence of multiple phases in the fluid. In the present study, only natural convection flows caused by a temperature difference are discussed.

To understand the physical nature of natural convection transport, the heat transfer from a heated vertical surface placed in an extensive quiescent medium at a uniform temperature, as shown in Figure 3.1, is considered.

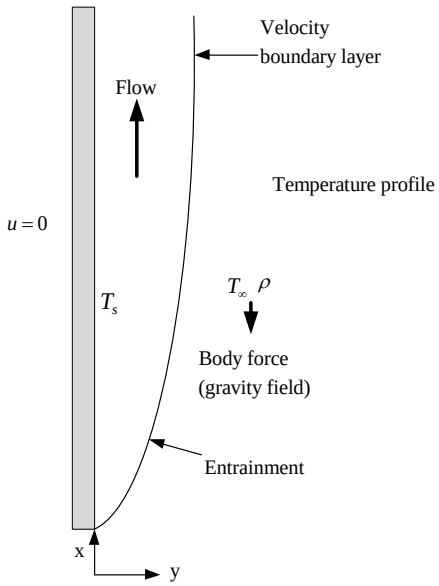

Figure 3.1: Natural convection flow over a vertical surface

If the plate surface temperature T_s is greater than the ambient temperature T_∞, the fluid adjacent to the vertical surface gets heated, becomes lighter (assuming that it expands when heated) and rises. Fluid from the neighbouring areas moves in due to the generated pressure differences to take the place of this rising fluid. Most fluids expand when heated, resulting in a decrease in density as the temperature increases. However, water between 0 and 4 °C is a notable exception. If the vertical surface is initially at temperature T_∞, and heat is turned on at a specific moment, say through an electric current, the flow undergoes a transient movement before the flow shown in Figure 3.1 is achieved. The analysis and study of this steady, time-dependent flow yields the desired information on the heat transfer rates, flow and temperature fields and other relevant process variables [85].

Convection heat transfer between a wall surface and a fluid can be calculated using Newton's Law of Cooling [86]:

$$\dot{Q}_{conv} = hA(T_s - T_\infty), \tag{3.1}$$

where $\dot{Q}_{conv}$ is the heat transfer rate by convection between the surface of area A at a temperature T_s and a fluid of temperature T_∞. The quantity h is called the convection heat transfer coefficient. The rate at which heat transfer is transported is controlled by the convective heat transfer coefficient. As such, it needs to be predicted accurately. The prediction of the convective heat transfer coefficient depends on the accurate evaluation of Nusselt number values. For some convection heat transfer systems, the convection heat

transfer coefficient can be calculated analytically, but the convection heat transfer coefficient must be determined experimentally or numerically for more complex systems [86].

3.1.1 Convection boundary layers

Theoretically, there are two boundary layers: the velocity and the temperature boundary layers. These boundary layers can be defined by considering the flow over a horizontal flat plate as shown in Figure 3.2. A flow region develops at the leading edge of the considered plate, where the effects of the viscous force are dominant. This effecting viscous force is a function of shear stress between fluid layers. This shear stress is proportional to the normal velocity gradient [86], [87].

$$\tau = \mu \frac{du}{dy} \tag{3.2}$$

where τ = shear stress

μ = dynamic viscosity

$\frac{du}{dy}$ = velocity gradient

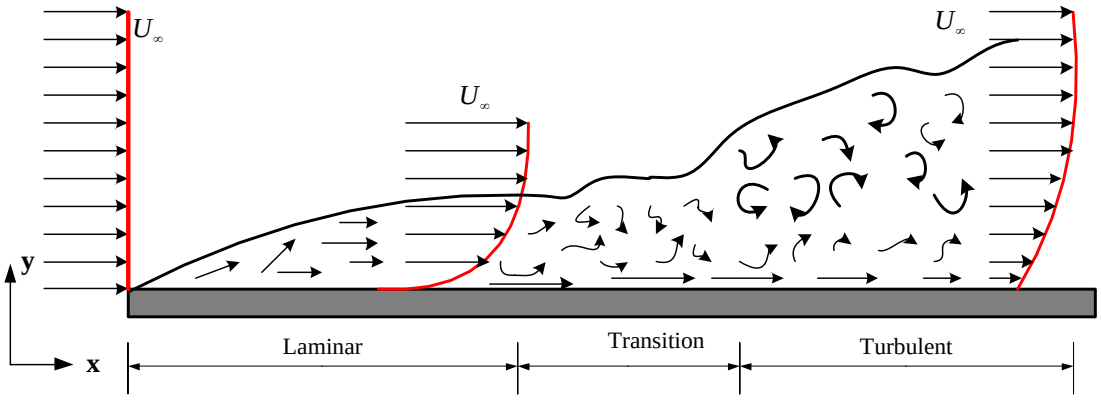

Figure 3.2: Velocity boundary layer development on a flat plate

The boundary layer is the region of the flow in which the effects of the viscosity start developing from the leading edge of the plate. This boundary layer ends at a distance on the y coordinate where the velocity becomes 99% of the free stream value U_∞.

The flow near the leading edge of the surface is laminar, as indicated by a well-ordered and well-layered flow, with no significant disturbance in Figure 3.2. However, as the flow proceeds horizontally downstream, it gets more disorderly and disturbed, because of flow instability, eventually becoming chaotic and random, a condition termed turbulent flow. The region between the laminar and turbulent flow regimes is termed the transition region. Its location and extent depend on several variables, such as the temperature of the surface, the fluid, as well as the nature and magnitude of external disturbances in the vicinity of the flow [85]. The transition from laminar to turbulent flow on a flat plate occurs [22] when the Reynolds number is:

$$Re_x = \frac{\rho u_\infty x}{\mu} > 5 \times 10^5 \tag{3.3}$$

where u_∞ = free stream velocity

x = distance from leading edge

ρ = fluid density

The thermal boundary layer develops when the plate surface temperature and the fluid free stream temperature are different. Also, it defines the region where the temperature gradients are present in the flow and the temperature gradients are caused by heat exchange between the plate surface and the fluid. The thermal boundary layer ends at a distance y, where $(T_s - T) = 0.99(T_s - T_\infty)$ [88].

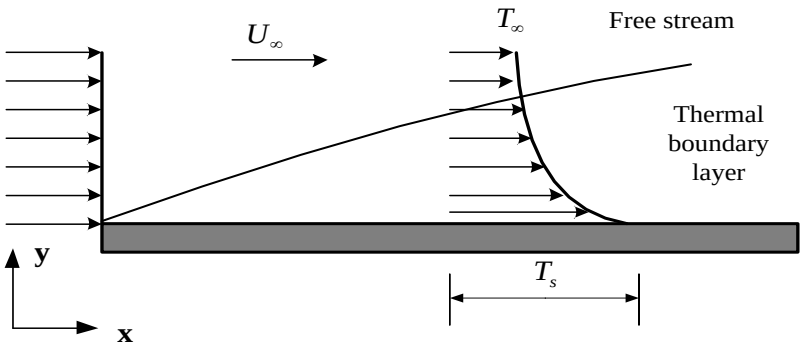

Figure 3.3: Thermal boundary layer development on an isothermal flat plate

The ratio between the thicknesses of velocity to thermal boundary layer is represented by the Prandtl number. Consider the flow over a flat plate as shown in Figure 3.3. Since the fluid motion becomes zero at the surface due to the no-slip condition, which is generally assumed to apply, the heat transfer from the heated surface to the fluid in its immediate vicinity is by conduction. It is therefore given by Fourier's Law as:

$$\dot{Q}_{cond} = -kA\frac{\partial T}{\partial y}\Big]_{surface} \tag{3.4}$$

Here the temperature gradient is evaluated at the surface (y = 0) in the fluid and k is the thermal conductivity of the fluid. From this equation, it is obvious that the natural convection flow largely affects the temperature gradient at the surface, since the remaining parameters remain essentially unaltered.

Convection heat transfer from the solid surface to the fluid is merely the conduction heat transfer from the solid surface to the fluid layer adjacent to the surface. Therefore, combining Equation 3.4 with Newton's Law (Equation 3.1) results in:

$$h = \frac{-k(\partial T/\partial y)_{surface}}{(T_s - T_\infty)} \tag{3.5}$$

To find the heat transfer coefficient, the temperature gradient at the plate surface needs to be found. This, in turn, depends on the nature and characteristics of the flow, temperature field and fluid properties. Generally, the convection heat coefficient varies along the flow (or x) direction. In such cases, the average or mean convection heat transfer coefficient for a surface is determined by properly averaging the local convection heat transfer coefficients over the entire surface [87].

3.1.2 Equations of motion for natural convection

From the physical mechanism of natural convection in a gravitational field, the buoyancy force exerted by the fluid on a body will be equal to the weight of the fluid displaced by the body [89].

$$F_{buoyance} = \rho_{fluid} g V_{body} \tag{3.6}$$

where ρ_{fluid} is the average fluid density, g is the gravitational acceleration and V_{body} is the volume of the body portion immersed in the fluid. The net force acting on this body will be [89]:

$$F_{net} = W - F_{buoyance} = \rho_{body} g V_{body} - \rho_{fluid} g V_{body} = (\rho_{body} - \rho_{fluid}) g V_{body} \tag{3.7}$$

The force shown in Equation 3.7 is proportional to the density difference of the fluid and the body immersed in this fluid. In heat transfer studies, however, the most important variable is the temperature, hence the buoyancy forces need to be expressed in terms of temperature difference, instead of density difference. The property, which represents the relation between temperature difference and density difference at constant pressure, is called the volume expansion coefficient β. This coefficient is defined as follows [85], [87]:

$$\beta = \frac{1}{v}\left(\frac{\partial v}{\partial T}\right) = -\frac{1}{\rho}\left(\frac{\partial \rho}{\partial T}\right)_P \tag{3.8}$$

The approximate value of this volumetric coefficient is produced by replacing the differential quantity by a difference quantity as in:

$$\beta \approx -\frac{1}{\rho}\frac{\Delta\rho}{\Delta T} = -\frac{1}{\rho}\frac{\rho_\infty - \rho}{T_\infty - T} \tag{3.9}$$

or

$$\rho_\infty - \rho = \rho\beta(T - T_\infty) \tag{3.10}$$

where ρ_∞ and T_∞ are the bulk density and temperature of the fluid respectively, which are measured far away from the surface so that these properties may not be affected by local conditions. For the perfect gas, $\beta = 1/T$, where T is the absolute temperature [85].

Considering a vertical hot plate immersed in a quiescent fluid body as shown in Figure 3.4 and assuming that the flow is steady and two-dimensional, and the fluid is Newtonian (with constant properties except for density), then the Boussinesq approximation for density can be applied.

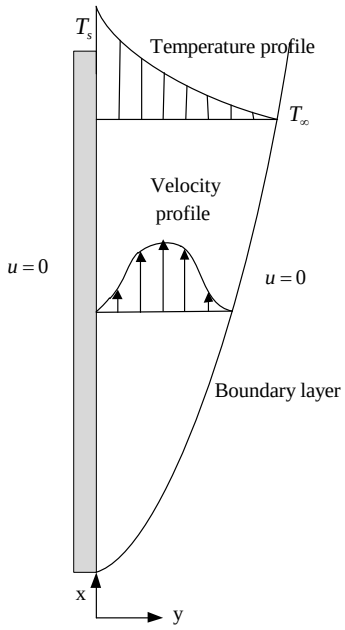

Figure 3.4: Natural convection over a vertical plate with temperature and velocity profile

The derivation of the equation of motion of the natural convection flow in the boundary layer based on the assumptions above is available in literature [87] and gives Equation 3.11:

$$u\frac{\partial u}{\partial x}+v\frac{\partial u}{\partial y}=v\frac{\partial u}{\partial y}.\frac{\partial u}{\partial y}+g\beta\left(T-T_\infty\right) \tag{3.11}$$

This momentum equation controls the fluid motion in the boundary layer due to the effect of buoyancy.

3.1.3 Dimensionless numbers

The governing equations in natural convection are normally non-dimensionalised and the variables are combined to produce non-dimensional numbers to reduce the total number

of variables. These parameters are not only important in simplifying the governing equations and the analysis, but also in guiding experiments that may be carried out to obtain the desired information on the process and in the presentation of the data for use in simulation, modelling and design [85].

3.1.3.1 Nusselt number

Consider the heat transfer from a fluid layer of side area A, a thickness L and a temperature difference between two sides of $\Delta T = T_1 - T_2$. If the fluid is moving, from Equation 3.1 the heat transfer by convection will be:

$$Q_{conv} = hA(T_1 - T_2) \tag{3.12}$$

If the fluid is motionless, the heat will be transferred by pure conduction according to this equation:

$$Q_{cond} = \frac{kA(T_1 - T_2)}{L} \tag{3.13}$$

The two equations can be non-dimensionalised by taking the ratio of the two equations:

$$\frac{Q_{conv}}{Q_{cond}} = \frac{\left[hA(T_1 - T_2)\right]}{\left[\frac{kA(T_1 - T_2)}{L}\right]} = \frac{hL}{k} = Nu \tag{3.14}$$

The dimensionless group that is produced is called the Nusselt number [87], which represents the enhancement of heat transfer through a fluid layer as a result of convection relative to conduction across the same fluid layer. That means that the larger the Nusselt number, the more effective the convection heat transfer [87]. Heat transfer across a fluid layer by pure conduction is represented by the Nusselt number equal to the unit.

3.1.3.2 Grashof number

The governing equations of natural convection heat transfer can be non-dimensionalised by employing the following dimensionless variable (indicated by asterisks). These constant quantities are [87]:

$$x^* = \frac{x}{L_c},\ y^* = \frac{y}{L_c},\ u^* = \frac{u}{V},\ v^* = \frac{v}{V},\ T^* = \frac{T - T_\infty}{T_s - T_\infty},\ \text{where } V = \frac{\mathrm{Re}_L\, v}{L} \tag{3.15}$$

Substituting these into the momentum Equation 3.11 and simplifying gives:

$$u^* \frac{\partial u^*}{\partial x^*} + v^* \frac{\partial u^*}{\partial y^*} = \frac{1}{Re_L} \frac{\partial^2 u^*}{\partial y^{*2}} + \left(\frac{g\beta(T_s - T_\infty)L^3}{\upsilon^2} \right) \frac{T^*}{Re_L} \tag{3.16}$$

where the dimensionless parameter shown between brackets is called the Grashof number Gr_L based on the characteristic length [85], [87].

$$Gr_L = \frac{g\beta(T_s - T_\infty)L^3}{\upsilon^2} \tag{3.17}$$

The Grashof number is the ratio between the buoyancy force and the viscous force, the magnitude of which allows the flow to be considered as laminar or turbulent. A large value of Gr, therefore, indicates small viscous effects in the momentum equation. The product of the Grashof number and Prandtl numbers is called the Ra [87]:

$$Ra_L = Gr_L Pr = \frac{g\beta(T_s - T_\infty)L^3}{\upsilon^2} Pr \tag{3.18}$$

where the Prandtl number is

$$Pr = \frac{\mu C_p}{k} = \frac{\nu}{\alpha} \tag{3.19}$$

The heat transfer inside enclosures depends strongly on the flow regimes and on the value of the Ra. The first flow regime is the conduction regime where heat is transferred by pure conduction. This regime occurs at a low Ra and obviously has a Nusselt number equal to unity. The second flow regime is the laminar regime. This occurs as the Ra increases, which causes large temperature gradients near the wall, indicating the growth of the boundary layers on the surfaces. Further increases of the Ra lead to unsteady motion, indicating the transition to turbulent regime. The transition from laminar to turbulent flow occurs when the Ra is greater than one million [84]. The Ra in natural convection is analogous to the Reynolds number in forced convection and is a measure by which the flow can be calculated as laminar or turbulent.

3.2 RADIATION HEAT TRANSFER

Radiation heat transfer or thermal radiation is the science of transferring energy in the form of electromagnetic waves. Unlike heat conduction and convection, radiation does not require the presence of a material medium to take place [85], [87]. The type of radiation heat transfer that is pertinent to heat transfer is thermal radiation, which is the form of radiation that is emitted by bodies because of their temperatures [87]. Thermal radiation is continuously emitted by all matter that has a temperature above absolute zero. The strength of this emission depends on the temperature of this body [86], [87]. The thermal surface radiation occurs between two or more surfaces at different temperatures and the amount emitted depends on the material of the body and the condition of its surface, as well as the temperature.

Therefore, radiation becomes extremely important if the temperature difference is high, due to radiation's fourth-order dependence on temperature, which implies that it will dominate at high temperature differences.

3.2.1 Radiation fundamentals

An idealised body, called a black body, serves as a standard against which radiative properties of real surfaces are compared. It is defined as a perfect emitter and absorber of radiation. A surface at an absolute temperature T_s emits a maximum rate of radiation according to the Stefan-Boltzmann Law as follows [87]:

$$\dot{Q}_{rad,\max} = \sigma A_s T_s^4 \tag{3.20}$$

where σ = 5.67 × 10^{-8} W/m^2. K^4 is the Stefan-Boltzmann constant, A_s is the surface area and T_s is the absolute surface temperature. The surface that emits this maximum rate of radiation as in Equation 3.20 is called a black body. According to Equation 3.21, all the other surfaces at the same temperature of the black body emit less radiation than the black body:

$$\dot{Q}_{rad} = \varepsilon \sigma A_s T_s^4 \tag{3.21}$$

where ε is the emissivity of the surface, and its value is in the range of $0 \leq \varepsilon \leq 1$. The emissivity value for the black body is ε = 1 and its value is less than 1 for the other surfaces. When radiation strikes a surface, part of it is absorbed, part of it is reflected and the remaining part, if any, is transmitted as shown in Figure 3.5. For opaque surfaces, such as those for metal, no part of the radiation is transmitted. The fraction that is absorbed by the surface is called the absorptivity α and its value is in the range of $0 \leq \alpha \leq 1$. If the black body absorptivity value is α = 1, it absorbs all the incident radiation on it. From Kirchhoff's Law, the emissivity and the absorptivity of a surface are equal at a given temperature and wavelength. Any surface, as shown in Figure 3.5, absorbs radiation according to the following equation:

$$\dot{Q}_{absorbed} = \alpha \dot{Q}_{incident} \tag{3.22}$$

where $\dot{Q}_{absorbed}$ is the portion of the heat that is absorbed by the surface and $\dot{Q}_{incident}$ is the incident heat radiation on this surface. A portion of the incident radiation is reflected back by the opaque surfaces as shown in Figure 3.5.

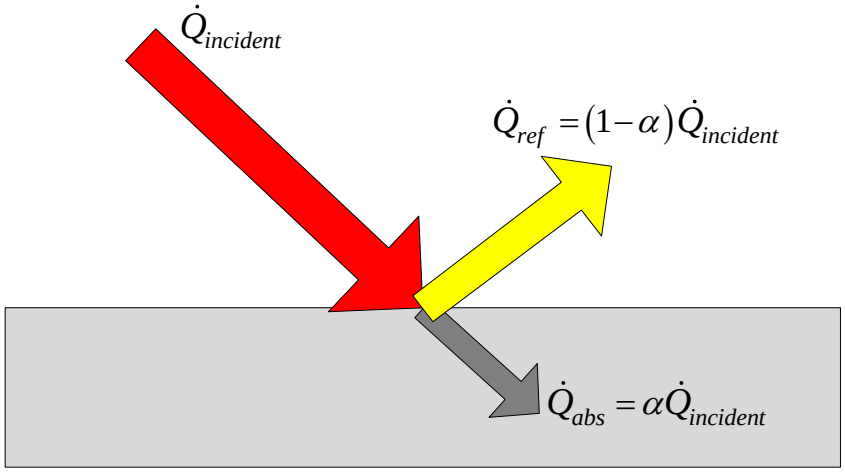

Figure 3.5: Incident, absorbed and reflected heat transfer on a surface of absorptivity α

Analysis of net radiation heat transfer between two surfaces is complicated, because it depends on many parameters, such as the properties of the surfaces, their location relative to each other and the interaction of the fluid between the two surfaces with radiation [86]. For example, when a surface of emissivity ε and surface area A_s at an absolute temperature T_s is completely enclosed by a large surface at absolute temperature T_∞ separated by a gas that does not intervene with radiation, as shown in Figure 3.6, the net radiation heat transfer between the two surfaces will be [86]:

$$\dot{Q}_{rad} = \varepsilon\sigma A_s (T_s^4 - T_{surr}^4) \tag{3.23}$$

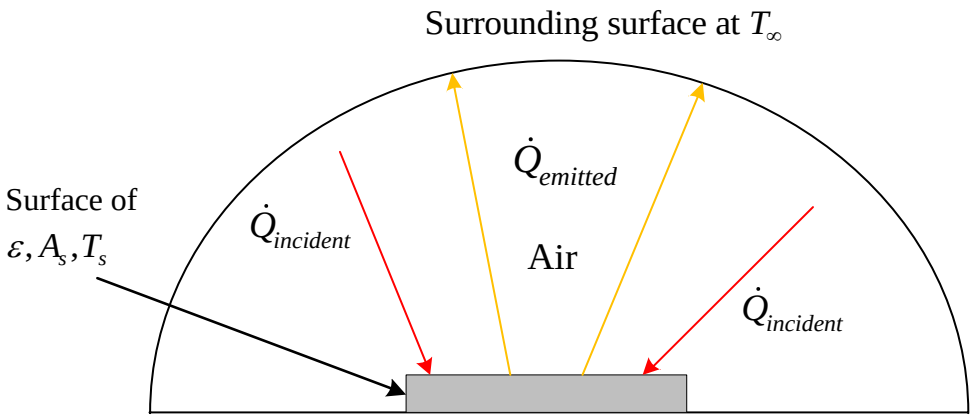

Figure 3.6: Heat transfer between two surfaces, one completely surrounding the other

3.2.2 The view factor

Radiation heat transfer between two surfaces depends on the radiation properties of the two surfaces. One of these properties is the orientation of the two surfaces relative to each other, as shown in Figure 3.7. To account for the effects of the orientation of the two surfaces relative to each other on the radiation heat transfer, a parameter called the view factor is defined. It is a purely geometric quantity and is independent of the temperature and the surface properties. The view factor is defined as the fraction of the radiation leaving Surface 1 to Surface 2 that strikes Surface 2 directly and is denoted by $F_{1\to 2}$ or just F_{12}, where F_{12} represents the fraction of radiation leaving Surface 1 that strikes Surface 2 directly.

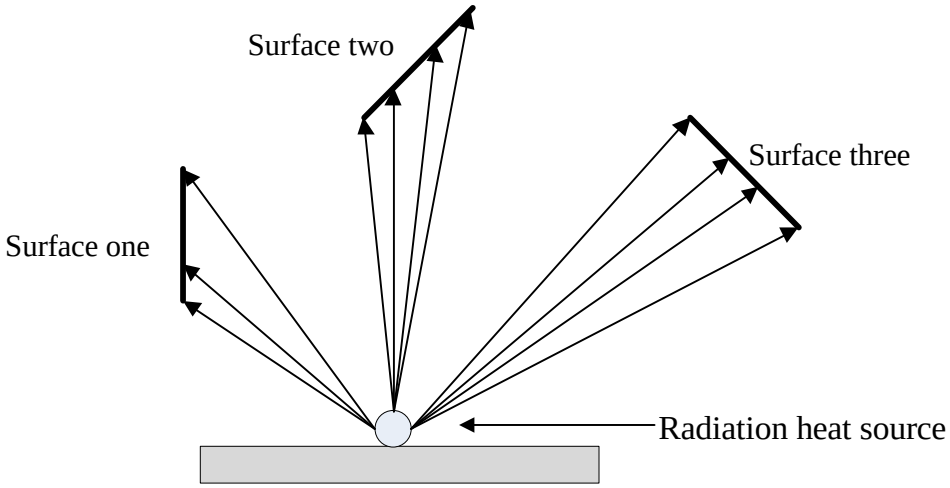

Figure 3.7: Radiation heat transfer depends on orientation between surfaces

The general expression for the view factor can be developed by considering two elemental surfaces dS_1 and dS_2 depicted in Figure 3.8.

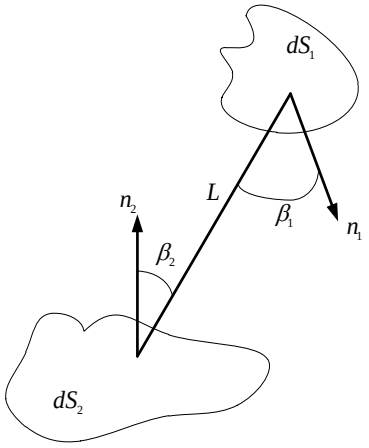

Figure 3.8: Radiation exchange between two elemental surfaces

Therefore, the view factor can be calculated using the following expression [90]:

$$F_{1-2} = \frac{1}{S_1} \iint_{S_1 S_2} \frac{\cos(\beta_1)\cos(\beta_2)}{\pi L^2} dS_1 dS_2 \tag{3.24}$$

$$F_{2-1} = \frac{1}{S_2} \iint_{S_1 S_2} \frac{\cos(\beta_1)\cos(\beta_2)}{\pi L^2} dS_1 dS_2 \quad \text{or} \quad F_{2-1} = F_{1-2}\frac{S_1}{S_2} \tag{3.25}$$

where L is the distance between dS_1 and dS_2, β_1 and β_2 are the angles between the normals of the two surfaces and the line that connects dS_1 and dS_2 respectively.

The following rules control the relation between view factors:

- The reciprocity rule $A_i F_{i\to j} = A_j F_{j\to i}$ (3.26)
- The summation rule $\sum_{j=1}^{N} F_{i\to j} = 1$ (3.27)
- The superposition rule $F_{1\to(2,3)} = F_{1\to 2} + F_{1\to 3}$ (3.28)
- The symmetry rule (if surfaces *j* and *k* are symmetric about the surface *i* then) $F_{i\to j} = F_{i\to k}$ (3.29)

The radiation heat transfer between two surfaces forming an enclosure can be calculated using the following equation:

$$\dot{Q}_{12} = \frac{\sigma(T_1^4 - T_2^4)}{R_1 + R_{12} + R_2} = \frac{\sigma(T_1^4 - T_2^4)}{\frac{1-\varepsilon_1}{A_1\varepsilon_1} + \frac{1}{A_1 F_{12}} + \frac{1-\varepsilon_2}{A_2\varepsilon_2}} \tag{3.30}$$

where the term $R_i = \frac{1-\varepsilon_i}{A_i\varepsilon_i}$ is the surface resistance to radiation and $R_{ij}\ \frac{1}{A_i F_{ij}}$ the space resistance to radiation.

3.3 CONCLUSION

In this chapter, the theoretical background of heat transfer mechanisms that contribute to the total cavity receiver thermal loss, namely convection heat transfer and radiation heat transfer, was discussed.

4

CHAPTER 4: NUMERICAL MODELLING FRAMEWORK

4.0 INTRODUCTION

In this chapter, the numerical and optimisation procedures employed in this research are presented. The results obtained by many researchers for the natural convection inside enclosed cavities are either by numerical modelling or by experimental methods. Numerical modelling has a certain advantage over experimental methods due to the flexibility for different geometries and boundary conditions. As such, it provides key benefits to cavity receiver designing.

Advances in numerical modelling in recent times have led to the development of more robust CFD. With the availability of CFD codes, it is now possible to perform an analysis on a series of parametric design variants until a satisfactory design criterion is obtained, thereafter prototype development can take place [7]. This has greatly reduced the lead time and cost in actual development procedures. A further improvement in the system design process is the use of optimisation tools. These tools can be used to overcome the problems of obtaining optimum design, which was previously largely constrained by the skill and experience of the modeller.

The combination of the CFD and optimisation tools can produce a great improvement in the design process, which makes it easy to obtain the generic information needed for a

better and more efficient design of the cavity receivers. This chapter presents a general overview of the numerical and optimisation techniques employed to study different cavity receiver models. However, further details regarding validation, grid independence and boundary conditions, as applied to the cavity receiver modelling problem in this study, are presented in chapters 5 to 7.

4.1 MATHEMATICAL MODEL

Natural convective heat transfer can be modelled mathematically by the set of governing equations derived from the conservation of mass, Newton's Second Law and the First Law of Thermodynamics. Application of these basic laws to an infinitesimal control volume, along with appropriate boundary conditions, gives a mathematical model of natural convection heat transfer that occurs in a cavity receiver. The resulting system of partial differential equations (PDEs), referred to as the Navier-Stokes equations, are shown below and solutions of these equations, including the energy equation, are required for the numerical analysis of laminar natural convection inside cavities.

Continuity equation:

The continuity equation is a differential equation that describes the conservation of mass. The general vector form of the continuity equation for a steady three-dimensional laminar flow is:

$$\nabla \cdot (\rho \mathbf{V}) = 0 \tag{4.1}$$

Momentum equation:

From Newton's Second Law, the rate of change of momentum of a fluid particle equals the sum of the forces on the particle. In this case, the general vector form of the momentum equation for a laminar flow is:

$$V \cdot \nabla(\rho \mathbf{V}) = \rho \mathbf{X} - \nabla p + \nabla^2(\mu \mathbf{V}) \tag{4.2}$$

Energy equation:

From the First Law of Thermodynamics, the rate of change of energy of a fluid particle is equal to the rate of heat addition to the fluid particle plus the rate of work done on the particle. The energy equation can be derived from this. In the case of laminar heat transfer, the general vector form of the energy equation is:

$$\mathbf{V} \cdot \nabla(\rho c_p T) = \nabla^2(kT) \tag{4.3}$$

where ρ is the density of air in kg/m^3, $\mathbf{V}$ is the velocity vector of air in m/s, $\mathbf{X}$ is the mass force vector in N/kg, p is the pressure, Pa, μ is dynamic viscosity in kg/(m.s), c_p is the specific heat capacity at constant pressure in J/(kg.K), k is thermal conductivity of air in W/(m.K) and T is temperature in Kelvin (K).

In natural convection, the buoyancy term in the Navier-Stoke equations is the key source term. Because rigorous mathematical models aimed at describing natural convection in open cavities are complex, most authors have used the so-called Boussinesq approximation to predict the fluid motion and heat transfer behaviour inside the cavity. This is the most extreme simplification and assumes that all physical properties are neither temperature nor pressure dependent, except for the density in the buoyance.

The Boussinesq approximation is known to provide good accuracy when the temperature difference between the hot wall and the ambient fluid ΔT is small. However, for large ΔT values, such as those found in solar concentrator receivers, the validity of the Boussinesq approximation is still uncertain [38]. For example, when the air temperature rises from the ambient temperature of 300 K to the receiver's operating temperature of 1000 K, air density decreases by 77.72%, thermal conductivity increases by 780.76%, and kinematic viscosity increases by 252.95%. These significant changes in physical air properties definitely have a crucial influence on natural convection heat transfer. Therefore, for large temperature differences, the Boussinesq assumption is not acceptable and the variations of the thermal properties (including density) with temperature in all terms of the governing equations should be taken into account [91]. In this study, polynomial relationships (equations 4.4 to 4.7) for density, specific heat capacity at constant pressure, dynamic viscosity and thermal conductivity are used to account for air property variation with temperature [92].

$$\rho = 7.4992\times10^{-9}T^{3} + 1.6487\times10^{-5}T^{2} - 1.2366\times10^{-2}T + 3.6508 \quad (4.4)$$

$$c_p = 1.3864\times10^{-13}T^4 - 6.4747\times10^{-10}T^3 + 1.0234\times10^{-6}T^2 - 4.3282\times10^{-4}T + 1.0613 \quad (4.5)$$

$$\mu = 1.3864\times10^{-15}T^3 - 1.4346\times10^{-11}T^2 + 5.0523\times10^{-8}T + 4.1130\times10^{-6} \quad (4.6)$$

$$k = 1.5797\times10^{-17}T^5 + 9.4600\times10^{-14}T^4 + 2.2012\times10^{-10}T^2 - 2.3758\times10^{-7}T^2 + 1.7082\times10^{-4}T^2 - 7.488\times10^{-3} \quad (4.7)$$

4.1.1 Thermal radiation model

The surface-to-surface (S2S) model that is coupled with the laminar natural convection model is used to account for the radiation exchange in the surfaces of the cavity receiver. In the S2S radiation model, the medium (air in this case) that fills the space between the surfaces is considered as non-participating. That is, it does not absorb, emit or scatter radiation. Under these circumstances, the radiation properties and the thermal boundary conditions that are imposed on each surface uniquely define the amount of radiation that a surface receives and emits. The surface properties are quantified in terms of emissivity, reflectivity, transmissivity and radiation temperature.

The S2S radiation model is based on enclosure theory as described in detail by Siegel and Howel [93] and [86].The net radiant flux on each surface is a function of the surface properties and the thermal boundary conditions that are imposed on that surface, and is calculated so that radiation is balanced. The radiation balance is enforced on the entire closed set of surfaces by considering each surface and how it exchanges radiation with

all other surfaces. Therefore, the first step in the model is to compute the surface-to-surface interaction for each surface pair.

The surfaces in the model may have either diffuse or specular surface properties. The surface emissivity is assumed to be diffuse, but the reflectivity may be either diffuse or specular. Specular properties are considered in the calculation of the view factors. The amount of radiation that is exchanged between surfaces depends on the emission from the surfaces, the position and orientation of the surfaces relative to each other, and on the presence of reflective surfaces that may alter the transfer between the surfaces. The view factors account for geometry and specular properties. The view factor is calculated using equations 3.24 or 3.25, as defined in Section 3.2.2.

In STAR-CCM+, the boundary surfaces are discretised into smaller elements called patches. These are sets of contiguous boundary cell faces, and view factors are calculated for each patch pair. By definition, patches do not straddle boundaries and are therefore at most as large as an entire boundary or as small as a boundary cell face. The emissive power (and therefore the radiation intensity) and radiation properties are assumed to be uniform over the surface of each patch [90].

The view factors as in equations 3.24 and 3.25 are purely topological quantities and depend only on the geometry of the two surfaces. However, the presence of partially specular reflective surfaces may introduce a further dependence on other surfaces and their respective surface properties. As a result, the collection of view factors generally depends on the surface geometry and the specular reflectivity of those surfaces. For a

fixed geometry and fixed surface specular reflectivity, the view factors must be obtained only once, usually at the start of a simulation.

4.2 NUMERICAL METHOD

Two numerical approximation techniques are usually utilised to obtain the solutions to the governing equations described in Section 4.1. One of them is the finite element method based on the Galerkin weighted residual function and the other is the finite volume method.

The finite element method divides the continuous problem domain described by governing partial differential equations into discrete problem subdomains, which have simple geometric shapes (called finite elements), for which it is possible to systematically generate the approximation functions needed in the solution of partial differential equations by the weighted residual method. The resulting systems of equations obtained from this discretisation are then assembled into a global system of equations, which is a set of linear algebraic equations and has the matrix form that is ready to be solved by efficient matrix inversion algorithms. One of the benefits of the finite element method is that it can solve problems with complicated geometry and properties.

In the finite volume method, the domain is divided into small volumes and the governing differential equations are integrated over these volumes. Compared with the finite element method, the finite volume method is more efficient computationally. It is also more universal and robust than the finite difference method as it poses a very low

requirement on domain geometry and flow condition. For this reason, the finite volume method is widely adopted as the generic flow solver.

The numerical study in this thesis was conducted by using the finite volume method with the help of a commercial CFD code, STARCCM+® [90]. The CFD code has an add-on package for optimisation. The detailed analysis of the numerical modelling techniques will be discussed in subsequent sections.

4.2.1 Numerical modelling procedures

The governing sets of mathematical equations that describe the flow field in the modelled cavity receiver are based on fundamental fluid dynamics principles, mass conservation, conservation of momentum and conservation of energy. CFD involves the numerical solving of the Navier-Stokes and energy equations on a discretised domain. This numerical process commences by first defining the domain and then creating the grid. The grid generation is the division of the domain into smaller control volumes. Generally, the numerical algorithm integrates the governing equations over the control volumes and, with the aid of the discretisation, the integral equations are converted into algebraic equations, which are then solved iteratively [94]. The Navier-Stokes and energy equations are then solved in these smaller volumes.

The CFD code employed in this research solves these equations on a discretised domain when relevant flow boundary conditions are specified. The general form of the equation in vector form was presented in Section 4.1.

In modelling the cavity receiver, the following basic assumptions were made:

- Steady-state conditions
- Isothermal boundary conditions were used for internals walls
- The flow in the cavity was considered to be laminar

Additional assumptions may also be specified for a specific cavity receiver model, as will be shown in chapters 5 to 7. The numerical analysis is divided into three stages: pre-processing, the solver (solution technique) and post-processing. The geometry development and grid generation within the flow domain is the pre-processing stage, while solving the flow-governing equation at various nodal points within the flow domain is regarded as the solver or solution technique. The results analysis, which involves a graphic presentation of simulation data, outputs, temperature and velocity fields of various parameters, is classified as post-processing.

When using STAR-CCM+ for simulations, the first step was to prepare the geometry of the receiver using three-dimensional computer-aided drawing (CAD) within the software. Three-dimensional CAD is tailored to suit the needs of a CFD analysis and allows changes to be made to the geometry quickly and easily, before re-running the simulation. Advanced automatic meshing technology generates either polyhedral or predominantly hexahedral control volumes at the touch of a button, offering a combination of speed, control and accuracy. The Navier-Stokes and energy equations are solved using the solver within the software.

For simulations involving radiation heat transfer, the double integral for the view factor, as in equations 3.24 and 3.25, is approximated using a ray tracing approach in STARCCM+. Collections of polygons represent surfaces and the solid angle is discretised by an angular quadrature. For each surface or patch, a predefined number of rays is traced through the computational domain starting at the patch centroid. The directions and weights are based on the discretisation of an ideal hemisphere over the patch [90]. This method is fairly simple and cost-effective compared to other methods (hemicube, hemisphere or MCRT). After the beam tracking has finished, the array of view factors obtained satisfies conservation, but not reciprocity, so a post-correction procedure is necessary to enforce reciprocity [90].

The major part of the post-processing was carried out within STARCCM+, but Matlab 2012a software and Origin8 were also used. The simulations were carried out on an Intel (R) Xeon (R) CPU 2.40 GHz PC with 12 GB of RAM.

4.3 NUMERICAL OPTIMISATION

Recent advancements in digital computer technology have seen extraordinary progress in the field of numerical methods for optimisation. Several methods have been developed for unconstrained and constrained optimisation [7]. Engineering applications for optimisation usually involve solving a non-linear constrained optimisation problem. Non-linear constrained problems involve the search for the minimum of a non-linear objective function subject to a set of non-linear constraints. Numerical optimisation deals with determining the best solution to problems that can be expressed mathematically or

numerically. In other words, it implies choosing the best element from a range of available alternatives.

4.3.1 Constrained optimisation

If we consider the optimisation problem of the general mathematical form:

$$\text{Min } f(\mathbf{x}); \mathbf{x} = [x_1, x_2, ...x_i, ...x_n]^T, \mathbf{x} \in R^n \tag{4.8}$$

and subject to the following constraints:

$$g_j(\mathbf{x}) \leq 0;\ j = 1, 2, ..., m$$

$$h_k(\mathbf{x}) = 0;\ k = 1, 2, ..., p < n$$

The function $f(\mathbf{x})$ is the objective function to be minimised (or maximised). The $g_j(\mathbf{x})$ and $h_k(\mathbf{x})$ represent the inequality and equality constraint functions respectively. The components x_i, $i = 2 \ldots n$ of x are referred to as the design variables. The optimum vector x that solves the problem denoted by Equation 4.8 is denoted by the following vector:

$$x^* = [x_1^*, x_2^*, ..., x_n^*]^T, \tag{4.9}$$

with the corresponding lowest function value $f(x^*)$ subject to the given inequality and equality constraints.

Several approaches, such as the gradient-based algorithms, can be used to solve the optimisation problem that is defined in Equation 4.8. However, engineers in all major industries are rapidly adopting automated design optimisation technology. The potential for delivering better designs in less time, compared to manual optimisation approaches, makes automated design optimisation attractive from a technical and a business standpoint [95]. In this study, an automated design optimisation tool was used, which is discussed in detail in the subsequent section.

4.3.2 Optimisation approach

The optimisation problem defined in Section 4.3.1 was solved using Optimate+, which is an add-on to the CFD code STARCCM+ that adds the capability to perform automated design optimisation studies using a Hierarchical Evolutionary Engineering Design System (HEEDS) search algorithm called Systematic Hybrid Exploration that is Robust, Progressive and Adaptive (SHERPA). SHERPA is an optimisation package that automates the iterative design process and uses an adaptive search strategy to efficiently find optimised solutions [96]. In the SHERPA scheme, the algorithm uses the elements of multiple search techniques simultaneously (not sequentially) in a unique blended manner to take advantage of the best attributes from each method. The optimisation methods contain internal tuning parameters that are modified during the search according

to the knowledge obtained from the design space. In this way, SHERPA learns about the design space and adapts in order to effectively search all types of design spaces.

The solution process for an automated design optimisation study is illustrated in Figure 4.1. The iteration steps within the dashed box occur automatically. The analysis model(s) are created prior to execution of the optimisation study and the input file(s) associated with these models are modified by the optimisation tool for each new design evaluation during the study. Aside from the analysis model(s), the key ingredient in this process is the optimisation algorithm, which controls the type and direction of the search at each iteration step. Note that some optimisation algorithms are very sensitive to the initial guesses of design variable values, while other methods are relatively insensitive to these values [95].

HEEDS gives each design a performance rating. The value returned for the objective(s) and the degree to which a design satisfies its constraints together determine the design's performance value. So, the high-performance design is the one that satisfies all the constraints and has a good rating on its objective(s). All designs that satisfy the chosen constraint essentially ignore by what margin they meet those constraints. Once the constraints are satisfied, only the objectives contribute numerically to the performance evaluation. The performance value is calculated using the following equation [96]:

$$\sum_{i=1}^{Nobj} \frac{S_i * Obj_i}{Norm_i} - \sum_{j=1}^{Ncon} penalty\left(\frac{ConstrntViolation_j}{Trget_j}\right) \tag{4.10}$$

where $Nobj$ is the number of objectives, S_i is a sign for the i-th objective, Obj_i is the response value for the i-th objective, $Norm_i$ is the normalisation factor for the i-th objective, $penalty_j$ is the penalty factor for the j-th constraint, $Ncon$ is the number of constraints, $ConstntViolation_j$ is the amount by which the j-th constraint is violated, and $Trget_j$ is target value of the j-th constraint. For feasible design (all constraints are satisfied), the performance function is a sum of the normalised objective values. When one or more constraints are violated, the performance value of the design is reduced by a value based on the violation of the constraint (the second term in the equation) [96].

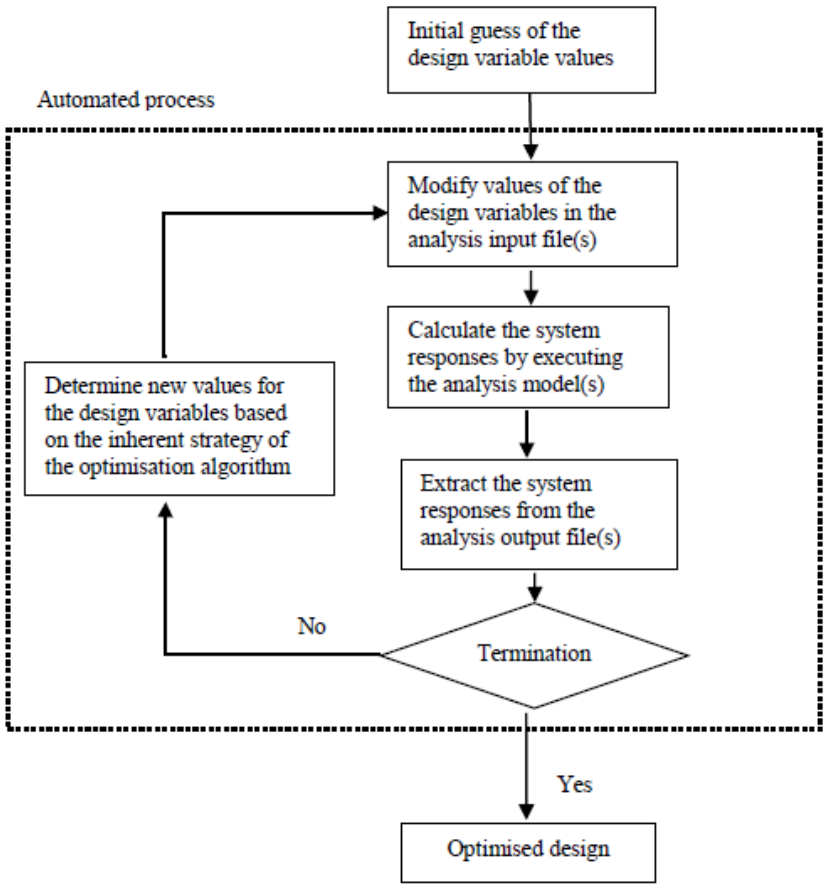

Figure 4.1: Automated design optimisation process flow chart

5

CHAPTER 5: NUMERICAL INVESTIGATION OF NATURAL CONVECTION OF CAVITY RECEIVER FOR LOW-POWER APPLICATION

5.0 INTRODUCTION

The conversion of solar energy into electricity has been receiving ever more attention in recent years. Sunlight is the world's largest energy source and the amount that can be readily accessed with existing technology greatly exceeds the world's primary energy consumption. Furthermore, sunlight is free, clean, renewable and technically exploitable in most parts of the inhabited earth.

Parabolic dish/cavity receiver configurations are some of the solar thermal systems used for light-to-heat conversion at high temperature. Such systems are subject to continuous changes in ambient conditions such as wind, solar insolation and ambient temperature. These environmental variations, as well as changes in receiver inclination angle, affect the overall receiver performance that leads to energy loss.

The total energy loss of solar receivers, which includes convection and radiation heat loss to the air and conduction heat loss through insulation, plays a dominant role in the light-to-heat conversion.

The radiation heat loss depends on the cavity wall temperature, the shape factors and the emissivity/absorptivity of the receiver walls, while conduction heat loss depends on the receiver wall temperature and the insulation material.

Analytical methods for predicting the radiative and conductive heat losses from a cavity receiver are fairly straightforward. However, this is not the case for convective heat loss analysis. The complexity of geometry, temperature and velocity fields in and around the receiver makes it difficult to use existing analytical models for predicting convective heat loss.

There are a number of papers concerning natural convection heat transfer in open cavities in literature. For instance, Le Quere et al. [25] investigated the heat loss characteristics of two different-sized cubical cavities. They considered variations in receiver operating temperature and angle in their study. They found convection heat loss to be strongly dependent on the cavity inclination. Harris and Lenz [30] presented a study that was conducted by Koenig and Marvin, which empirically derived a correlation for convective heat loss from cylindrical cavity-type receivers, including the effects of variation in operating temperature and angle. An analytical model for convective heat loss for an open cubical cavity receiver was presented by Clausing [97]. The Clausing Model was developed for a central receiver operating at much higher temperatures.

Siangsukone and Lovegrove [31] presented work on the modelling and simulation of the ANU 400 m^2 paraboloidal dish concentrator system with a direct steam-generating cavity

receiver and steam line. Taumoefolau and Lovegrove [44] presented an experimental investigation based on an isothermal, electrically heated model cavity receiver.

Sendhil Kumar and Reddy [32] presented a two-dimensional model to estimate natural convection heat loss from the modified cavity receiver of a fuzzy focal solar dish concentrator. Insulation conditions and no insulation conditions were used to estimate heat loss. The analysis of the receiver was carried out based on the assumption of the uniform and maximum solar flux distribution in the central plane of the receiver. Sendhil Kumar and Reddy [33] also presented a numerical investigation of natural convective heat loss from three types of receivers for a fuzzy focal solar dish concentrator: cavity receiver, semi-cavity receiver and modified cavity receiver.

Furthermore, Reddy and Sendhil Kumar [69] presented a numerical study of combined laminar natural convection and surface radiation heat transfer in the modified cavity receiver of a solar parabolic dish collector. Reddy and Sendhil Kumar [24] also presented a three-dimensional numerical model and compared it with other well-known cavity receiver models. They concluded that the three-dimensional model more accurately estimates heat loss in cavity receivers when compared to other models.

Prakash et al. [41] presented the effects of fluid inlet temperature and receiver inclination angle on convection heat loss from a downward-facing cylindrical cavity receiver experimentally and numerically. Experimental and numerical results agreed reasonably well. Wu et al. [34] conducted a three-dimensional numerical study to investigate the

influence of aperture characteristics. The investigation included the aspects of aperture position and size on the natural convection heat loss of a heat-pipe receiver accounting for air property variation with temperature.

Le Roux, Bello-Ochende and Meyer [98], [99] used the Second Law of Thermodynamics to optimally size a modified cavity receiver under steady state so that the parabolic dish system can have maximum net power. Mwesigye, Bello-Ochende and Meyer [100] carried out a numerical analysis of a solar receiver to investigate the effects of different concentration ratios.

In this thesis, a numerical investigation of a modified cavity receiver was conducted to quantify the natural convection heat loss and determine the effects of the operating temperature, receiver inclination angle and aperture size on heat loss. Furthermore, visualisation results, such as temperature contours, were also presented to gain insight into the effects of natural convection. The Boussinesq and non-Boussinesq fluid models were used in the numerical investigation and a comparison was made between them.

For the fluids modelled as Boussinesq incompressible, the density was regarded as a constant property everywhere except in the body force terms of the momentum equations. In this approximation, the density was treated as a linear function of temperature only and was assumed to be independent of pressure.

The focus was on modified cavity receivers employed in medium- and high-temperature solar dish systems with an operating temperature of up to 1000 K that accounted for the air property variations. The Boussinesq approximation, which was applied in previous numerical investigations for modified cavity receivers [24], [32], [33], [69], leads to considerable deviations at high operating temperatures and can no longer be applicable to such receivers, because the air properties change significantly with the remarkable operating temperature increments. For example, when the air temperature rises from the ambient temperature of 300 K to the receiver's operating temperature of 1000 K, air density decreases by 77.72%, thermal conductivity increases by 780.76%, kinematic viscosity increases by 252.95%. These significant changes in physical air properties definitely have an important influence on natural convection heat loss.

5.1 PHYSICAL AND MATHEMATICAL MODEL

The modified cavity receiver without insulation suggested by Reddy and Sendhil Kumar [32] is considered in the analysis.

The collector system consists of a parabolic dish collector operating in tracking mode as shown in Figure 5.1. The receiver is made of copper tubing with an opening aperture diameter (d) and cavity diameter (D) of 180 mm. The copper tubes are spirally wound to get the shape of the receiver. The outer surface of the cavity receiver is completely covered with opaque insulation. Two assumptions are made for modelling the cavity receiver: the surfaces of the tube are uniform and smooth, and the temperature of air flowing through the copper tube is the same as the surface temperature of the tube.

Natural convection heat loss is estimated at different inclination angles of the receiver from $\theta = 0^o$ (cavity receiver aperture facing sideways) to $\theta = 90^o$ (cavity aperture facing downwards). To investigate the effects of aperture diameter, the aperture diameter is varied from 60 to 120 mm.

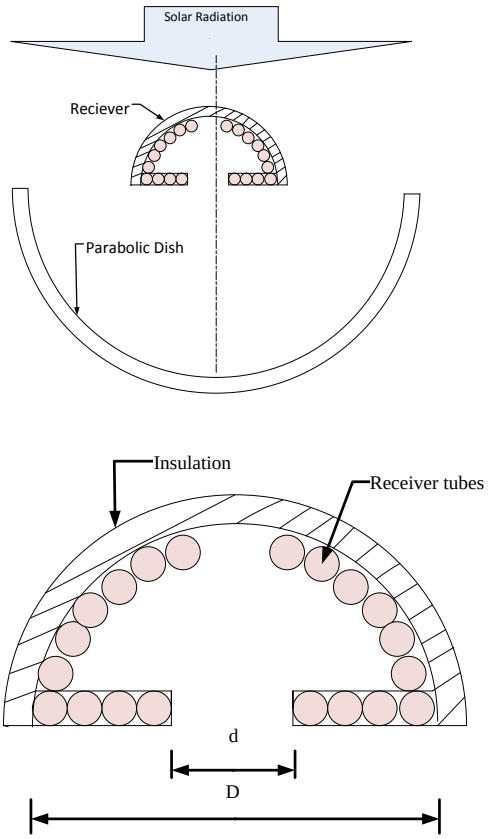

Figure 5.1: Schematic of a parabolic dish-concentrating collector with a modified cavity model

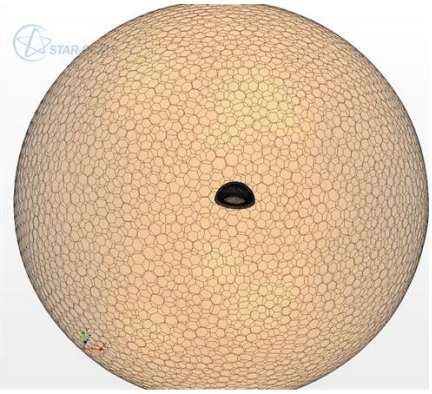

Figure 5.2: Typical computational grid for the numerical analysis of the modified cavity receiver

For natural convection in the cavity receiver, the flow and heat transfer simulations are based on the simultaneous solution of equations describing the conservation of mass, momentum and energy of the system.

Continuity equation:

$$\Delta \cdot (\rho \mathbf{V}) = 0 \tag{5.1}$$

Momentum equation:

$$V \cdot \nabla(\rho \mathbf{V}) = \rho \mathbf{X} - \nabla p + \nabla^2(\mu \mathbf{V}) \tag{5.2}$$

Energy equation:

$$\mathbf{V} \cdot \nabla(\rho c_p T) = \nabla^2(kT)\,, \tag{5.3}$$

where ρ is the density of air in kg/m^3, $\mathbf{V}$ is the velocity vector of air in m/s, $\mathbf{X}$ is the mass force vector in N/kg, p is the pressure in Pa, μ is dynamic viscosity in kg/(m.s), c_p is the specific heat capacity at constant pressure in J/(kg.K), k is the thermal conductivity of air in W/(m.K) and T is temperature in K.

Polynomial relationships for density, specific heat capacity at constant pressure and dynamic viscosity are used to account for air property variation with temperature [92].

$$\rho = 7.4992\times10^{-9}T^3 + 1.6487\times10^{-5}T^2 - 1.2366\times10^{-2}T + 3.6508 \tag{5.4}$$

$$c_p = 1.3864\times10^{-13}T^4 - 6.4747\times10^{-10}T^3 + 1.0234\times10^{-6}T^2 - 4.3282\times10^{-4}T + 1.0613 \tag{5.5}$$

$$\mu = 1.3864\times10^{-15}T^3 - 1.4346\times10^{-11}T^2 + 5.0523\times10^{-8}T + 4.1130\times10^{-6} \tag{5.6}$$

$$k = 1.5797\times10^{-17}T^5 + 9.4600\times10^{-14}T^4 + 2.2012\times10^{-10}T^2 - 2.3758\times10^{-7}T^2 + 1.7082\times10^{-4}T^2 - 7.488\times10^{-3} \tag{5.7}$$

The convective heat transfer coefficient can be expressed as:

$$h_c = \frac{Nuk}{D} \tag{5.8}$$

where Nu is the Nusselt number and D is the receiver cavity diameter. The Nusselt numbers were calculated using STAR-CCM+ 7.06.

The convective heat loss from the modified cavity receiver is given as:

$$Q_c = h_c A(T_s - T_\infty) \tag{5.9}$$

5.2 NUMERICAL PROCEDURE AND VALIDATION

A finite volume-based CFD code, STAR-CCM+ 7.06, was employed in the three-dimensional simulation of the natural convection through the aperture of the cavity receiver. Figure 5.2 schematically represents the computational grid of the cavity receiver. In reality, the receiver was surrounded by an infinite atmosphere with a limiting temperature equal to the ambient air temperature. In the numerical analysis, the region outside the cavity was represented by a spherical enclosure. The size of the enclosure was increased until it had an insignificant effect on fluid and heat flows in the vicinity of the receiver.

In STARCCM+, it was found that the diameter of the spherical enclosure should be about 10 times the diameter of the receiver to achieve this.

A mesh refinement was performed on the cavity receiver and it investigated the average Nusselt number on the hot inner surfaces of the cavity receiver (T_s = 800 K and Ra = 10^6).

Table 5.1 presents the average Nusselt numbers that were obtained for five different grids at a 90° inclination angle of the receiver. The relative deviation for the Nusselt number between Grid 1 and Grid 2 was less than 1%. Since the differences between the two were minor, Grid 2 was chosen for all the simulations presented in this work. This was considered a good trade-off between accuracy and cost of time.

Table 5.1: Average Nusselt numbers for different grids

Grid number	Number of cells	Nusselt number	Relative deviation
1	1.85×10^5	12.3475	
2	1.70×10^5	12.3463	0.000101
3	1.58×10^5	12.2686	0.006288
4	1.43×10^5	12.3802	-0.00909
5	1.38×10^5	12.3123	0.005486

The cells were very small in the region inside the cavity and near the receiver, but gradually increased in size towards the spherical enclosure wall. Prism layer cells were also used on the walls of the cavity receiver. This layer of cells was necessary to improve the accuracy of the flow solution.

Since the Ra encountered were less than 10^8, the laminar, steady-state and three-dimensional governing equations were solved by STAR-CCM+ using an implicit solver.

5.2.1 Boundary conditions

An isothermal boundary condition was applied to the internal receiver surfaces and the outer surface on the aperture plane as shown in Figure 5.3. The temperature was varied

from 400 K to 1000 K. The outer surface of the receiver were treated as adiabatic, since they were covered with insulation to prevent heat loss.

The outer domain was treated as a pressure outlet boundary condition. The wall temperature of the entire spherical enclosure was set to an ambient temperature of 300 K.

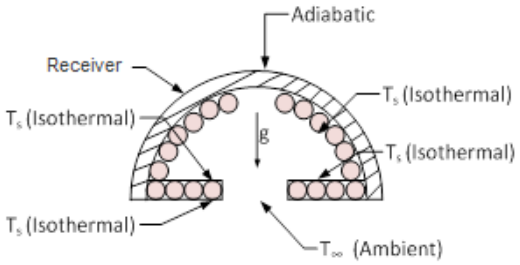

Figure 5.3: Numerical model and boundary conditions of the modified cavity receiver

5.2.2 Validation

To validate the present numerical procedure of the modified cavity receiver, a typical case of three-dimensional laminar natural convection heat transfer from an isothermal horizontal open hemispherical cavity reported by Khubeiz, Radziemska and Lewandowski [101] has been considered. The results of the theoretical analysis, numerical calculation and experimental procedure are presented in the Nusselt and Ra relations: $Nu_D = 0.296Ra_D^{1/4}$, $Nu_D = 0.340Ra_D^{1/4}$ and $Nu_D = 0.316\ Ra_D^{1/4}$ respectively. This present numerical procedure has been validated using glycerine as the working fluid. The isotherms of the upward-facing hemispherical open cavity at Ra of 1.1511×10^7 are shown in Figure 5.4.

The area-weighted average Nusselt numbers for the hot surface of the hemisphere were obtained for two different Ra. The results are given in Table 5.2. It was observed that the present numerical procedure was in good agreement with the experimental data with a maximum deviation of approximately 6.45%.

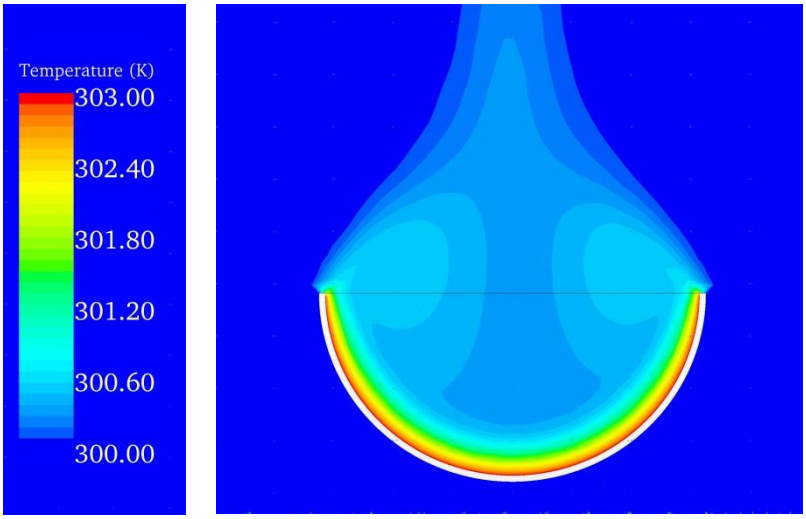

Figure 5.4: Temperature contours of mid plane of upward open hemispherical cavity

Table 5.2: Validation of the present numerical procedure using an experimental convective Nusselt number

Rayleigh number	Nusselt number from [101]			Nusselt number from present numerical procedure	Percentage of deviation from experimental value
	Nu_{exp}	Nu_{num}	Nu_{anal}		
2.4864×10^{6}	12.55	13.50	11.75	11.74	6.45
1.1511×10^{7}	18.41	19.80	17.24	18.82	-2.23

5.3 RESULTS AND DISCUSSION

5.3.1 Effects of receiver inclination angle and operating temperature on natural convection heat loss

To estimate the natural convection heat loss from the modified cavity receiver, the temperature was varied from 400 K to 1000 K.

Figure 5.5 shows the temperature contours of the modified cavity receiver on the symmetry plane operating at 400 K for different inclinations of the receiver.

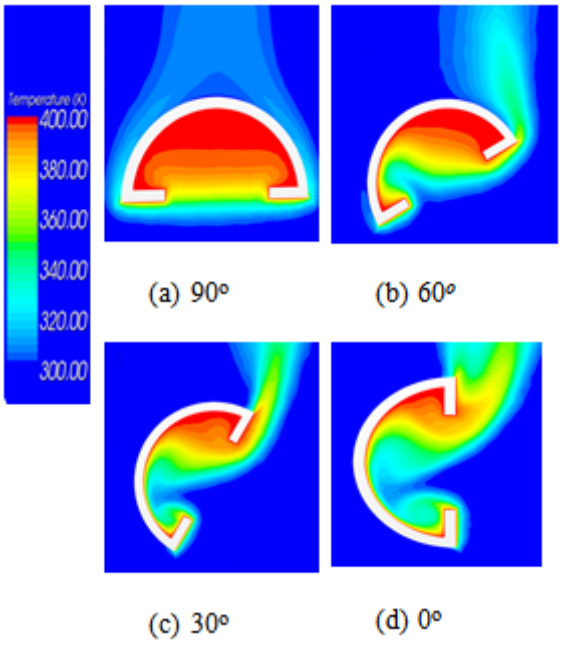

Figure 5.5: Temperature contours of the cavity at 400 K for various inclination angles

The behaviour of air in the cavity receiver was completely different at varying inclination angles of the receiver. In the downwards-facing position of 90°, the cavity was almost dominated by the stagnant zone, thus convection heat loss out of the receiver was small. When the receiver inclination angle was varied anticlockwise, the stagnant zone

decreased and this increased the convective zone where most of the heat transfer mainly took place.

The near stagnant air and almost uniform temperature within the stagnation zone suggests that it does not take part in convective heat transfer, and convective heat loss takes place from the convective zone.

It can be seen from Figure 5.5 that the temperatures of the lower part of the inclined cavity walls are relatively lower, while the temperatures of the upper parts of the walls are higher. The explanation for this is that as air at ambient temperature is driven into the cavity receiver by the natural convective currents, the air adjacent to the receiver surface becomes hotter and lighter as it absorbs heat from the receiver surfaces and consequently flows up along the cavity wall. As a result, hot, stagnant air only appears at the top of the cavity receiver. Eventually, the hot air leaves the cavity through the aperture and is cooled by the ambient air.

From Figure 5.6, it is observed that the convective heat loss varies non-linearly with receiver angle inclination at high operating temperatures. However, it is approximately linear at 400 K. The convective heat loss is at a minimum for all operating temperatures when the receiver aperture orientation is downwards. This supports the assumption of negligible convective heat loss with the receiver in this position, as observed by other researchers. Maximum heat loss occurs when the receiver aperture is orientated at 0^{o}. It

is also observed that the effect of the angle of inclination on convection heat loss is more significant for a higher receiver temperature.

For example, the percentage decrease of the convection heat loss from 0 to 90^{o} is about 68.87% at a 1000 K operating temperature in contrast to about 10% at 400 K. This can be attributed to the fact that the convection zone extends as the receiver moves anticlockwise, thus causing an increase in convection heat loss.

The convection heat loss from the receiver was estimated for operating temperatures ranging from 400 K to 1000 K at intervals of 200 K. From Figure 5.7, it was found that the convection heat loss increased tremendously with increasing receiver operating temperatures. The effect of the inclination angle on convection heat loss was not much at lower operating temperatures compared with higher operating temperatures where it was significantly higher. It is further observed from Figure 5.7 that the convection heat loss is closely linearly dependent on operating temperature.

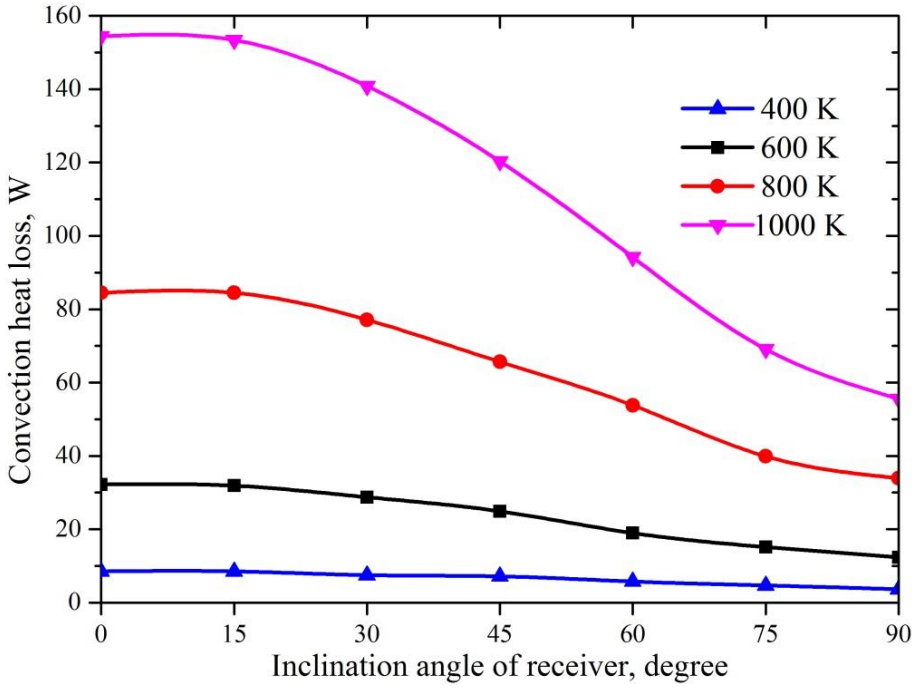

Figure 5.6: Variation of convection heat loss with inclination angle

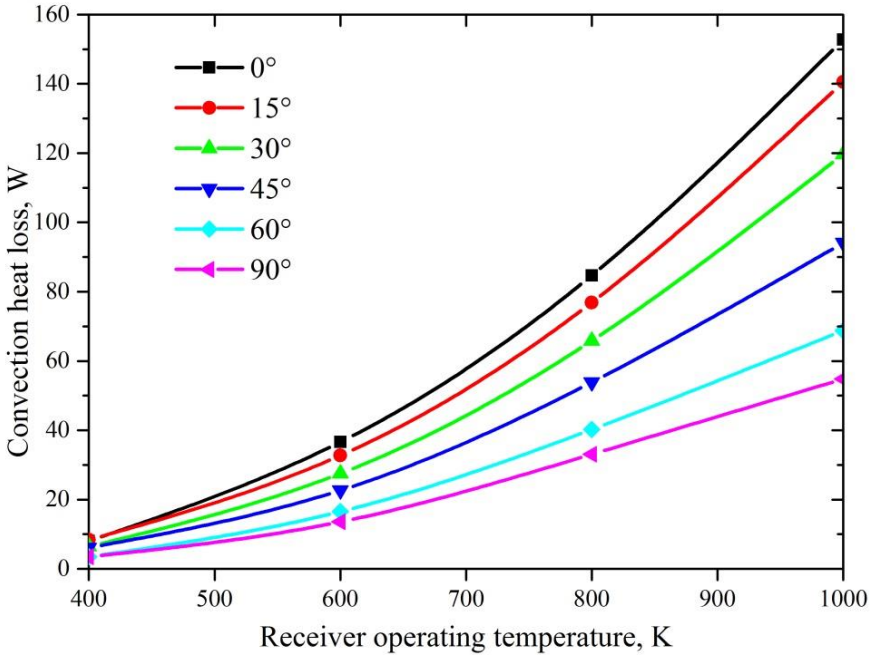

Figure 5.7: Variation of convection heat loss with operating temperature

5.3.2 Effects of aperture size on natural convection heat loss

To explore the effects of aperture size on natural convection heat loss, the diameter of the aperture was varied from 60 to 120 mm at an 800 K operating temperature. Figure 5.8 shows the variation of convection heat loss with the aperture size at different inclination angles.

It is clear from Figure 5.8 that, as the aperture size becomes larger, the convection heat loss also increases. However, the increase in the convection heat loss at 60 and 90^{o} is minimal in comparison with the increase at other inclination angles. This is due to the fact that, as the cavity receiver moves anticlockwise, the convection zone apparently expands with an increasing inclination angle, which definitely leads to a considerable increment of the convection heat loss. This also explains that convection heat loss is not significantly affected when the receiver faces downwards as confirmed by the curves for 60 and 90^{o}. This leads to the conclusion that the effect of aperture size on convection heat loss is actually closely related to the receiver inclination angle.

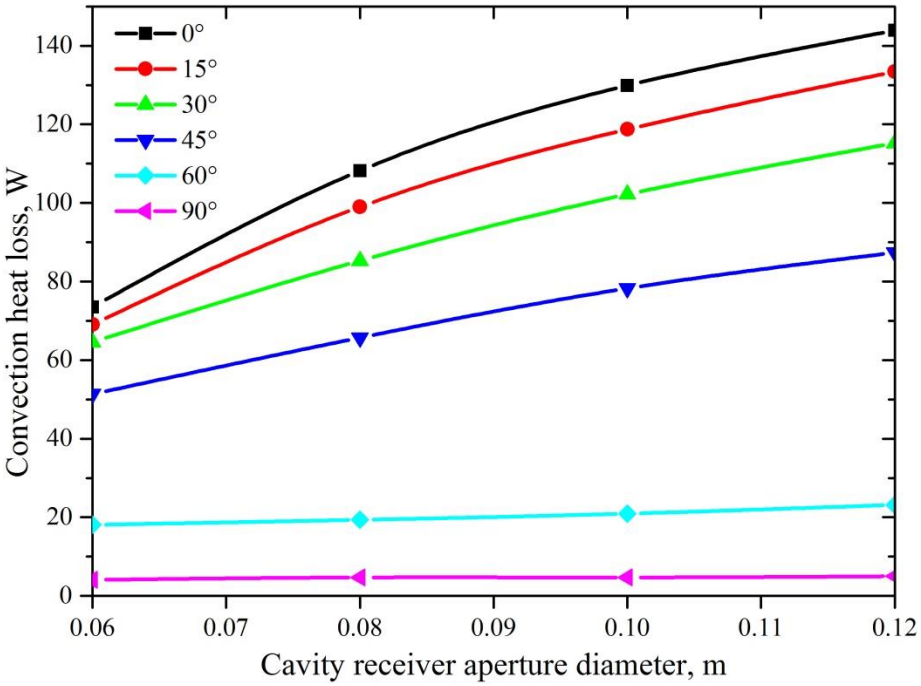

Figure 5.8: Variation of convection heat loss with aperture diameter at 800 K

5.3.3 The comparison of the Boussinesq and non-Boussinesq fluid models

For the fluids modelled as Boussinesq incompressible, the fluid properties were assumed to be constant and the density was treated as a linear function of temperature only, and was assumed to be independent of pressure. Temperature-dependent air properties were used for the non-Boussinesq model to account for the air property variations. The comparison between the Boussinesq and non-Boussinesq fluid models was made at equal equivalent Ra.

Figure 5.9 and Figure 5.10 show the variation of the convection heat loss with the inclination angles of the receiver for the Boussinesq and non-Boussinesq fluid models. It can be seen from Figure 5.9 that, at a receiver operating temperature of 400 K, the non-

Boussinesq solution agreed with the Boussinesq solution with a maximum deviation of 6.1% when the receiver was at 0^o inclination and a minimum deviation of 1.7% at a 90^o inclination angle.

Comparison of the non-Boussinesq and Boussinesq fluid models at a 1000 K operating temperature shows larger deviations with a maximum deviation of 19.48% at 0^o inclination angle and a minimum deviation of 7.7% at a 90^o inclination angle as shown in Figure 5.10.

It is therefore observed that the Boussinesq fluid model provides a good approximation of air density data and other air properties only in the regime with a small temperature difference. An increase in the temperature difference leads to a growth in air properties error between the Boussinesq approximation and the non-Boussinesq fluid model. Without accurate predictions for the density and other air properties, the results obtained based on the Boussinesq incompressible fluid model probably cannot reflect the real phenomenon taking place in the cavity receiver. Therefore, the Boussinesq solution can be regarded as the solution for the limiting case with a small operating temperature difference.

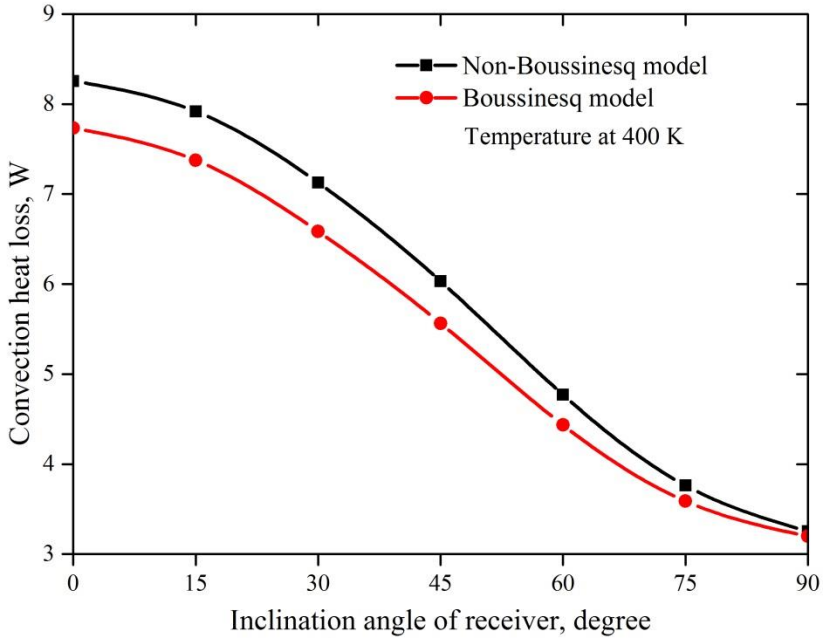

Figure 5.9: Variation of convection heat loss with an inclination angle at 400 K

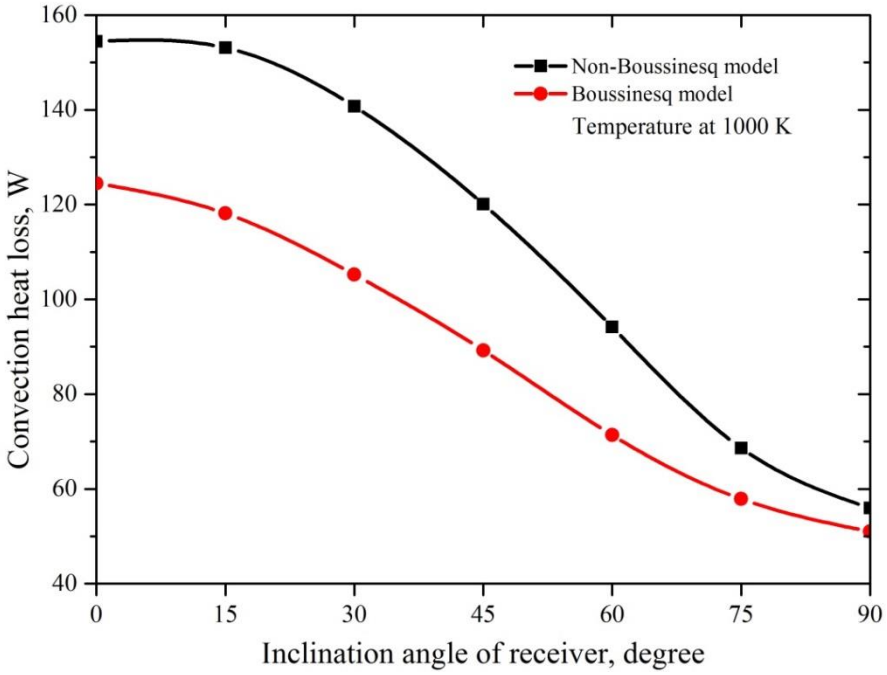

Figure 5.10: Variation of convection heat loss with an inclination angle at 1000 K

5.4 CONCLUSION

A numerical investigation was conducted on a modified cavity receiver to quantify the natural convection heat loss and to determine the effects of the operating temperature, receiver inclination angle and aperture size on heat loss. The effects of the variation of air properties were also accounted for by using polynomial relationships for density, specific heat capacity at constant pressure and dynamic viscosity.

It was observed that the convective heat loss varied non-linearly with receiver angle inclination at high operating temperatures. The convection heat loss was at a minimum for all operating temperatures when the receiver aperture orientation was facing downwards. The maximum heat loss occurred when the receiver aperture was orientated at 0^o. It was found that the convective heat loss increased tremendously with increasing receiver operating temperatures and the effect of inclination angle on convection heat loss was not much at lower operating temperatures when compared with higher operating temperatures where it was significantly higher.

It is clear that, as the aperture size became larger, the convection heat loss also increased. However, the increase in convection heat loss at 75 and 90^o was minimal compared with the increase at other inclination angles. This leads to the conclusion that the effect of aperture size on convection heat loss is closely related to the receiver inclination angle.

The comparison between the Boussinesq and non-Boussinesq fluid models showed some agreement at lower operating temperatures with a maximum deviation of 6.1%. However, the deviation was much higher at higher operating temperatures with a maximum deviation of 19.48%.

6

CHAPTER 6: NUMERICAL MODELLING AND OPTIMISATION OF NATURAL CONVECTION HEAT LOSS SUPPRESSION IN A SOLAR CAVITY RECEIVER WITH PLATE FINS

6.0 INTRODUCTION

The use of concentrating solar thermal technology has great potential for generating power. The parabolic dish receiver assembly is one such promising system. It usually consists of a reflector in the form of a dish with a downward-facing receiver at the focus of the dish. These systems are continuously subjected to changes in environmental conditions, such as wind, solar insolation and ambient temperature. These environmental variations, coupled with changes in receiver inclination angle, affect the overall receiver performance, leading to energy loss.

A cavity receiver is used to maximise the absorption of the concentrated solar flux. The total energy loss of solar receivers, which includes convection and radiation heat loss to the air and conduction heat loss through insulation, plays a dominant role in the light-to-heat conversion. The radiation heat loss depends on the cavity wall temperature, the shape factors and emissivity/absorptivity of the receiver walls, while conduction heat loss depends on the receiver wall temperature and insulation material. Natural convection

through the receiver aperture contributes a significant fraction of the energy loss. Hence, it is essential to effectively minimise it in order to improve the system efficiency.

The flow and heat transfer research of the cavity receiver helps in estimating the thermal performance and optimisation of the receiver design [46], [102], [103]. With cavity receivers, radiation and conduction can readily be determined analytically. However, this is not the case for natural convection. The complexity of geometry, temperature and velocity fields in and around the receiver makes it difficult to use existing analytical models for predicting convective heat loss. Therefore, many significant investigations have been conducted on natural convection heat transfer in open cavities and are available in literature [24], [25], [28], [30]–[33], [41], [44], [58].

Minimising natural convection is seen as an effective method to improve the thermal efficiency of cavity receivers. Some investigations have been reported on the heat loss reduction of cavity receivers. For instance, Kribus et al. [66] designed and tested a multistage receiver that divided the aperture into separate stages according to the irradiation distribution to achieve high working temperature and thermal efficiency. Bertocchi, Karni and Kribus [102] designed a frustum-like high-pressure window for a volumetric solar receiver. The transparent window prevented the working fluid and much of the radiation emitted in the cavity from escaping to the ambient air. Reddy and Sendhil Kumar [69] analysed the heat transfer behaviour of the modified cavity receiver with a cone, CPC and trumpet reflector. The results showed that the receiver with a trumpet reflector performed the best.

The heat transfer rate through the enclosures can be controlled by means of the fins' configuration and literature is available on the subject [102]–[116]. In this study, a cavity receiver with plate fins attached to the inner aperture surface is presented as a possible low-cost means of suppressing natural convection heat loss in a cavity receiver. This numerical study employs air as the working fluid. Laminar natural convection heat transfer from a cavity receiver with plate fins attached to the inner aperture surface has been investigated for a range of Ra, inclination angles, and fin heights and thicknesses. Furthermore, visualisation results, such as fluid flow and temperature contours, have also been presented to gain insight into the suppression of natural convection. In addition, a numerical optimisation tool is used to select the best plate fin geometric configuration that improves the cavity receiver performance at minimum natural convection heat loss. This study presents a novel approach of suppressing natural convection heat loss in a cavity receiver. The proposed model has not been observed in literature.

6.1 PHYSICAL AND MATHEMATICAL MODEL

In this study, a three-dimensional cavity receiver is considered. Figure 6.1 shows the schematics of the cavity receiver and the proposed cavity with plate fins from a two-dimensional orientation. Compared with the prototype cavity receiver (Figure 6.1a), isothermal circular plate fins were installed on the inner side of the aperture surface on the proposed receiver (Figure 6.1c) to suppress natural convection. Both receivers are made of copper tubing with an opening aperture diameter (d) and cavity diameter (D). The diameter of the receiver and its aperture are defined as 180 and 100 mm

respectively. The copper tubes are spirally wound to get the shape of the receiver. The outer surface of the cavity receiver is completely covered with opaque insulation.

The following assumptions are made for modelling the cavity receiver: there is uniform and maximum solar flux distribution in the cavity receiver, the surfaces of the tube are uniform and smooth for the prototype cavity receiver, the plate fins are made of copper and installed on the inner side of the aperture surface between the copper tubing, and the temperature of air flowing through the copper tube is the same as the surface temperature of the tube. The copper tubes were not considered in the simulation.

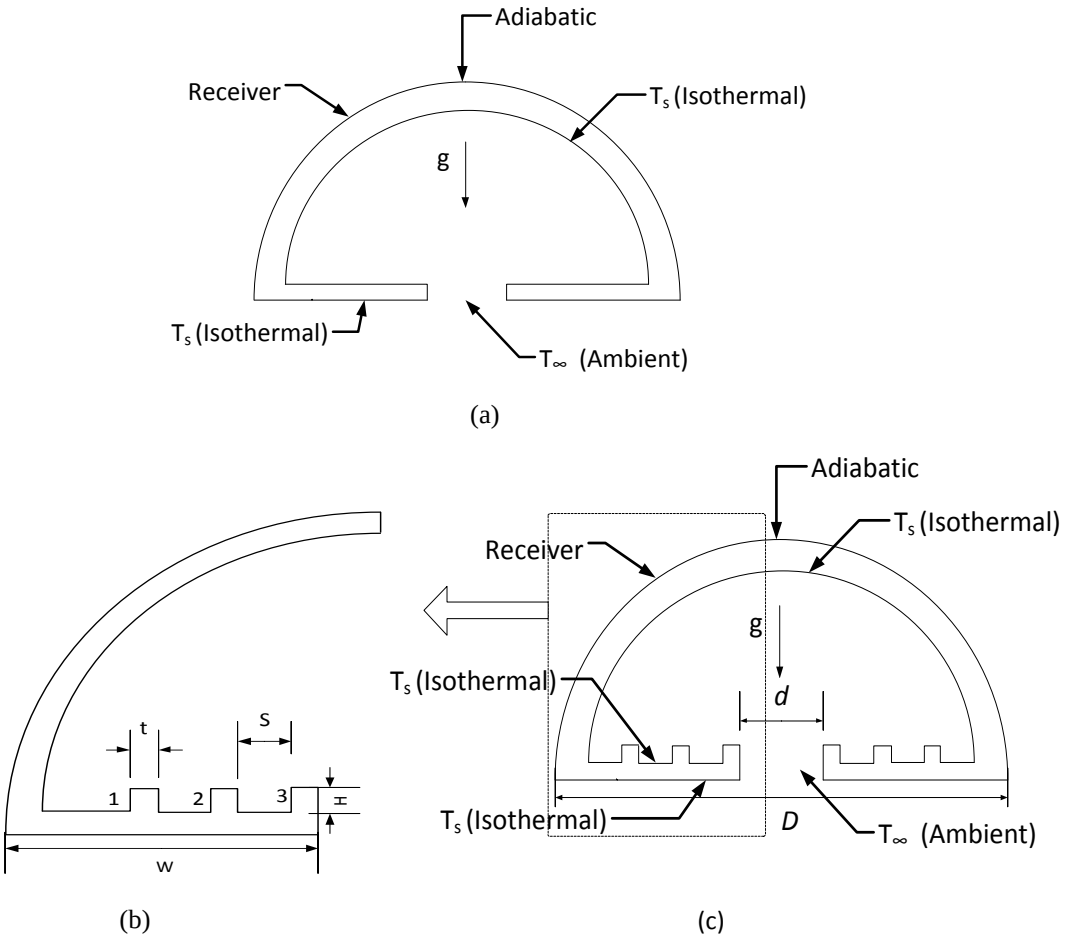

Figure 6.1: Schematic of modified cavity receiver with and without plate fins

The inclusion of plate fins in this study is aimed at reducing natural convection in the cavity receiver, thus improving its performance. The numerical study employs air as the working fluid (*Pr* = 0.71). The design variables that greatly affect the hydrodynamic performance of plate fins are the geometric parameters of fin heights (H_1, H_2, and H_3), fin thickness (t_1, t_2 and t_3) and the number of fins N, as depicted in Figure 6.1b. The fin height and thickness are defined as dimensionless parameters H_j/W and t_j/W respectively in this study (for j = 1, 2, 3).

Natural convection heat loss was estimated at different Ra, inclination angles, and plate fin heights and thicknesses. The dimensionless fin heights were varied in the following range: $0.025 \leq H_j/W \leq 0.15$. The dimensionless thicknesses of the fins were varied in the range: $0.025 \leq t_j/W \leq 0.125$ and the value of N was varied from 0 to 3, where $N = 0$ indicates no fin condition. In this study, the distance between two plate fins (*S*) varies depending on the thickness of the fin plates. The Ra was varied in the range: $10^4 \leq Ra \leq 10^7$.

For natural convection in the cavity receiver, the flow and heat transfer simulations are based on the simultaneous solution of equations describing the conservation of mass, momentum and energy of the system.

Continuity equation:

$$\Delta \cdot (\rho \mathbf{V}) = 0 \tag{6.1}$$

Momentum equation:

$$\mathbf{V} \cdot \nabla (\rho \mathbf{V}) = \rho \mathbf{X} - \nabla p + \nabla^2 (\mu \mathbf{V}) \tag{6.2}$$

Energy equation:

$$\mathbf{V} \cdot \nabla (\rho c_p T) = \nabla^2 (kT), \tag{6.3}$$

where ρ is the density of air in kg/m^3, $\mathbf{V}$ is the velocity vector of air in m/s, $\mathbf{X}$ is the mass force vector in N/kg, p is the pressure, Pa, μ is dynamic viscosity in kg/(m.s), c_p is the specific heat capacity at constant pressure in J/(kg.K), k is the thermal conductivity of air in W/(m.K) and T is temperature in K.

The Boussinesq approximation, which has been applied in previous numerical investigations for modified cavity receivers [24], [32], [33], [58] leads to considerable deviations at high operating temperatures and can no longer be applicable to such receivers because the air properties change significantly with the remarkable operating temperature increments. Polynomial relationships for density, specific heat capacity at constant pressure and dynamic viscosity are used to account for air property variation with temperature [92].

$$\rho = 7.4992\times10^{-9}T^3 + 1.6487\times10^{-5}T^2 - 1.2366\times10^{-2}T + 3.6508 \quad (6.4)$$

$$c_p = 1.3864\times10^{-13}T^4 - 6.4747\times10^{-10}T^3 + 1.0234\times10^{-6}T^2 - 4.3282\times10^{-4}T + 1.0613 \quad (6.5)$$

$$\mu = 1.3864\times10^{-15}T^3 - 1.4346\times10^{-11}T^2 + 5.0523\times10^{-8}T + 4.1130\times10^{-6} \quad (6.6)$$

$$k = 1.5797\times10^{-17}T^5 + 9.4600\times10^{-14}T^4 + 2.2012\times10^{-10}T^2 - 2.3758\times10^{-7}T^2 + 1.7082\times10^{-4}T^2 - 7.488\times10^{-3} \quad (6.7)$$

The convective heat transfer coefficient can be expressed as:

$$h_c = \frac{Nuk}{D} \quad (6.8)$$

where Nu is the Nusselt number and D is the receiver cavity diameter. The Nusselt numbers were calculated using a CFD code. The convective heat loss from the modified cavity receiver is given as:

$$Q_c = h_c A(T_s - T_\infty) \quad (6.9)$$

The Ra for all results in this study is based on the cavity receiver diameter D and is defined as:

$$Ra = \frac{g\beta(T_s - T_\infty)D^3}{\nu\alpha} \tag{6.10}$$

where g is the acceleration due to gravity in m/s², β is the thermal expansion coefficient in 1/K, ν is the kinematic viscosity in m²/s and α is the thermal diffusivity in m²/s.

6.2 NUMERICAL PROCEDURE AND VALIDATION

6.2.1 Numerical procedure

A finite volume-based CFD code, STAR-CCM+ 7.06, was employed in the three-dimensional simulation of the natural convection through the aperture of the cavity receiver. Figure 6.2 schematically represents a computational grid of the cavity receiver. In reality, the receiver is surrounded by an infinite atmosphere with a limiting temperature equal to the ambient air temperature. In the numerical analysis, the region outside the cavity is represented by a spherical enclosure (Figure 6.2a). The size of the enclosure was increased until it had an insignificant effect on fluid and heat flows in the vicinity of the receiver. In STARCCM+, it was found that the diameter of the spherical enclosure should be about ten times the diameter of the receiver to achieve this.

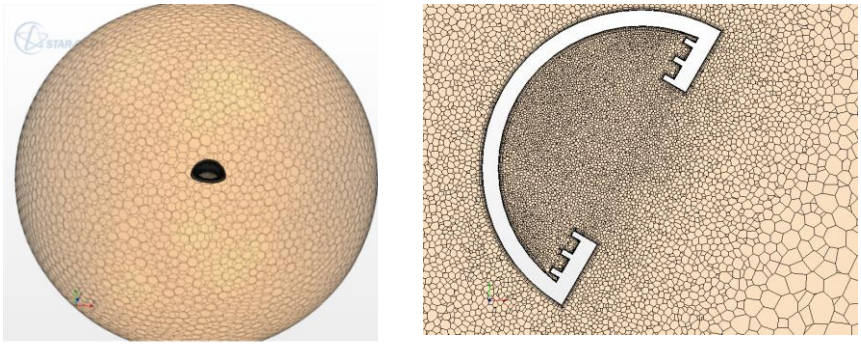

(a) (b)

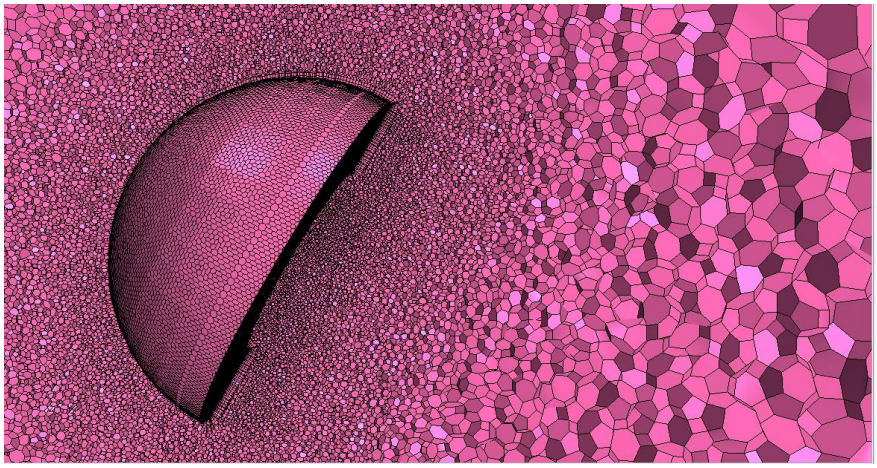

(c)

Figure 6.2: Typical computational grid for the numerical analysis of the modified cavity receiver: (a) three-dimensional, including sphere; (b) two-dimensional cross-section at 30º; (c) refined polyhedral cells are in and around the cavity at 30º and the coarse mesh towards the sphere

The cells are very small in the region inside the cavity and near the receiver, but gradually increase in size towards the spherical enclosure wall. Prism layer cells were also used on the walls of the cavity receiver (Figure 6.2b). The prism layer mesh model was used with a core volume mesh to generate orthogonal prismatic cells next to wall boundaries. This layer of cells is necessary to improve the accuracy of the flow solution [90]. Since the Ra encountered are less than 10^8, the laminar, steady-state and three-dimensional governing

equations are solved by STAR-CCM+ using an implicit solver. The convergence criteria for the residuals of continuity and the velocity equations are of the order of 10^{-3}, while for the energy equation it is 10^{-5}. The solutions are obtained once the convergence criteria are satisfied.

A mesh refinement was performed on the cavity receiver, investigating the average Nusselt number on the hot inner surfaces of the cavity receiver (T_s = 800 K and Ra = 10^6). Table 6.1 presents the average Nusselt numbers for four different grids at two different inclination angles of the receiver (θ = 0º and θ = 30º). The relative deviation for the Nusselt number between Grid 1 and Grid 2 was less than 1%. Since the differences between the two were minor, Grid 2 was chosen for all the simulations presented in this study. This was considered a good trade-off between accuracy and cost of time.

Table 6.1: Average Nusselt numbers for different grids

Grid number	Cells	Nusselt number			
		θ = 0º	Relative deviation	θ = 30º	Relative deviation
1	801 337	10.1675		18.2941	
2	320 000	10.1529	0.001436	18.2734	0.001132
3	241 336	10.2338	-0.00797	18.2008	0.003973
4	218 272	10.2947	-0.00595	18.2096	-0.00048

6.2.1.1 Boundary conditions

An isothermal boundary condition was applied to the internal receiver surfaces, outer surface on the aperture plane, as well as the fins. The temperature was varied from 400 to 1000 K. The outer spherical walls of the receiver were treated as adiabatic since they were

covered with insulation to prevent heat loss. The outer domain was treated as a pressure outlet boundary condition. The wall temperature of the entire spherical enclosure was set to an ambient temperature of 300 K.

6.2.2 Validation

The numerical procedure was validated using the experimental work reported by Shiina, Fujimura, Kunugi and Akino [117] as shown in Table 6.2. The enclosed hemisphere was experimentally studied under steady-state, laminar conditions. The curved portion and bottom surface were taken as cold and hot surfaces respectively. The area weighted average Nusselt numbers of the hot surface of the enclosed hemisphere were obtained for different Ra. It was observed that the present numerical procedure is in good agreement with the experimental data with maximum deviation approximately 2.8%.

Table 6.2: Validation of the Nusselt number by using present procedure

Rayleigh number	Nusselt number		Percentage of deviation
	Shiina et al [117]	Present work	
1.9437×10^{5}	6.91	7.09	-2.6
2.8523×10^{6}	7.60	7.39	2.8
4.9288×10^{6}	8.72	8.62	1.1
7.8266×10^{6}	9.78	9.86	-0.8
1.1683×10^{7}	10.82	10.84	-0.2
2.2818×10^{7}	12.79	12.44	2.7

6.3 OPTIMISATION PROBLEM FORMULATION

The optimisation problem was tailored towards finding the best plate fin geometric parameters that give the least natural heat loss from the modified receiver cavity for different Ra and inclination angles at a given temperature. The plate fin heights and thicknesses, as indicated in Section 2, greatly affect the hydrodynamic performance of plate fins. The dimensionless fin heights were varied in the following range: $0.025 \leq H_j/W \leq 0.15$. The dimensionless thicknesses of the fins were varied in the range: $0.025 \leq t_j/W \leq 0.125$. The distance between two plate fins varies depending on the thickness of the fins and is not considered. The type of optimisation considered in this study is the placement of individual plate fins to form channels. This leads to the treatment of an array of fins in which each fin operates optimally [118].

6.3.1. Optimisation approach

The optimisation problem defined in Section 4.0 was solved using Optimate+, an add-on to the CFD code STAR-CCM+ that adds the capability to perform automated design optimisation studies using SHERPA, a HEEDS search algorithm. This is an optimisation package that automates the iterative design process and uses an adaptive search strategy to efficiently find optimised solutions [96].

In the SHERPA scheme, the algorithm uses the elements of multiple search techniques simultaneously (not sequentially) in a unique blended manner in attempts to take

advantage of the best attributes from each method. The optimisation methods contain internal tuning parameters that are modified during the search according to the knowledge obtained from the design space. In this way, SHERPA learns about the design space and adapts it in order to effectively search all types of design spaces.

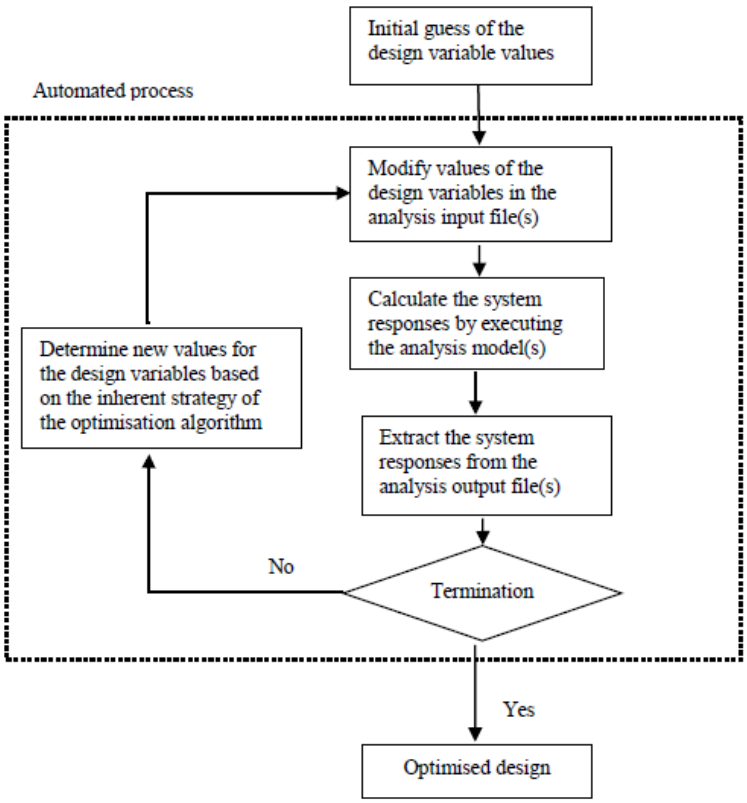

Figure 6.3: Automated design optimisation process flow chart

The solution process for an automated design optimisation study is illustrated in Figure 6.3. The iteration steps within the dashed box occur automatically. The analysis models are created prior to the execution of the optimisation study, and the input files associated with these models are modified by the optimisation tool for each new design evaluation during the study. Aside from the analysis model(s), the key ingredient in this process is

the optimisation algorithm, which controls the type and direction of the search at each iteration step. Note that some optimisation algorithms are very sensitive to the initial guesses of design variable values, while other methods are relatively insensitive to these values [95].

HEEDS gives each design a performance rating. The value returned for the objective(s) and the degree to which a design satisfies its constraints determine the design's performance value. So, a high-performance design satisfies all the constraints and has a good rating on its objective(s). All designs that satisfy the chosen constraint essentially ignore by what margin they meet those constraints. Once the constraints are satisfied, only the objectives contribute numerically to the performance evaluation. The performance value is calculated using the following equation [96]:

$$\sum_{i=1}^{Nobj} \frac{S_i * Obj_i}{Norm_i} - \sum_{j=1}^{Ncon} penalty \left(\frac{ConstrntViolation_j}{Trget_j} \right) \tag{6.11}$$

where $Nobj$ is the number of objectives, S_i is a sign for the i-th objective, Obj_i is the response value for the i-th objective, $Norm_i$ is the normalisation factor for the i-th objective, $penalty_j$ is the penalty factor for the j-th constraint, $Ncon$ is the number of constraints, $ConstntViolation_j$ is the amount by which the j-th constraint is violated, and $Trget_j$ is the target value of the j-th constraint. For a feasible design (all constraints are

satisfied), the performance function is a sum of the normalised objective values. When one or more constraints are violated, the performance value of the design is reduced by a value based on the violation of the constraint (the second term in the equation) [96].

6.4 RESULTS AND DISCUSSION

6.4.1 Temperature and velocity contours

For different cavity receiver wall temperatures, the temperature and velocity distributions inside and near the receiver are similar. As such, this chapter of this thesis only gives temperature and velocity contours of the cavity receiver with T_s = 800 K. Temperature and velocity contours on the symmetry plane of a receiver cavity without fins and one with three plate fins (at H_j/W = 0.15 and t_j/W = 0.075, j = 1, 2, 3) are depicted in Figures 6.4 and 6.5 for Ra = 10^4 and 10^6 respectively. From Figure 6.4a and Figure 6.4b, it is seen that at Ra = 10^4, the temperature contours exhibit a conduction-dominated heat transfer regime for both the finned and unfinned cavity receivers. The velocity contours (Figure 6.4c and Figure 6.4d) are mildly distorted, since buoyancy forces are not strong enough to trigger significant convection and, as such, the plate fins do not play a major role in convection heat transfer.

At a higher Ra, the heat transfer is dominated by the convection zone in the lower part of both the finned and unfinned cavities. The temperature and velocity contours are distorted by the flow, and the fluid penetrates through into the cavity as seen in Figure 6.5(a–d). It

is also noted that the thickness of the hydrodynamic boundary layer adjacent to the hot wall decreases for high Ra = 10^6 for most of the lower part of the cavity.

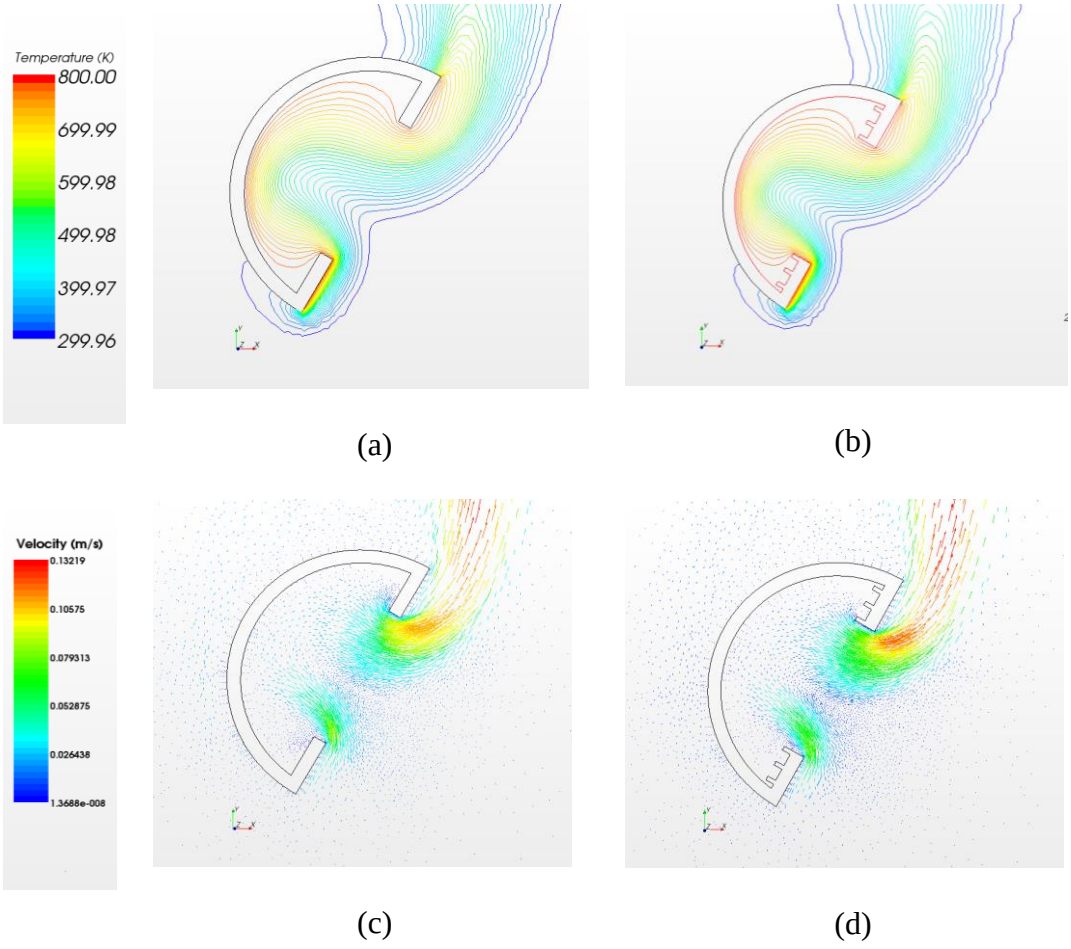

Figure 6.4: Temperature contours and velocity vectors on the symmetry plane respectively, at 60° cavity inclination, Ra = 10^4, H_j/W = 0.15 and t_j/W = 0.075 for unfinned and finned cavities

From Figure 6.5a and Figure 6.5b, it is seen that the temperatures of the lower part of the cavity receiver walls are relatively lower, while the temperatures of the upper parts of the walls are higher. The explanation for this is that as air at ambient temperature is driven into the cavity receiver by the natural convective currents, the air adjacent to the receiver surface becomes hotter and lighter as it absorbs heat from the receiver surfaces and

consequently flows up along the cavity wall. As a result, hot, stagnant air only appears at the top of the cavity receiver. Eventually, hot air leaves the cavity through the aperture and is then cooled by the ambient air.

In the absence of fins, a clockwise-rotating vortex is formed in the lower part of the cavity receiver, as shown in Figure 6.5a and Figure 6.5c. This occurs because of the rise of the fluid due to the buoyancy effects produced by heating from the lower aperture surface. The presence of fin plates attached to the aperture surface has counteracting effects on the flow and temperature fields, as shown in Figure 6.5b and Figure 6.5d. The plate fins tend to create a blockage to flow movement close to the hot aperture wall, which weakens the primary vortex in the lower part of the cavity and reduces heat transfer.

The decrease in convection heat transfer in the cavity can also be attributed to decrease in velocity of fluid flowing through the small cavities created by the plate fins. This is due to the fact that the pre-heated air from the first cavity reaches the entrance of the following cavities causing a large part of the small cavities to be occupied by hot air and leading to poor heat transfer thus preventing the cold air from ambient to enter the small cavities. Hence, the driving potential to natural convection reduces in the cavity, which in turn reduces the net heat transfer.

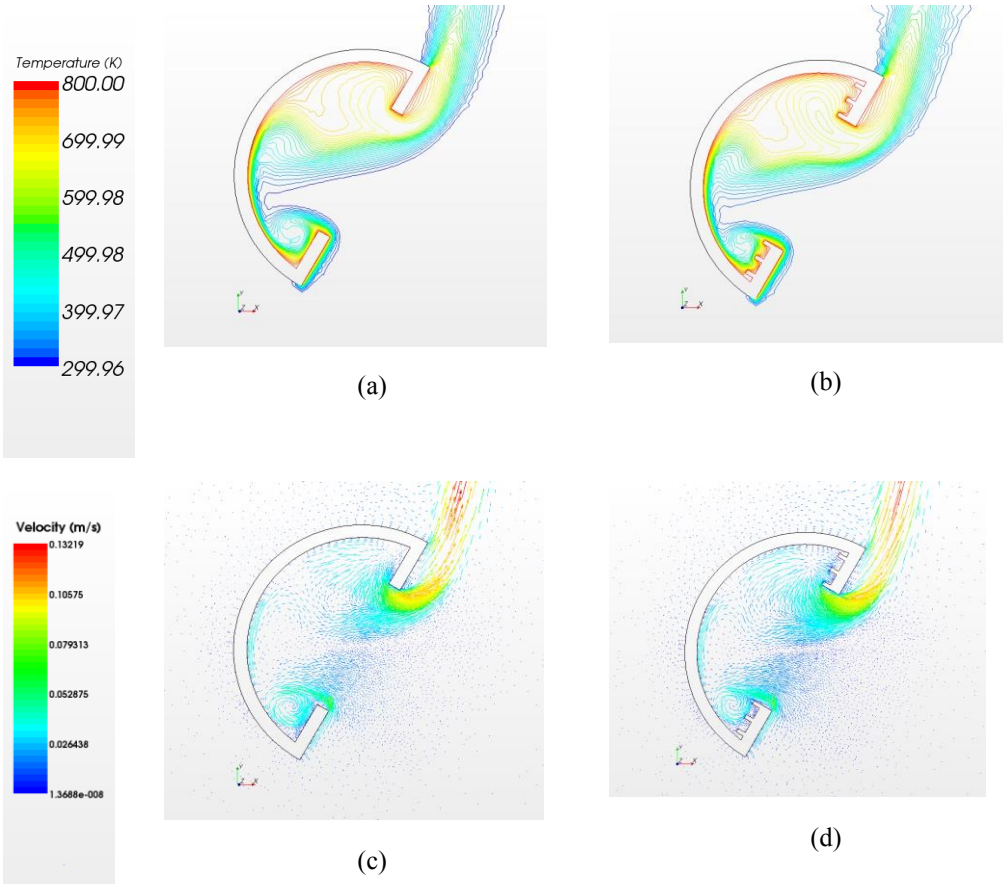

Figure 6.5: Temperature and velocity contours on the symmetry plane respectively at 60º cavity inclination, $Ra = 10^6$, H_j/W = 0.15 and t_j/W = 0.075 for unfinned and finned cavities

6.4.2 Effects of the fin height

Figure 6.6 shows the effect of the dimensionless plate fin heights H_j/W on natural convection heat loss from the proposed cavity receiver. Natural convection heat loss is plotted against plate fin height at a given Ra and temperature for different inclination angles.

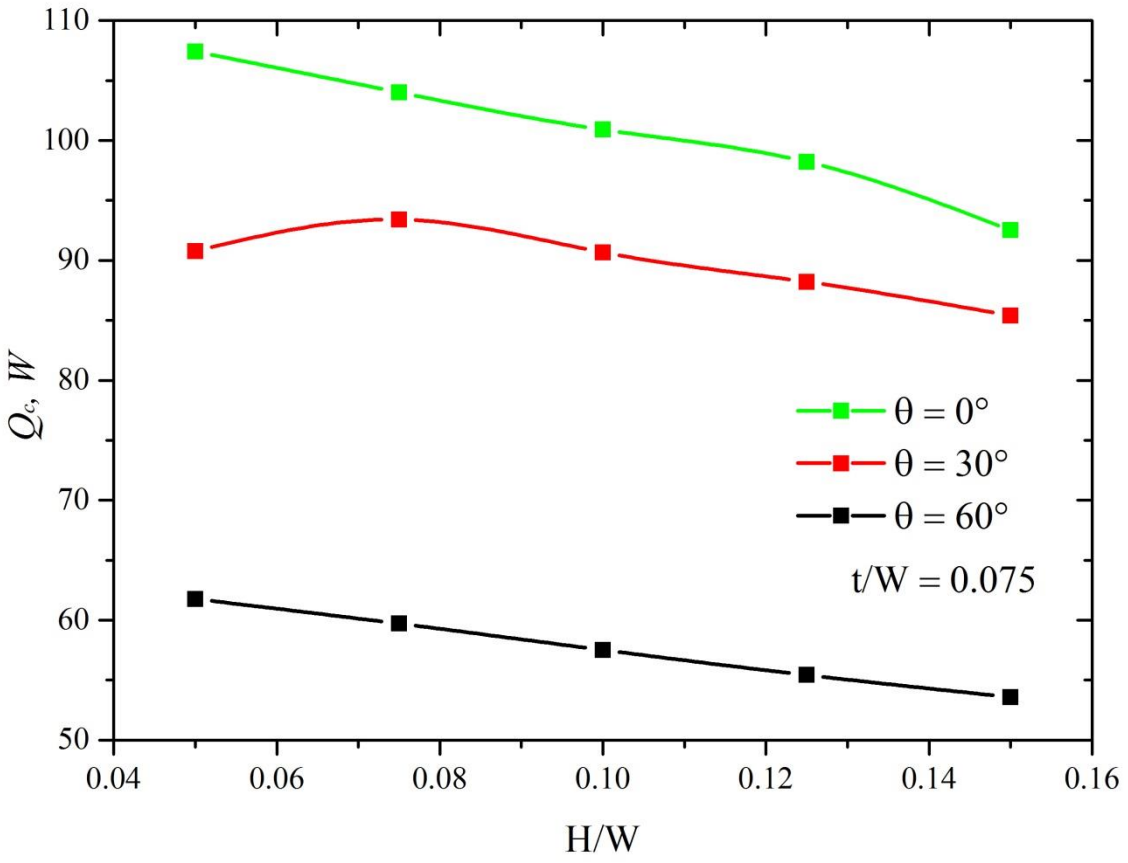

Figure 6.6: The effect of plate fin height on natural convection heat loss from the proposed cavity receiver, $Ra = 10^6$

As seen from Figure 6.6, for any receiver inclination angle of θ, increasing the fin height decreases the natural convection heat loss, and a reduction of 19.6% is observed at all inclination angles. The decrease in natural convection is close to linear for all inclination angles. The decrease in convection heat transfer loss in the proposed cavity with plate fins is attributed to a decrease in the velocity of the fluid flowing through the cavities created by the plate fins, as discussed in Section 4.1. Increasing the fin height increases the resistance of the convection cell movement between the plate fins, thus further decreasing the heat transfer rate. The results show that longer plate fins cause higher

natural convection heat loss suppression compared to shorter plate fins. The conclusion is that the natural convection heat loss from the proposed cavity receiver was reduced when compared to the case without fins. This reduction can be enhanced by increasing the fin height.

6.4.3 Effect of plate fin thickness

The dependence of natural convection heat loss on the dimensionless fin thickness t_j/W in the proposed cavity receiver is shown in Figure 6.7. Natural convection heat loss is plotted against the dimensionless plate fin thickness at a given Ra and temperature for different inclination angles.

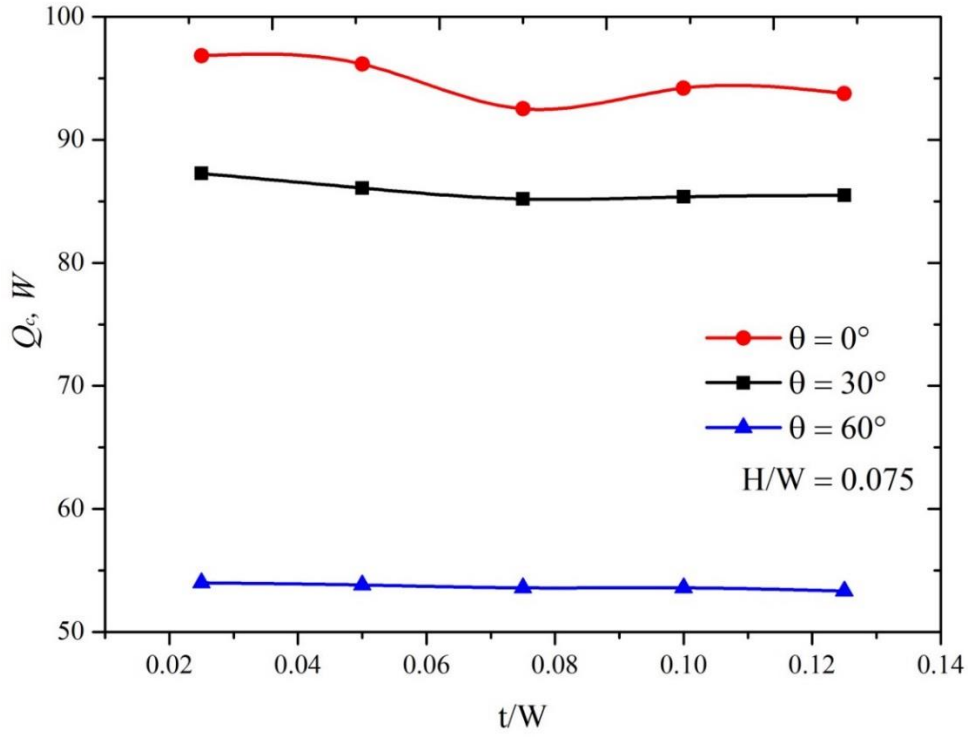

Figure 6.7: Effect of plate fin thickness on natural convection heat loss from the proposed modified cavity, $Ra = 10^6$

As seen from Figure 6.7, at lower inclination angles (between 0 and 30°) it is clear that plate fin thickness optimally exist, which minimizes natural convection heat loss in the cavity. However, natural convection heat loss does not depend much on plate fin thickness, but varies greatly with the inclination angle of the receiver, with the minimum occurring at 60°. Reducing the plate fin thickness will slightly increase the natural convection heat loss, while increasing the plate fin thickness reduces the natural convection heat loss until an optimum thickness is reached, after which the heat loss starts to increase. The decrease in convection heat transfer in the proposed cavity receiver with plate fins is attributed to the fact that, at high fin thickness, the fin spacing (S) is too thin to permit the formation of convection cells between each adjacent two-plate fin. This decreases the transfer rate. On the other hand, reducing plate fin thickness increases fin spacing, thus permitting the formation of convection cells, and the heat transfer rate is slightly increased.

6.4.4 Effects of the Rayleigh number

Figure 6.8 shows the variation of natural convection heat loss with Ra for the cavity receiver. Natural convection heat loss is plotted against Ra for different inclination angles. It can be observed from this figure that, for any cavity receiver orientation, the natural convection heat loss generally increases with increasing Ra. This can be attributed to the increased buoyancy force with increasing Ra. Increasing buoyancy force increases flow driving force and causes an increase in flow intensity that leads to higher heat transfer

rates. Increasing Ra also enhances the mixing within the air layer that leads to higher heat transfer.

It is also observed that the growth in natural convection heat loss at all inclination angles of the cavity receiver is slightly lower at low Ra, compared to that of high Ra. This can be attributed to the fact that heat transfer is dominated by conduction, since buoyancy forces are not strong enough to trigger significant convection at a low Ra.

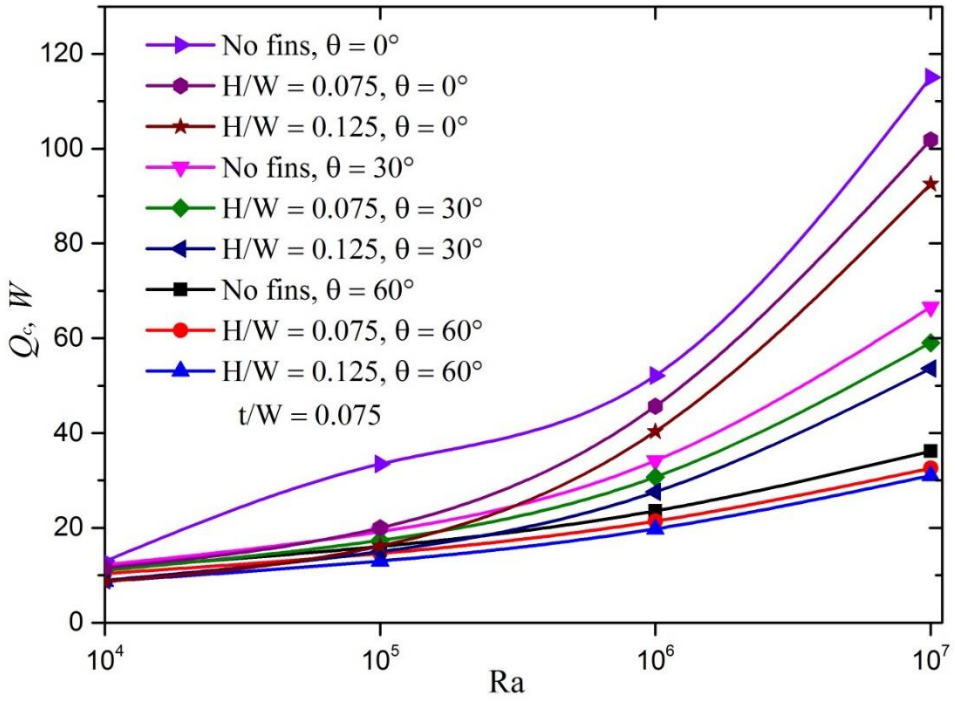

Figure 6.8: The Rayleigh number's effect on natural convection heat loss from the proposed modified cavity

It can be seen from the figure that the introduction of fin plates suppresses natural convection significantly at high Ra compared to low Ra for all inclination angles of the receiver except at 60°. It is also observed that increasing the fin heights further suppresses

natural convection at higher Ra. This can be attributed to the fact that plate fins do not play a significant role at low Ra since heat transfer is dominated by conduction. However, they play a significant role at high Ra, at which heat transfer is dominated by convection, as discussed in Section 4.1. It is further observed that natural convection heat loss at different Ra varies with the inclination angle of the receiver, especially at high Ra.

6.4.5 Effect of the number of fins

The dependence of the natural convection heat loss on the number of plate fins on the aperture of the cavity receiver is shown in Figure 6.9. Natural convection heat loss is plotted against the number of plate fins (N) for different inclination angles and fixed dimensionless fin height and thickness.

It is observed from Figure 6.9 that, for all inclination angles of the cavity receiver, natural convection heat loss decreases with an increasing number of plate fins. This variation of natural convection heat loss with the number of fins can be attributed to a decrease in the flow intensity with the insertion of fins.

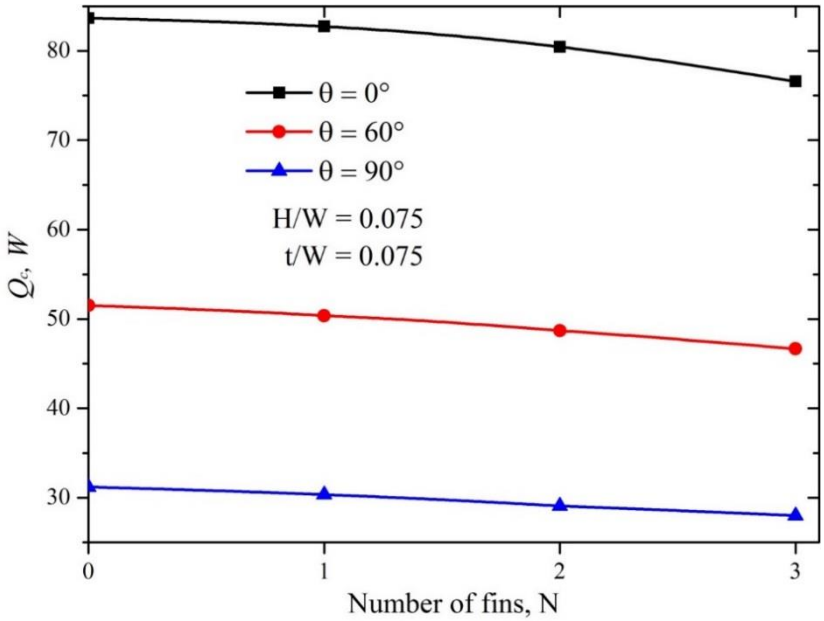

Figure 6.9: Variation of convection heat loss with number of fins, $Ra = 10^6$

The resistance of the motion of the rotating convection cells is expected to increase with the increasing number of fins, and this leads to weaker flow intensity. Decreasing flow intensity reduces the heat transfer rate, thus reducing natural convection heat loss.

6.4.6 Effects of inclination angle

Figure 6.10 shows the effect of the cavity receiver inclination angle on natural convection for the unfinned and finned aperture cases that have three plate fins and $H_j/W = 0.075$ and 0.125 respectively. The figure shows that natural convection heat loss is greater during the side-facing position (0°) when compared to the downward-facing position (90°). This trend was noticed for both the unfinned and finned cases across the entire

range of inclination angles. This can be attributed to the fact that behaviour of air in the cavity receiver is completely different at varying inclination angles of the receiver.

In the downward-facing position of 90^{o}, the cavity is almost dominated by the stagnant zone, thus convection heat loss out of the receiver is small. When the receiver inclination angle is varied anticlockwise, the stagnant zone decreases. This increases the convective zone where most of the heat transfer occurs. It is also observed from the figure that the introduction of plate fins suppresses natural convection for all inclination angles. The suppression is observed to be much higher at lower inclination angles, compared to higher inclination angles.

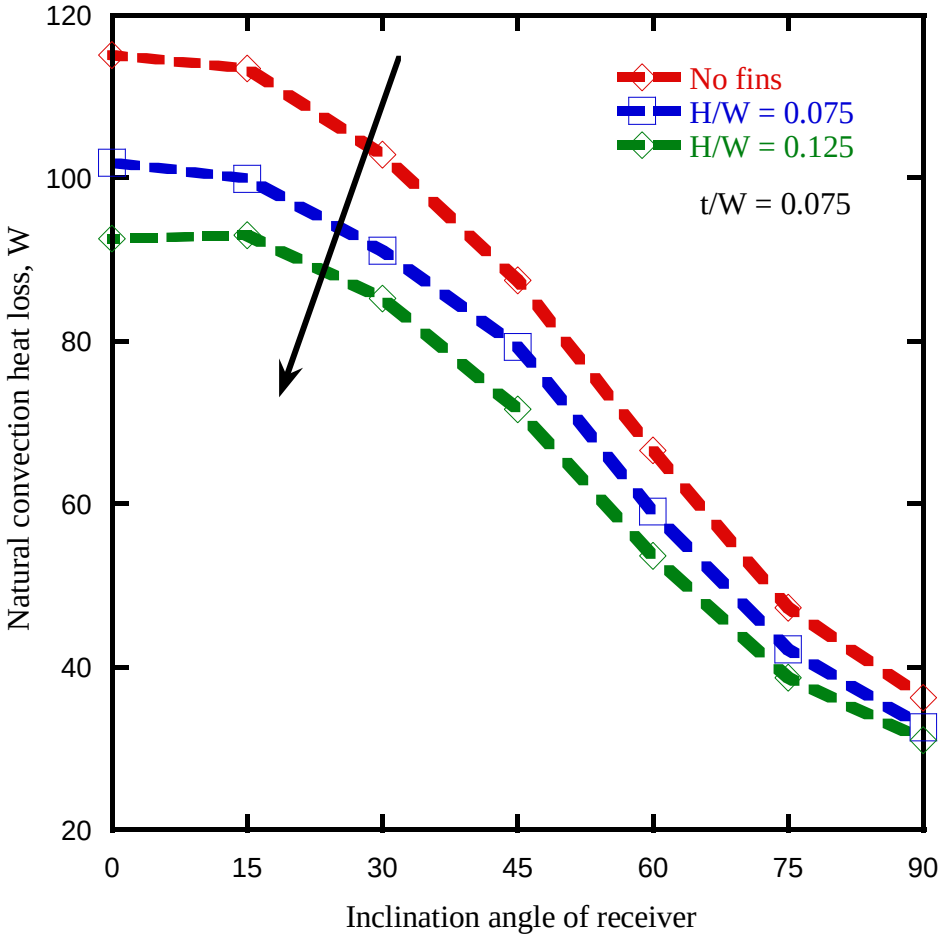

Figure 6.10: Variation of convection heat loss with receiver inclination angle, Ra = 10^6

The increase in fin height further suppresses natural convection for all inclination angles. With the introduction of plate fins H_j/W = 0.125, a reduction in natural convection heat loss of a maximum of 19.6% at 0° and 14.2% at 90° was observed respectively.

6.5 OPTIMISATION RESULTS

In this section, the optimisation SHERPA algorithm was applied to obtain the best geometric configuration of the plate fins that will optimally suppress natural convection

heat loss in the cavity receiver. The optimal geometric parameters have a significant influence on the performance of the receiver cavity, as reducing natural convection will improve the performance of the cavity receiver. A series of numerical optimisation evaluations was conducted automatically within the constraint ranges that are given in Section 4.0. The results are presented in Table 6.3.

Table 6.3: Optimisation results

Variable	Fin height/thickness (m)	
	Initial	Optimised
H_1	0.005	0.006
H_2	0.005	0.006
H_3	0.005	0.006
t_1	0.003	0.005
t_2	0.003	0.005
t_3	0.003	0.005

Figure 6.11 shows optimised results of the cavity receiver plate fin heights at all inclination angles. The optimum results are plotted together with the effect of the cavity receiver inclination angle on natural convection for the unfinned and finned aperture cases that have three plate fins and H_j/W = 0.075 and 0.125 respectively. For the range of inclination angles, Figure 6.11 shows that natural convection heat loss depends on fin height and decreases with increasing plate fin height until the optimum is reached. This is attributed to the decrease in natural convection heat loss as discussed in Section 4.2.

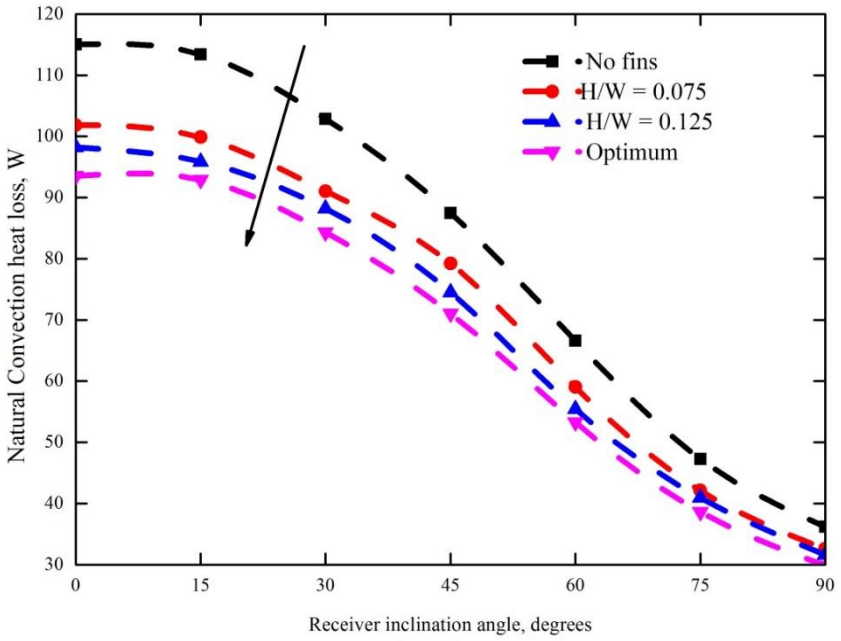

Figure 6.11: Variation of convection heat loss with receiver inclination angle, including optimised results, Ra = 10^6

Figure 6.12 shows the optimised results of the cavity receiver plate fin thicknesses at all inclination angles. The optimum results are plotted together with the effect of the cavity receiver inclination angle on natural convection for the unfinned and finned aperture cases that have three plate fins and t_j/W = 0.075 and 0.125 respectively. Figure 6.12 shows that natural convection heat loss does not depend significantly on plate fin thickness, and varying t_j/W shows insignificant change in natural convection heat loss. However, we observe from the optimisation study that natural convection suppression is achieved when t_j/W = 0.125. Thus, it can be concluded that the plate fins' geometric configuration in

cavity receivers could be important for cavities' optimum performance in practical applications.

Figure 6.13 shows the effects of the minimised natural convection heat loss Q_{min} as a function of the Ra for the various receiver inclination angles. It is observed that minimised natural convection heat loss increases with the increase in Ra for all receiver inclination angles. It is also observed that, at lower Ra (10^4 and 10^5), the variation of minimised natural convection heat loss at different inclination angles of the cavity receiver is lower when compared to that of high numbers (10^6 and 10^7).

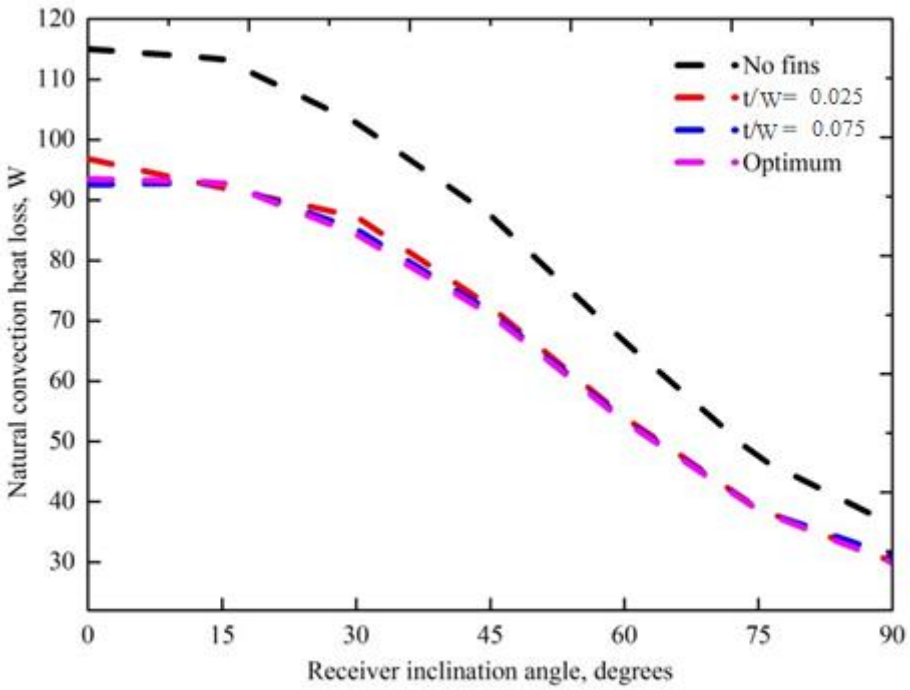

Figure 6.12: Variation of convection heat loss with receiver inclination angle optimised results, Ra = 10^6

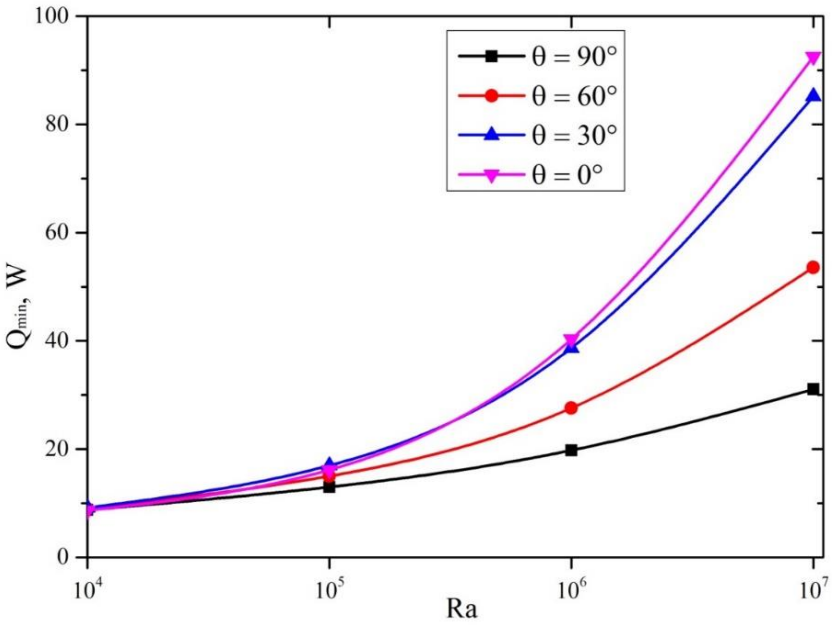

Figure 6.13: The Rayleigh number's effect on minimised natural convection heat loss from the proposed modified cavity

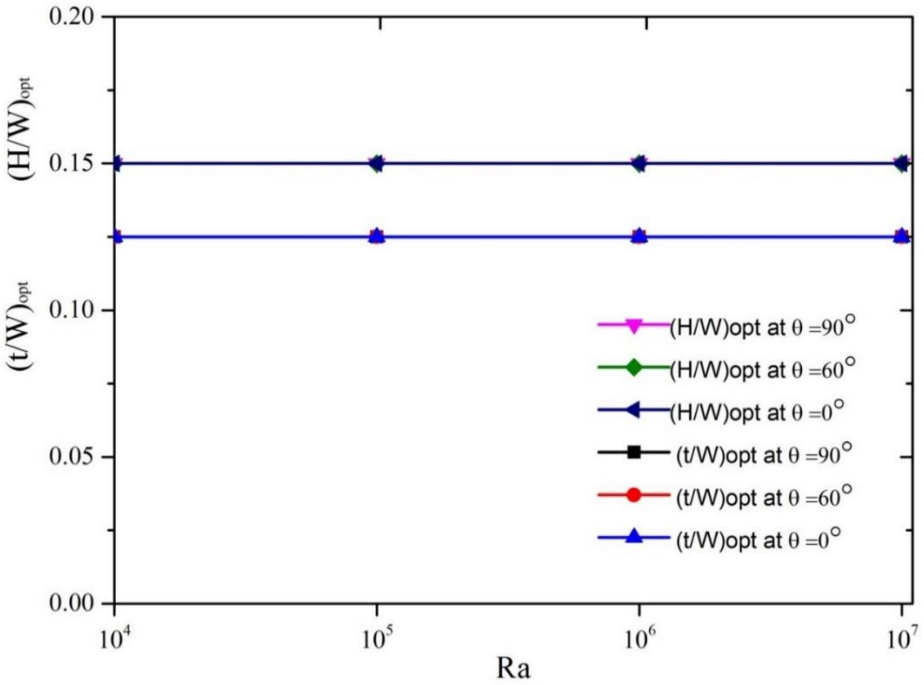

Figure 6.14: The Rayleigh number's effect on optimised dimensionless plate fin heights and thicknesses

Figure 6.14 shows that the optimal dimensionless fin height $(H/W)_{opt}$ and dimensionless fin thickness $(t/W)_{opt}$ were constant values of 0.15 and 0.125 mm respectively for different Ra when the cavity receiver was optimised. It is also observed that the $(H/W)_{opt}$ and $(t/W)_{opt}$ were constant and insensitive to receiver inclination angles for different Ra.

6.6 CONCLUSION

The use of plate fins attached to the inner aperture surface was presented as a possible low-cost means of suppressing natural convection heat loss in a cavity receiver. A three-dimensional numerical model for the heat transfer process in the cavity receiver was presented and the effects of the Ra, inclination angle, and fin height and thickness on natural convection heat loss were investigated. From the temperature contours, a conduction-dominated heat transfer regime for the finned and unfinned cavities was observed for low Ra. The temperature contours are mildly distorted, since buoyancy forces are not strong enough to trigger significant convection.

Consequently, the plate fins do not play a major role in the convection heat transfer at low Ra. At higher Ra, heat transfer is dominated by convection in the lower part of the cavity. The isotherms are distorted by the flow, fluid enters the cavity and fins play a significant role. It was also found that natural convection heat loss depends on the receiver, inclination angle, and fin height and thickness.

The examined geometric parameters were optimised using SHERPA (the HEEDS search algorithm). The major finding is that the natural convection heat loss from the cavity receiver can be significantly reduced by using plate fins, which act as heat transfer suppressors. It was also found that optimal plate fin geometries exist for minimised natural convection heat loss. A reduction of up to a maximum of 19.6% at 0^{o} receiver inclination was observed. The results obtained provide a novel approach for improving the design of cavity receivers for optimal performance.

7

CHAPTER 7: THREE-DIMENSIONAL ANALYSIS AND NUMERICAL OPTIMISATION OF COMBINED NATURAL CONVECTION AND RADIATION HEAT LOSS IN SOLAR CAVITY RECEIVER WITH PLATE FINS INSERT

7.0 INTRODUCTION

The total energy loss of solar receivers plays an important role in the light-to-heat conversion. It comprises of conduction heat loss through the cavity receiver housing, convection and radiation heat loss to the ambient environment through the aperture. However, most of the heat loss is mainly through natural convection and surface radiation, since the cavity receiver is insulated. As a result, it is very important to understand the behaviour of this type of heat transfer mechanism.

Research of heat transfer and flow in the cavity receivers can greatly contribute to the estimation of thermal performance and optimisation of the design [46], [102], [103]. A literature review indicates that numerous studies have been conducted on natural convection heat loss in open cavities [24], [28], [30]–[34], [41]. Although most of the past studies were for pure natural convection, heat transfer actually occurs in cavities through a combination of natural convection and radiation. In this regard, researchers

have carried out some numerical and experimental investigations on combined natural convection and radiation heat transfer in cavities [51]–[57], [59], [64], [65], [119], [120].

Minimising heat loss is viewed as an effective way to enhance the thermal performance of cavity receivers. Some research has been conducted on the reduction of heat loss from cavity receivers. However, fewer studies have been done on cavity enhancement and performance [66], [67], [119]–[123].

Most of the earlier studies used a two-dimensional numerical model and the Boussinesq approximation. However, at a higher temperature, the Boussisneq approximation does not give the correct numerical results. In the present study, a three-dimensional numerical model with non-Boussinesq steady-state combined laminar natural convection and surface radiation heat transfer from a modified cavity receiver (hemispherical) with fin plates was developed and investigated. The influence of operating temperature, emissivity of the surface, orientation and the geometric parameters on the total heat loss from the receiver was investigated. The optimisation was conducted to obtain the optimal fin geometry. The overall thermal efficiency of the receiver was presented at different operating temperatures. In this study, the analysis is based on a parabolic dish/cavity receiver system operating at temperatures between 800 K and 1 200 K.

7.1 PHYSICAL AND MATHEMATICAL MODEL

Figure 7.1a shows the schematics of the cavity receiver proposed by Sendhil Kumar and Reddy [32] and Figure 7.1b the proposed cavity with plate fins in two-dimension. The cavity receiver is usually mounted at the focal point of the parabolic dish solar collector to capture concentrated sunlight from the dish. Both cavity receivers are made of copper tubing with an opening aperture diameter (d) and cavity diameter (D). Circular plate fins have been installed in the proposed cavity receiver (Figure 7.1b) to suppress combined laminar natural convection and radiation heat loss. The diameters of the receiver and its aperture are defined as 180 and 100 mm respectively. The copper tubes are spirally wound to get the shape of the receiver. To reduce heat loss through conduction, the outer surface of the cavity receiver is completely covered with opaque insulation. The following assumptions are made for modelling the cavity receiver: there is uniform and maximum solar flux distribution in the cavity receiver, the surfaces of the tube are uniform and smooth for the prototype cavity receiver, the plate fins are made of copper and installed on the inner side of the aperture surface between the copper tubing, and the temperature of air flowing through the copper tube is the same as the tube's surface temperature. The copper tubes were not considered in the simulation.

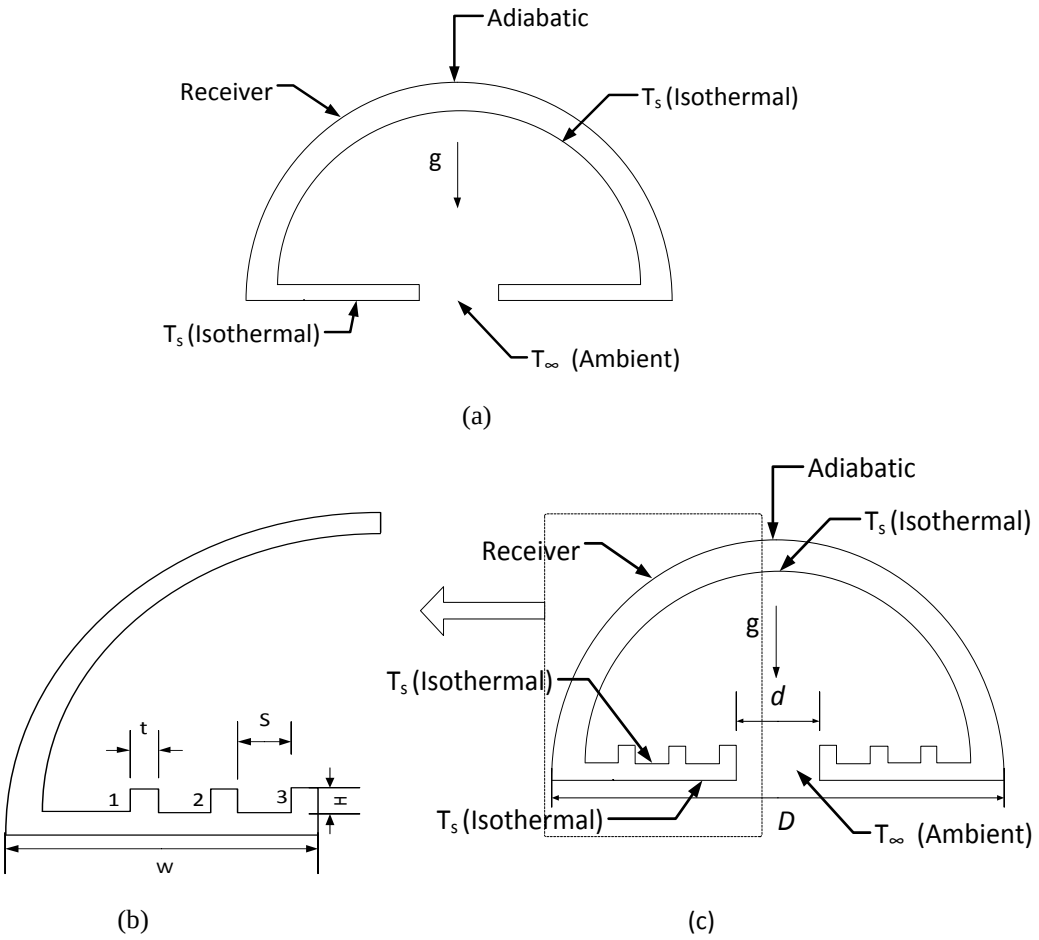

Figure 7.1: Schematic of modified cavity receiver with and without plate fins

The fin height (H_1, H_2, and H_3), thickness (t_1, t_2 and t_3) and number of fins N, as depicted in Figure 7.1b, greatly affect the hydrodynamic performance of the plate fins. The fin height and thickness are defined as dimensionless parameters H_j/W and t_j/W respectively in this study (for j = 1, 2, 3). The dimensionless fin heights were varied in the following range: $0.025 \leq H_j/W \leq 0.15$. The dimensionless thickness of the fins were varied in the range: $0.025 \leq t_j/W \leq 0.125$ and the value of N was varied from 0 to 3,

where $N = 0$ indicates no fin condition. In this study, the effects of the distance between two plate fins (S) was not considered.

Figure 7.2 shows the cavity receiver at the different inclination angles that were used in this study. Figure 7.2a depicts the cavity receiver at an ideal sunrise when the parabolic dish faces east and the cavity receiver aperture faces west. Figure 7.2b depicts the cavity receiver at noon when the sun is directly above both the parabolic dish and the cavity receiver. Figure 7.2c depicts the receiver at an ideal sunset when the parabolic dish faces west and the cavity receiver aperture faces the opposite direction.

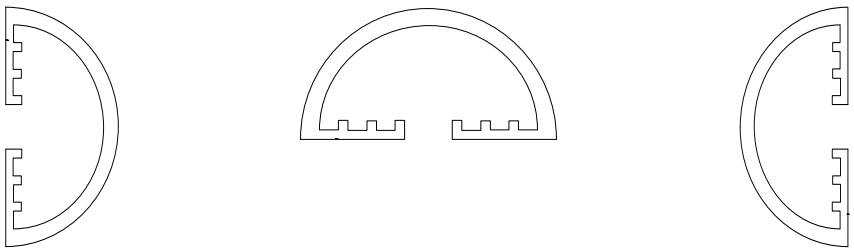

(a) (b) (c)

0° 90° 180°

Figure 7.2: A schematic of a modified cavity receiver at different inclination angles

For natural convection in the cavity receiver, the flow and heat transfer simulations are based on the simultaneous solution of equations that describe the conservation of the system's mass, momentum and energy. The vector form of the continuity, momentum and energy equations can be expressed as follows:

Continuity equation:

$$\Delta \cdot (\rho \mathbf{V}) = 0 \tag{7.1}$$

Momentum equation:

$$\mathbf{V} \cdot \nabla (\rho \mathbf{V}) = \rho \mathbf{X} - \nabla p + \nabla^2 (\mu \mathbf{V}) \tag{7.2}$$

Energy equation:

$$\mathbf{V} \cdot \nabla (\rho c_p T) = \nabla^2 (kT) \tag{7.3}$$

where ρ is the density of air in kg/m^3, $\mathbf{V}$ is the velocity vector of air in m/s, $\mathbf{X}$ is the mass force vector in N/kg, p is the pressure, Pa, μ is dynamic viscosity in kg/(m.s), c_p is the specific heat capacity at constant pressure in J/(kg.K), k is the thermal conductivity of air in W/(m.K) and T is temperature in K.

Since temperatures encountered in concentrated solar thermal systems are high, the Boussinesq approximation is not considered to be appropriate. Consequently, it is not used in this study. Polynomial relationships for density, specific heat capacity at constant pressure and dynamic viscosity are used to account for air property variation with temperature [92].

$$\rho = 7.4992\times10^{-9}T^3 + 1.6487\times10^{-5}T^2 - 1.2366\times10^{-2}T + 3.6508 \tag{7.4}$$

$$c_p = 1.3864\times10^{-13}T^4 - 6.4747\times10^{-10}T^3 + 1.0234\times10^{-6}T^2 - 4.3282\times10^{-4}T + 1.0613 \tag{7.5}$$

$$\mu = 1.3864\times10^{-15}T^3 - 1.4346\times10^{-11}T^2 + 5.0523\times10^{-8}T + 4.1130\times10^{-6} \tag{7.6}$$

$$k = 1.5797\times10^{-17}T^5 + 9.4600\times10^{-14}T^4 + 2.2012\times10^{-10}T^2 - 2.3758\times10^{-7}T^2 + 1.7082\times10^{-4}T^2 - 7.488\times10^{-3} \tag{7.7}$$

The convective heat transfer coefficient can be expressed as:

$$h_c = \frac{Nuk}{D} \tag{7.8}$$

where Nu is the Nusselt number and D is the receiver cavity diameter. The Nusselt numbers were calculated using a CFD code. The convective heat loss from the modified cavity receiver is given as:

$$Q_c = h_c A(T_s - T_\infty) \tag{7.9}$$

The non-Boussinesq laminar natural convection model is solved using the continuity, momentum and energy equations. The radiation heat transfer in the surfaces of the cavity receiver is accounted for by using the S2S model, which is coupled with the laminar natural convection model. In this model, the medium (air in this case) that fills the space

between the surfaces is considered as non-participating. That is, it does not absorb, emit or scatter radiation. Under these circumstances, the radiation properties and the thermal boundary conditions that are imposed on each surface uniquely define the amount of radiation that a surface receives and emits. The surface properties are quantified in terms of emissivity, reflectivity, transmissivity and radiation temperature.

The size, orientation and separation distance between two surfaces are the parameters that effect energy exchange between them. The view factor, which is calculated using the view factor model, is used to account for the effects of these parameters.

To predict the effects of combined natural convection and surface radiation on total heat transfer, the emissivity of the cavity receiver surfaces was varied from 0.2 to unity. The radiant flux from a given surface consists of directly emitted and reflected energy. The reflected energy flux depends on the incident energy flux from the surroundings, which can then be expressed in terms of the energy flux that leaves all other surfaces. The energy reflected from surface *i* is given by [58]:

$$q_{out,i} = \varepsilon_i \sigma T_i^4 + (1-\varepsilon_i) q_{in,i} \tag{7.10}$$

The amount of incident energy on a surface from another surface is a direct function of the S2S view factor, F_{ji}. The incident energy flux $q_{in,i}$ can be expressed in terms of the energy flux leaving all other surfaces as [58]:

$$A_i q_{in,i} = \sum_{j=1}^{N} A_j q_{out,j} F_{ji} \tag{7.11}$$

For N surfaces, view factor reciprocity theorem gives:

$$A_j F_{ji} = A_i F_{ij} \tag{7.12}$$

Therefore, $q_{in,i}$ is expressed as:

$$q_{in,i} = \sum_{j=1}^{N} F_{ji} q_{out,j} \tag{7.13}$$

When Equation 7.13 is substituted into Equation 7.10, the following is found:

$$q_{out,i} = \varepsilon_i \sigma T_i^4 + (1-\varepsilon_i) \sum_{j=1}^{N} F_{ji} q_{out,j} \tag{7.14}$$

Equation 7.14 can be written as:

$$J_i - (1-\varepsilon_i) \sum_{j=1}^{N} F_{ij} J_j = E_i \tag{7.15}$$

Also,

$$J_i = E_i + (1-\varepsilon_i) \sum_{j=1}^{N} F_{ij} J_j \tag{7.16}$$

$$\sum_{j=1}^{N}(\delta_{ij}-(1-\varepsilon_i)F_{ij})J_j = E_i \tag{7.17}$$

where

$$\delta_{ij} = \begin{cases} 1 & \text{when } i = j \\ 0 & \text{when } i \neq j \end{cases}$$

The radiosity equation is expressed in vector form as:

$$KJ = E \tag{7.18}$$

where K is an $N \times N$ matrix, $K = (\delta_{ij} - (1-\varepsilon_i)F_{ij})$, J is the radiosity vector and E is the emissivity power vector.

The radiative heat transfer coefficient and its corresponding heat loss can be written as:

$$h_R = \frac{Nuk}{D} \tag{7.19}$$

$$Q_R = h_R A(T_s - T_\infty) \tag{7.20}$$

Conduction has not been considered in this study.

Therefore, the total heat loss from the cavity receiver can be expressed as:

$$Q_{total} = Q_c + Q_R \tag{7.21}$$

7.1.1 Thermal performance

Thermal performance is estimated by estimating the incident power flux distribution using the Gaussian sun shape. The overall receiver efficiency can be estimated as a function of surface temperature and receiver aperture radius using an equation from Steinfeld and Schubnell [124]. Although the assumption of Gaussian distribution is not suitable for high-quality parabolic dishes, the difference in overall efficiency compared with the more accurate pillbox-shaped sun was found to be about 8% [124], justifying its use in estimating overall efficiency in this study.

The solar energy absorption efficiency of a cavity receiver, $\eta_{absorption}$, is defined as the net rate at which energy is absorbed divided by the power coming from the concentrator. This is given by:

$$\eta_{absorption} = \frac{Q_{net} - Q_{total}}{P_{in}} \tag{7.22}$$

$$Q_{net} = \alpha_{eff} P_{aperture} \tag{7.23}$$

$$P_{in} = 2\pi\lambda^2 F_{peak} \tag{7.24}$$

$$P_{aperture} = 2\pi\lambda^2 F_{peak}\left[1 - \exp\left(\frac{-r^2}{2\lambda^2}\right)\right] \tag{7.25}$$

where F_{peak} is the peak flux, λ denotes the standard deviation and α_{eff} is the effective absorption. The overall idealised cavity receiver efficiency can be represented as:

$$\eta_{overall} = \eta_{absorption}\left(1-\frac{T_\infty}{T_s}\right) \tag{7.26}$$

In this analysis, it is assumed that α_{eff} = 1. For a given incident flux distribution, there is an optimum operating temperature and optimum radius for which overall efficiency is at its maximum. In this study, a graph plotted using a simple method described by Steinfeld and Schubnell [124] is used to obtain the optimum operating temperatures used for a range flux distribution as shown in Table 7.1.

Table 7.1: Peak flux density and corresponding operating temperature

Peak flux density (MW/m^2)	Optimum operating temperature (K)
0.58	800
1.18	900
2.17	1000
3.70	1100
6.08	1200

7.2 NUMERICAL PROCEDURE AND VALIDATION

7.2.1 Numerical procedure

A finite volume-based CFD code, STAR-CCM+ 7.06, was employed in the three-dimensional simulation of the natural convection through the aperture of the cavity receiver. Figure 7.3 schematically represents the cavity receiver's computational grid. In reality, the receiver is surrounded by an infinite atmosphere with a limiting temperature that is equal to ambient air temperature. In the numerical analysis, the region outside the cavity is represented by a spherical enclosure (Figure 7.3a). The size of the enclosure was increased until it had an insignificant effect on fluid and heat flows in the vicinity of the receiver. It was found that in STARCCM+, the diameter of the spherical enclosure should be about ten times the diameter of the receiver to achieve this.

The core volume mesh contains polyhedral cells. The cells were refined on the cavity receiver's walls as a percentage of base cell and prism layer cells were used (Figure 7.3b). This led to cells being very small inside the cavity and near the receiver, but gradually increasing in size towards the spherical enclosure wall. The prism layer mesh model was used with a core volume mesh to generate orthogonal prismatic cells next to wall boundaries. An enlarged portion of the mesh is shown in Figure 7.3b and Figure 7.3c.

A mesh refinement on the cavity receiver investigated the average Nusselt number on the hot inner surfaces of the cavity receiver (T_s = 800 K and $Ra = 10^6$). Table 7.2 presents the average Nusselt numbers that were obtained for four different grids at two different inclination angles of the receiver ($\theta = 0°$ and $\theta = 30°$).

The relative deviation for the Nusselt number between Grid 1 and Grid 2 was less than 1%. Since the differences between the two were minor, Grid 2 was chosen for all the simulations in this study. This was considered a good trade-off between accuracy and cost of time.

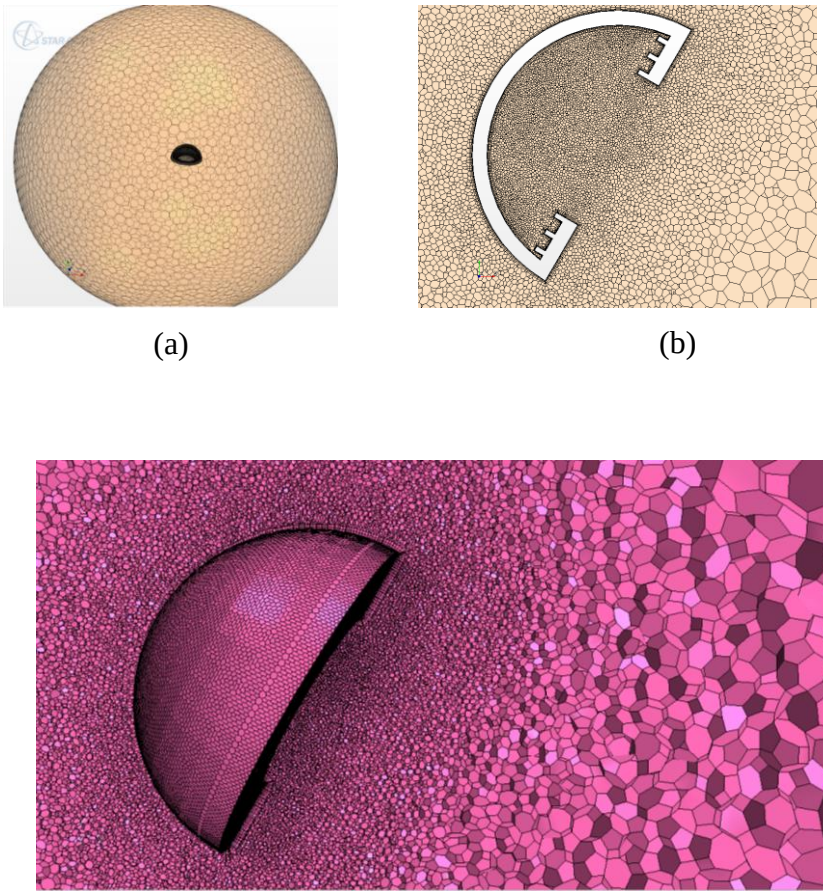

(a) (b)

(c)

Figure 7.3: A typical computational grid for the numerical analysis of the modified cavity receiver: (a) three-dimensional including sphere; (b) two-dimensional cross-section at 30º; (c) refined polyhedral cells are in and around the cavity at 30º and the coarse mesh

Table 7.2: Average Nusselt numbers for different grids

Grid number	Cells	Nusselt number			
		$\theta = 0^o$	Relative deviation	$\theta = 30^o$	Relative deviation
1	801,337	10.1675		18.2941	
2	320,000	10.1529	0.001436	18.2734	0.001132
3	241,336	10.2338	-0.00797	18.2008	0.003973
4	218,272	10.2947	-0.00595	18.2096	-0.00048

7.2.1.1 Boundary conditions

The isothermal boundary condition was applied to the internal receiver surfaces, outer surface on the aperture plane, as well as the fins. The temperature was varied from 800 K to 1 200 K and radiation heat transfer in the surfaces of the cavity receiver is accounted for by using the S2S model. The outer spherical walls of the receiver were treated as adiabatic, since they were covered with insulation to prevent heat loss. The outer domain was treated as a pressure outlet boundary condition. The wall temperature of the entire spherical enclosure was set to an ambient temperature of 300 K. The properties of the working fluid were taken based on the average temperature of the cavity receiver surface and the ambient temperature.

7.2.2 Validation

In the present model, a non-Boussinesq numerical procedure has been used to solve natural convection and surface radiation. However, available literature does not investigate a separate non-Boussinesq combined natural convection and surface radiation heat transfer model for a modified hemispherical cavity receiver.

Hence, a low-temperature Boussinesq natural convection and surface radiation heat model for a modified cavity has been considered to validate the findings with a low-temperature non-Boussinesq heat transfer model. At a lower temperature, the Boussinesq and non-Boussinesq models give the same results. By using the present numerical non-Boussinesq procedure, the natural convection Nusselt number has been predicted for the modified cavity receiver and compared with the developed Nusselt number correlations for the modified cavity receiver [24].

Since there is no three-dimensional data for the radiation heat transfer for a modified cavity, the predicted radiation Nusselt number from the present study is compared with the developed radiation Nusselt number correlation for a two-dimensional modified cavity model [58]. To perform this, Grashof numbers of 10^5 and 10^6 at 400 K and emissivity of 0.5 and 1.0 have been taken. The results are given in Table 7.3.

For natural convection, it was observed that the present numerical procedure is in good agreement with the Nusselt number based on the modified cavity with a maximum deviation of 4%. However, for the radiation Nusselt number, the deviation is up to 16.91%, which is attributed to the fact that the present study used a three-dimensional model and compared it with a two-dimensional model. This is in agreement with the prediction of Reddy and Sendhil Kumar [24] that there is a deviation of about 14.5% between two-dimensional and three-dimensional simulations in a modified cavity receiver.

Table 7.3: Validation of the numerical procedure for natural convection and radiation heat loss

Configuration	Grashof number	Nusselt number type	Nusselt number		Percentage of deviation
			Reported	Present study	
Modified cavity [24]	1.4085×10^{6}	Convective - 90^{o}	12.43	12.25	1.45
Improved		Convective - 75^{o}	15.53	16.00	3.03
	1.4085×10^{5}	Convective - 90^{o}	7.68	7.99	-4.04
		Convective - 75^{o}	9.60	9.26	3.76
Modified cavity [58]	1.4085×10^{6}	Radiative - $\varepsilon = 0.5$	11.56	12.56	-8.65
		Radiative - $\varepsilon = 1.0$	16.87	14.02	16.91

7.3 OPTIMISATION PROBLEM FORMULATION

The optimisation problem was tailored to finding the best plate fin geometric parameters that give the least natural convection and radiation heat loss from the modified receiver cavity. The design of the plate fin heights and thicknesses greatly affect the hydrodynamic performance of plate fins. The dimensionless fin heights were varied in the following range: $0.025 \leq H_j/W \leq 0.15$. The dimensionless thicknesses of the fins were varied in the range: $0.025 \leq t_j/W \leq 0.125$. The type of optimisation considered in this study is the placement of individual plate fins to form channels. This leads to the treatment of an array of fins in which each fin operates optimally [118].

The optimisation problem was solved using Optimate+, which is an add-on to the CFD code Star CCM+, that adds the capability to perform automated design optimisation

studies using SHERPA [96]. Details of the process are explained by Ngo, Bello-Ochende and Meyer [125].

7.4 RESULTS AND DISCUSSION

7.4.1 Effects of receiver inclination angle

Figure 7.4 and Figure 7.5 show the variation of heat loss with receiver inclination angle for surface emissivity of 0.2 and 1.0 at an operating temperature of 800 K respectively. It is observed from both figures that the convective heat loss reaches a maximum at 0^o (cavity aperture facing sideways towards the east), but starts to decrease as the inclination angle increases, until a minimum is reached at 90^o when the receiver is facing downwards. This can be attributed to the fact that, as the receiver inclination angle increases from 0 to 90^o, the receiver is initially dominated with the convective zone (where most of the heat transfer happens) at 0^o, which starts to decrease with increasing inclination angle. At 90^o, the cavity receiver is dominated by the stagnant zone, thus convection heat loss out of the receiver is at a minimum.

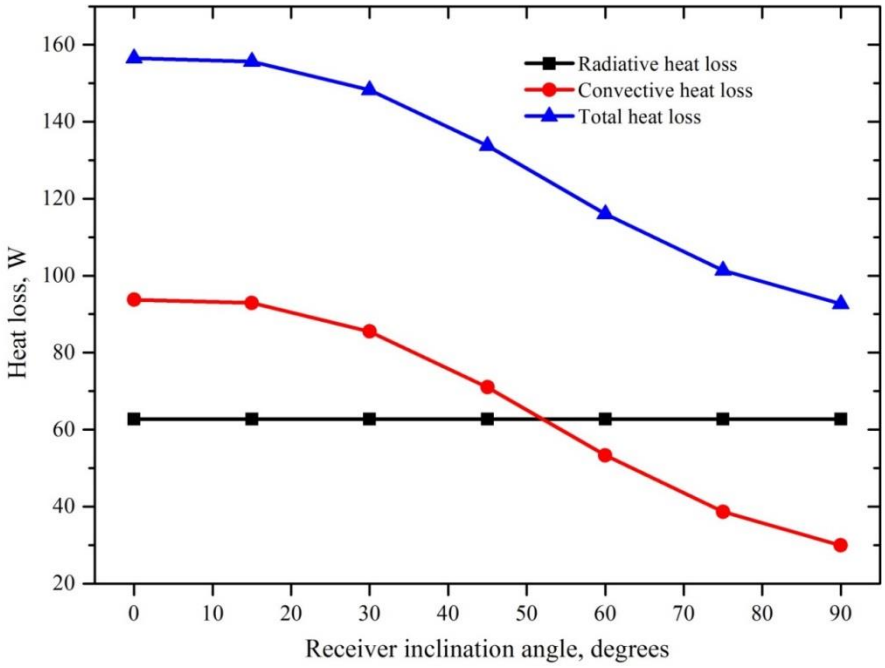

Figure 7.4: Variation of heat loss with cavity receiver inclination angle, ε = 0.2 at 800 K

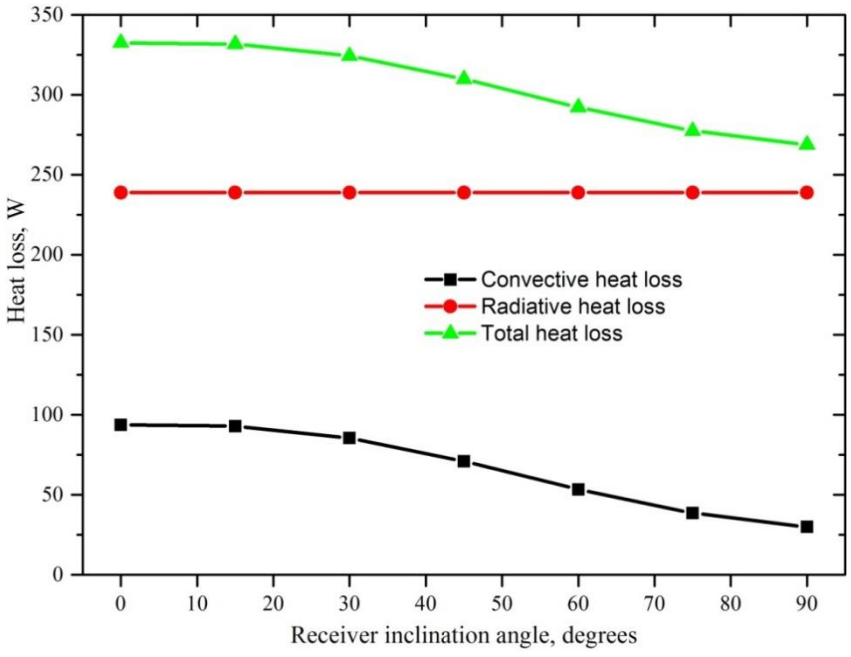

Figure 7.5: Variation of heat loss with cavity receiver inclination angle, ε = 1.0 at 800 K

From Figure 7.4, it is observed that at lower emissivity (0.2), the convective heat loss is higher than the radiative heat loss at lower inclination angles (0 to 50^{o}). This is due to the fact that the cavity is mostly occupied by the convective zone. However, for angles between 50 and 90^{o}, the radiative heat loss is higher than the convective heat loss. This can be attributed to the increase in the stagnation zone where convective heat loss is low. It is observed from Figure 7.5 that the radiative heat loss dominates when the emissivity is increased to 1.0 for all inclination angles and the radiative heat is observed to remain constant at all inclination angles, which means that radiative heat loss is not influenced by the inclination angle.

7.4.2 Effects of fin plates

Figure 7.6 shows the effects of fins on combined natural convection and radiation heat loss from the cavity receiver. Combined natural convection and radiation heat loss is plotted for different inclination angles for the cavity receiver with fins and without fins at an operating temperature of 800 K. It is observed from Figure 7.6 that the inclusion of fins decreases both the natural convection and radiation heat loss from the cavity receiver. It is also observed in both cases that the radiative heat loss is more dominant and constant at all inclination angles. The decrease in convection heat transfer in the cavity receiver with plate fins is attributed to a decrease in the velocity of the fluid flowing through the cavities created by the plate fins. The fins increase the resistance of the convection cell movement between the plate fins, which further decreases the convective heat loss.

The conclusion is that the combined natural convection and radiation heat loss from the cavity receiver with fins was reduced compared to the case without fins. Convective heat loss is significantly reduced by approximately 20% at 0^o and 10% at 90^o with the introduction of fin plates. Radiation heat loss is minimally reduced by 5% at all inclination angles.

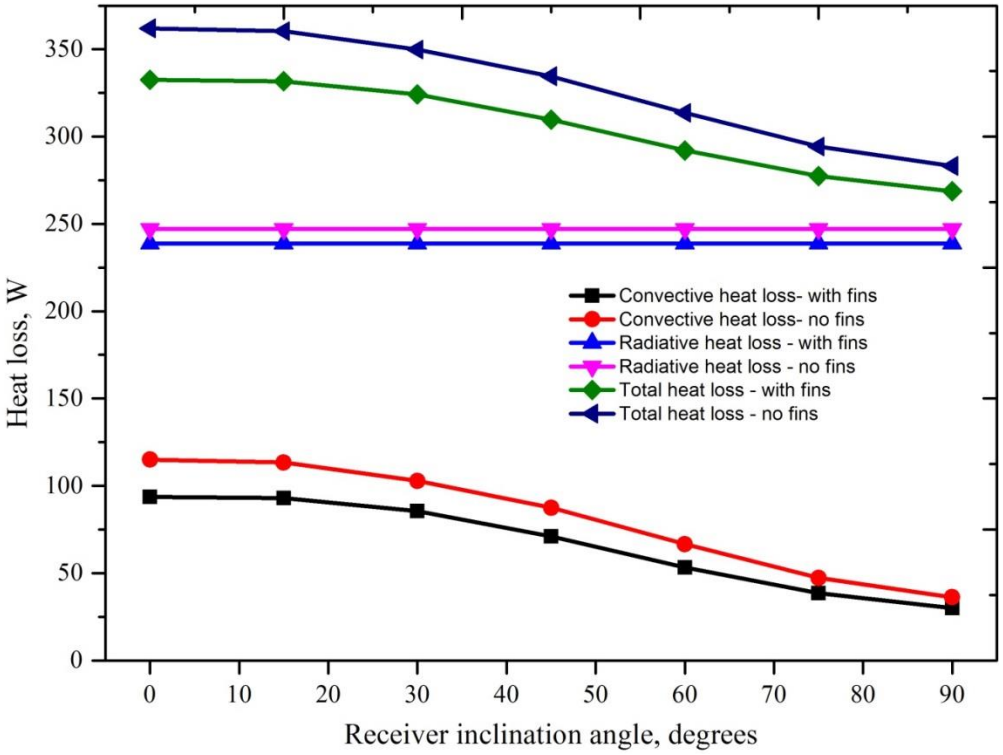

Figure 7.6: Variation of heat loss with receiver cavity inclination angle at an operating temperature of 800 K

7.4.3 Effects of number of fins

The dependence of the combined natural convection radiation heat loss on the number of plate fins on the aperture of the cavity receiver is shown in Figure 7.7. Combined natural convection and radiation heat loss is plotted against the number of plate fins for different inclination angles, emissivity of 1.0 and fixed fin height and thickness. It is observed from

Figure 7.7 that, for all inclination angles of the cavity receiver, combined natural convection and radiation heat loss decreases with an increasing number of plate fins. This variation of combined natural convection and radiation heat loss with the number of fins can be attributed to the decreasing flow intensity with fin insertion. The resistance of the motion of the rotating convection cells is expected to increase with the increasing number of fins and this leads to weaker flow intensity. Decreasing flow intensity reduces the heat transfer rate, thus reducing the natural convection heat loss and, as such, the total heat loss.

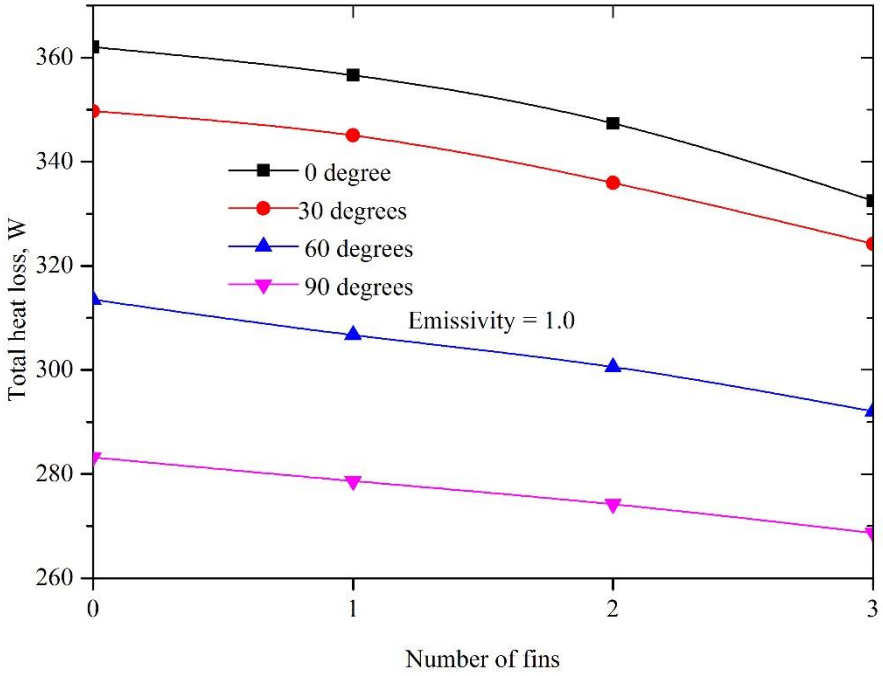

Figure 7.7: Variation of total heat loss with number of fins for ε = 1.0 at 800 K.

7.4.4 Effects of surface emissivity

The effects of emissivity on total combined natural convection and heat loss on the cavity receiver has been investigated for different inclination angles. For a given Ra and temperature, the total heat loss varies linearly with emissivity for all inclination angles, as seen from Figure 7.8. There is a sharp increase in the total heat loss with increasing surface emissivity. This can be attributed to the fact that radiative heat loss increases with increasing emissivity in the receiver. The emissivity of the cavity receiver surface directly influences surface radiation, which also increases the radiative heat loss and total heat loss as a whole. The greatest heat loss occurs at 90^o and 1.0 emissivity and the least heat loss is estimated at 0^o when the emissivity is 0.2.

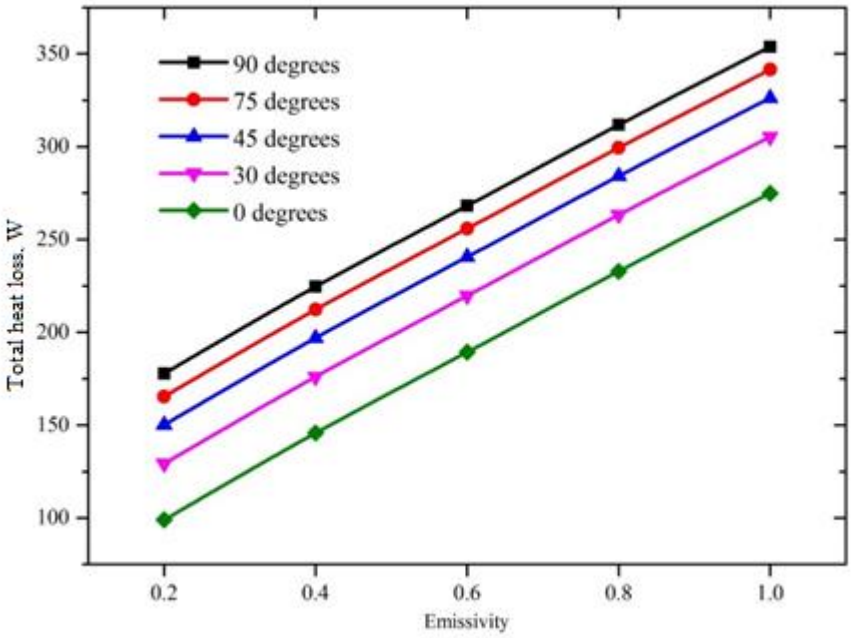

Figure 7.8: Variation of total heat loss with receiver cavity emissivity at 800 K for N = 3.

7.4.5 Effects of surface temperature

To show the effects of temperature on combined natural convection and radiation heat transfer, the temperature of the cavity receiver was varied from 800 K to 1 200 K. For a given dimensionless fin height (H/W = 0.125m), fin thickness (t/W = 0.075m), emissivity (1.0) and Ra (1×10^6), the temperature contours of the cavity receiver at a given inclination angle and surface temperatures are shown in Figure 7.9a and Figure 7.9b. It is observed from the cavity receiver at 800 K and at 60^o inclination angle (Figure 7.9a) that the thickness of the stagnation zone in the top part of the cavity is higher compared to that of the corresponding cavity at 1 200 K (Figure 7.9b).

In both cases, the temperature of the lower part of the cavity receiver walls are relatively lower, while the temperature of the upper parts of the walls are higher. As air at ambient temperature is driven into the cavity receiver by the natural convective currents, the air adjacent to the receiver surface becomes hotter and lighter as it absorbs heat from the receiver surfaces and consequently flows up along the cavity wall. Consequently, hot, stagnant air only appears at the top of the cavity receiver. Eventually, the hot air leaves the cavity through the aperture and is then cooled by the ambient air.

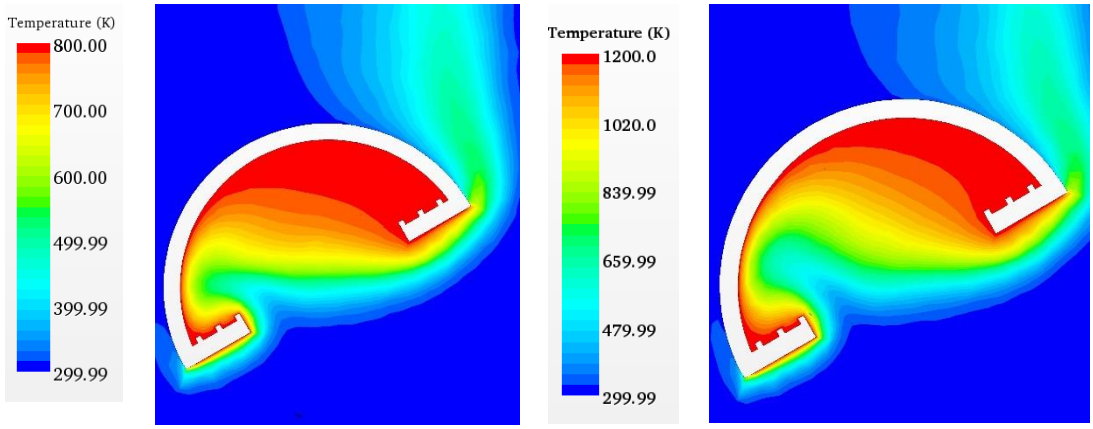

(a) (b)

Figure 7.9: Temperature contours for cavity receivers with three plate fins at 60° for Ra = 10^6 with surface temperature at 800 K and 1 200 K

The temperature contours are distorted by the flow and the fluid penetrates through into the cavity. It is observed that the fluid penetrates more into the cavity at high temperature (Figure 7.9b) compared to the cavity at lower temperature (Figure 7.9a). It is also noted that the thickness of the hydrodynamic boundary layer adjacent to the hot wall decreases in both cases.

Figure 7.10 shows the variation of combined natural convection and radiation heat loss with temperature for a given emissivity ε = 1.0, Ra (1×10^6) at different inclination angles of the cavity receiver. It is observed from the graph that radiation heat loss varies greatly with increasing temperature, but remains constant for all inclination angles. Natural convection heat loss on the other hand varies steadily with increasing temperature, and depends on the inclination angle of the receiver. It is observed that natural convection is at a minimum at 90^o and highest at 0^o. Because of the higher

radiation heat loss, which is constant at all inclination angles, the total combined natural convection and radiation heat is also high and varies greatly with temperature.

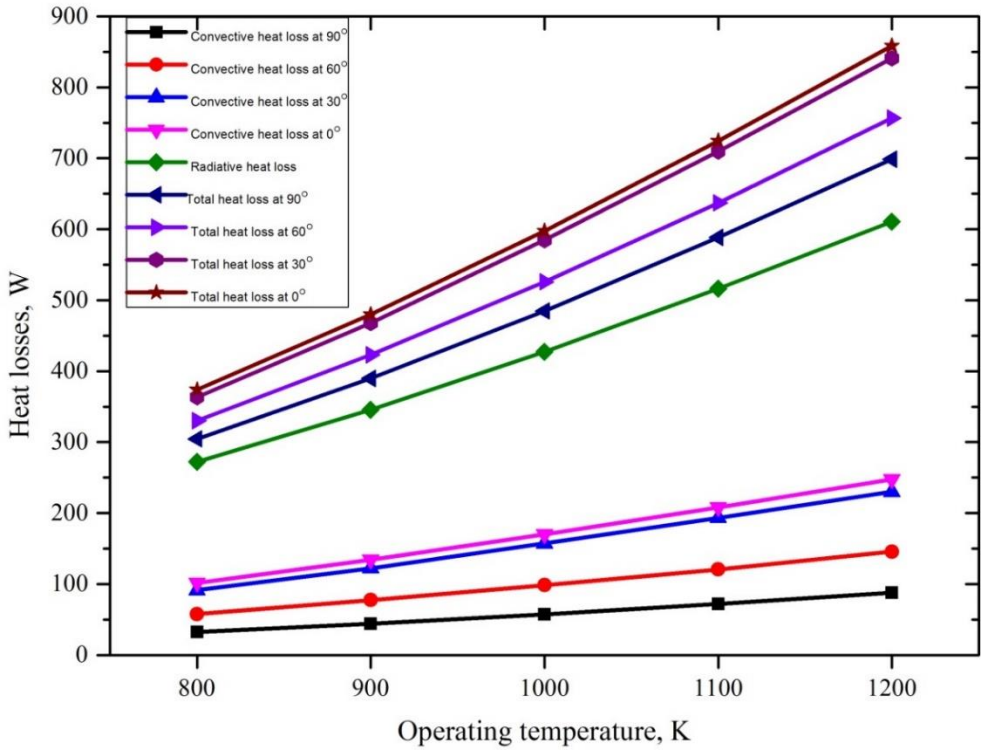

Figure 7.10: Variation of combined natural convection and radiation heat loss with temperature

7.4.6 Optimisation results

In this section, the optimisation SHERPA algorithm was applied to obtain the best geometric configuration of the plate fins that will optimally suppress combined natural convection and radiation heat loss in a cavity receiver. The optimal geometric parameters significantly influence the performance of the receiver cavity, as the reduction of total heat loss will improve the performance of the cavity receiver. For each simulation, 30 optimisation numerical evaluations were conducted automatically within the constraint

ranges given in Section 4.0, and convergence was attained after approximately 14 hours. The results are presented in Table 7.4.

Table 7.4: Optimisation results

Variable	Fin height/thickness (m)	
	Initial	Optimised
H_1	0.005	0.006
H_2	0.005	0.006
H_3	0.005	0.006
t_1	0.003	0.005
t_2	0.003	0.005
t_3	0.003	0.005

7.4.7 Thermal efficiency

Figure 7.11 and Figure 7.12 illustrate the change trends of overall cavity receiver efficiency when the optimum operating temperature varies from 800 K to 1 200 K. The results show that the overall cavity receiver efficiency increases with increasing operating temperature. It is observed from Figure 7.11 that the overall cavity receiver varies marginally with increasing inclination angles. The cavity receiver at 90^o is seen to have a slightly higher efficiency compared to when the cavity receiver is at 0^o. This is attributed to the fact that there is higher convective heat loss at this angle, which is discussed in Section 7.4.1.

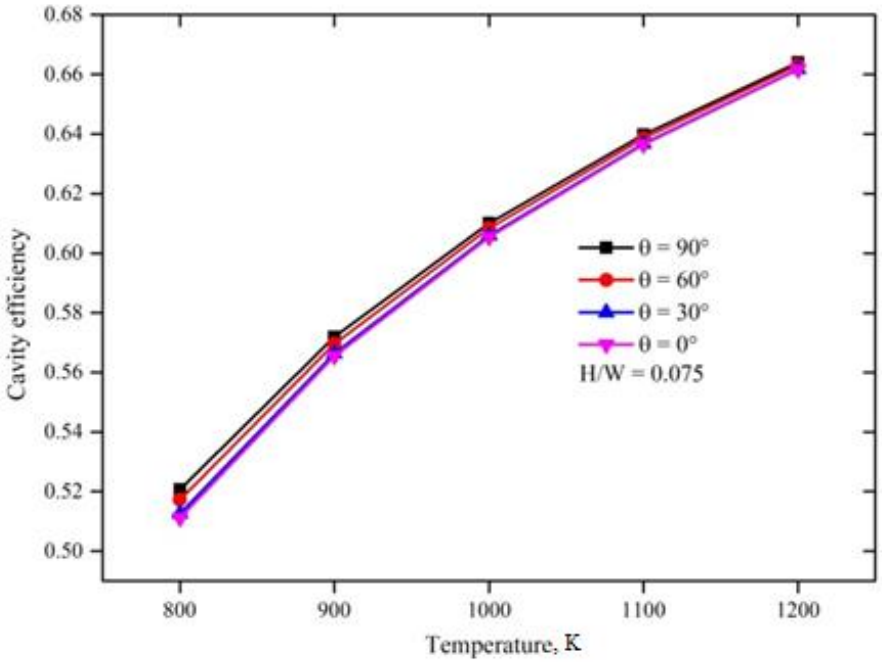

Figure 7.11: Variation of cavity receiver efficiency and operating temperature at different inclination angles

Figure 7.12 shows that the increase in overall cavity efficiency is marginal at approximately 2% with the insertion of fin plates, although the convective heat loss decreases by 20%. This is due to the fact that radiation heat loss dominates at high operating temperatures when compared to convective heat loss. This supports the conclusion of other researchers. From Figure 7.12, it can be concluded that the cavity's overall efficiency increases with the introduction of fin plates and optimum geometry exits, as the results show in Table 7.4 for maximum cavity receiver efficiency.

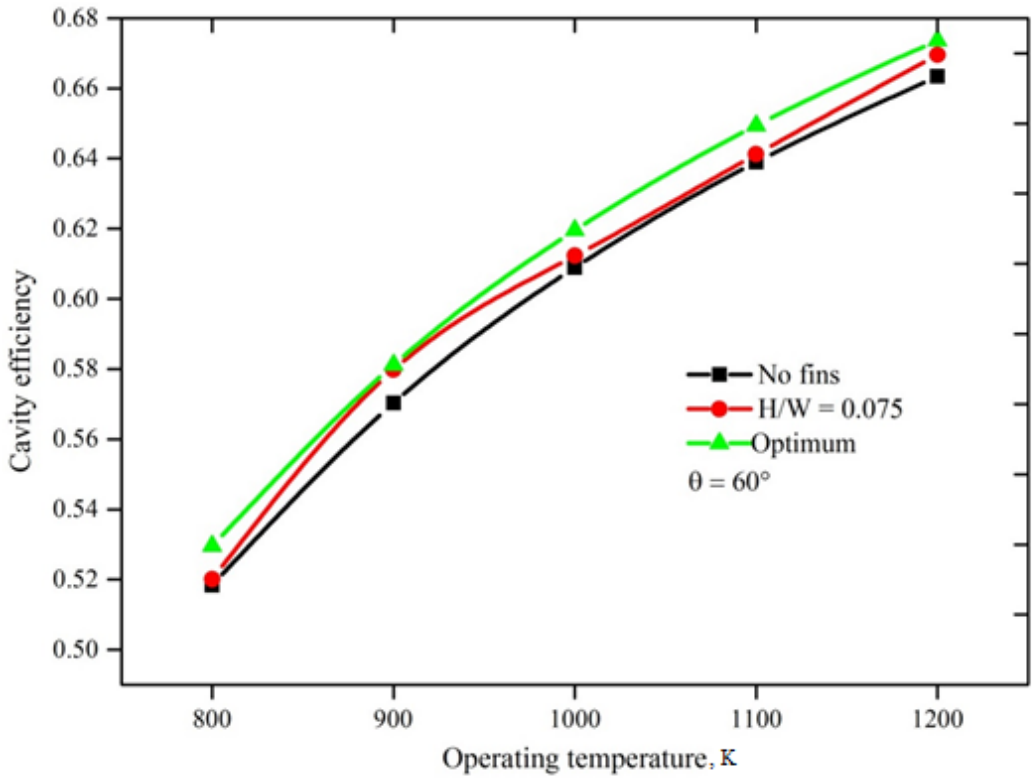

Figure 7.12: The effect of fin plates on cavity receiver efficiency and operating temperature

7.5 CONCLUSIONS

The numerical study of combined laminar natural convection and surface radiation heat transfer in a cavity receiver with plate fins was presented in this chapter. The influence of operating temperature, emissivity of the surface, orientation and the geometric parameters on the total heat loss from the receiver was investigated. It is observed that convective heat loss from the cavity receiver is significantly influenced by the inclination and presence of plate fins in the receiver, whereas the radiation heat loss is considerably affected by the receiver's surface properties. The radiative heat was constant at all inclination angles.

The major finding is that plate fins can significantly reduce natural convection heat loss from the cavity receiver by about 20%, while radiation heat loss is marginally reduced by about 5%. When natural convection was studied together with radiation, the overall cavity efficiency marginally increased by approximately 2% with the insertion of fin plates in the cavity receiver, although the convective heat loss was suppressed by about 20%. This occurs because radiation heat loss dominates at high operating temperatures when compared to convective heat loss. This supports other researchers' conclusions that radiation heat loss dominates at higher temperatures.

8

CHAPTER 8: SUMMARY, CONCLUSIONS AND RECOMMENDATIONS

8.1 SUMMARY

Currently, fossil fuels are still affordable when compared to renewable energy sources, including solar energy. However, fossil fuels are finite and are the major contributor to environmental pollution, which has a negative impact on agriculture, as well as the health, social and economic condition of the populace. Hence, this has led to more research on the development of carbon-free energy sources that are environmentally friendly, sustainable and readily available as an alternative to fossil fuels. In this regard, the parabolic dish receiver assembly, which uses the abundant solar energy resource, is a promising system.

Factors that can improve performance and ultimately help achieve the commercialisation of a parabolic dish receiver system have been explored in this thesis. The present study focused on developing novel approaches that aim to enhance thermal performance for this type of concentrated solar thermal system through the reduction of heat loss in the cavity receiver. The use of combined numerical modelling and automated optimisation ensures effective and accurate predictions of cavity receiver performance under different operating conditions.

8.2 CONCLUSIONS

The main conclusions from this study can be summarised as follows:

(1) In the first part of the study, a numerical investigation was conducted on a modified cavity receiver to quantify the natural convection heat loss and to determine the effects of the operating temperature, receiver inclination angle and aperture size on the heat loss. This study also accounted for the effects of the variation of air properties using polynomial relationships for density, specific heat capacity at constant pressure and dynamic viscosity. The main findings from this study were the following:

- ❖ Convective heat loss varied non-linearly with receiver angle inclination at high operating temperatures. Convection heat loss was at a minimum for all operating temperatures when the receiver aperture was facing downwards. The maximum heat loss occurred when the receiver aperture was orientated at 0^{o}.

- ❖ Convective heat loss increased tremendously with increasing receiver operating temperatures. The effect of inclination angle on convection heat loss was not very significant at lower operating temperatures compared with higher operating temperatures, where it was significantly higher.

- ❖ Convection heat loss increased with increasing aperture size. However, the increase in convection heat loss at 75 and 90^{o} was minimal in comparison with the increase at other inclination angles. This led to the conclusion that the effect of aperture size on convection heat loss is closely related to the inclination angle of the receiver.

- ❖ The comparison between the Boussinesq and the non-Boussinesq fluid models showed some agreement at lower operating temperatures with a maximum deviation of 6.1%. However, the deviation was much higher at higher operating temperatures, with a maximum deviation of 19.48%, thus concluding that the Boussinesq model is not reliable at higher temperatures.

(2) In the second part of this study, the use of plate fins attached to the inner aperture surface was presented as a possible low-cost means of suppressing natural convection heat loss in a cavity receiver, and the geometric parameters were optimised. The main findings from this study were the following:

- ❖ Conduction dominated heat transfer for both the finned and unfinned cavities at low Ra. The temperature contours are mildly distorted since buoyancy forces are not strong enough to trigger significant convection. Therefore, the plate fins do not play a major role in convection heat transfer. However, at higher Ra, heat transfer is dominated by convection and fins play a significant

role. It was also found that natural convection heat loss depends on the receiver, the inclination angle, and the height and thickness of the fins.

- A significant reduction in the natural convection heat loss from the cavity receiver was achieved using plate fins that act as heat transfer suppressors. It was also concluded that optimal plate fin geometries exist for minimised natural convection heat loss. Reduction up to a maximum of 19.6% at 0^o receiver inclination was observed. The results obtained provide a novel approach for improving the design of the cavity receivers for optimal performance.

(3) In the last part of the research, the numerical study of combined laminar natural convection and surface radiation heat transfer in a cavity receiver with plate fins was presented. The main findings from this study were the following:

- Convective heat loss from the cavity receiver is significantly influenced by the inclination and presence of plate fins in the receiver, whereas radiation heat loss is considerably affected by the surface properties of the receiver.

- Radiative heat loss was observed to be constant at all inclination angles. Natural convection heat from the cavity receiver was significantly reduced by 20% using plate fins, while radiation heat loss was marginally reduced by about 5%.

- The overall cavity efficiency marginally increased by approximately 2% with the insertion of fin plates, although the convective heat loss was suppressed by about 20%. This is due to the fact that radiation heat loss dominates at higher operating temperatures compared to convective heat loss. This supports the conclusion by other researchers that radiation heat loss dominates at higher temperatures.

It is hoped that the results of this study will usefully contribute to the literature in this field and enhance understanding of the improvement of the thermal performance of cavity receivers. The approach of reducing heat loss in the cavity receiver to improve performance can also help commercialise this type of technology at low cost to compete favourably with fossil fuel-based technologies. This approach can also be used to reduce heat losses in different types of cavities that use air as the working fluid.

8.3 RECOMMENDATIONS

The numerical methodologies and models presented in this study could be further improved and/or extended in the following directions:

- In the models presented, assumptions of isothermal boundary conditions were applied on the cavity receiver walls. It is necessary to evaluate cavity receiver performance under the actual solar heat flux to assess its influence on the model.

- In the models presented, the copper tubing that makes up the cavity receiver was not part of the model and can be included in the future so that more parameters, such as pipe diameter and fluid flow, can be considered in both the numerical analysis and the optimisation.

- The model considered in this study did not consider forced convection from ambient winds and it is necessary to include this in the model to assess its influence on the performance of cavity receivers with fin plates.

- The proposed model should be studied experimentally and the results should be compared with the numerical results.

REFERENCES

[1] International Energy Agency (IEA), "World outlook executive summary," 2013. [Online] Available: http://www.iea.org/ [Accessed: 13-Dec-2014].

[2] International Energy Agency (IEA), "World energy outlook executive summary", 2012. [Online] Available: http://www.iea.org/publications/ [Accessed: 13-Dec-2014].

[3] The Secretary-General High Level Group, "Sustainable energy for all a framework for action", 2012. [Online] Available: http://www.se4all.org/ [Accessed: 13-Dec-2014].

[4] O. Behar, A. Khellaf and K. Mohammedi, "A review of studies on central receiver solar thermal power plants", Renew. Sustain. Energy Rev., vol. 23, pp. 12–39, Jul. 2013.

[5] CSP & CPV Today, "An overview of CSP in Europe, North Africa and the Middle East", 2008. [Online] Available: http://www.csptoday.com/reports/ [Accessed: 13-Dec-2014].

[6] Desertec Foundation, "An overview of the Desertec Concept", 2010. [Online] Available: http://mragheb.com/ [Accessed: 13-Dec-2014].

[7] S. O. Obayopo, "Performance enhancement in proton exchange membrane fuel cell – numerical modeling and optimisation", University of Pretoria, 2012.

[8] S. A. Kalogirou, *Solar Energy Engineering*. Elsevier, 2009, pp. 1–48.

[9] European Academies Science Advisory Council, "Concentrating solar power: its potential contribution to a sustainable energy future", 2011. [Online] Available: http://www.easac.eu/fileadmin/Reports/ [Accessed: 13-Dec-2014].

[10] W.B. Stine and M. Geyer, *Power from the sun*. 2001. [Online] Available: http://www.powerfromthesun.net/book.html [Accessed: 14-Dec-2014].

[11] L. Feierabend, "Thermal model development and simulation of cavity-type solar central receiver systems", 2009.

[12] H. R. W. Stine and B. William, *Solar energy fundamentals and design: with computer applications*. Wiley, 1985.

[13] SBC Energy Institute, "Concentrating solar power", 2013. [Online]. Available: https://www.sbc.slb.com/ [Accessed: 14-Dec-2014].

[14] "Renewable energy sources", 2014. [Online] Available: https://newenergyportal.wordpress.com/ [Accessed: 14 December 2014].

[15] P. R. Fraser, "Stirling dish system performance prediction model", 2008.

[16] G. C. Bakos and C. Antoniades, "Techno-economic appraisal of a dish/stirling solar power plant in Greece based on an innovative solar concentrator formed by elastic film", *Renew. Energy*, vol. 60, pp. 446–453, 2013.

[17] R. Klein, "Integrated product development", 2014. [Online] Available: http://ryanpklein.com/portfolio-index/#/integrated-product-development/ [Accessed: 14 December 2014].

[18] B. W. A. Duffie and A. John, *Solar engineering of thermal processes*, 3rd ed.. Wiley, 2006.

[19] V. Goldberg, G. Thomas, R. B Diver, C. E. Andraka, K. Scott Rawlinson and T. A. Moss, "Status of the advanced dish development system project", *ASME 2003 International Solar Energy Conference*, 2003, pp. 637–646.

[20] T. Mancini, P. Heller, B. Butler, B. Osborn, W. Schiel, V. Goldberg, R. Buck, R. Diver, C. Andraka and J. Moreno, "Dish-stirling systems: an overview of development and status", *J. Sol. Energy Eng.*, vol. 125, no. 2, p. 135, 2003.

[21] P. R. Fraser, "Stirling dish system performance prediction model", University of Wisconsin-Madison, 2008.

[22] J. P. Holman, *Heat Transfer*, 8th ed.. McGraw-Hill, 1997.

[23] S-Y. Wu, L. Xiao, Y. Cao and Y-R. Li, "Convection heat loss from cavity receiver in parabolic dish solar thermal power system: a review", *Sol. Energy*, vol. 84, no. 8, pp. 1342–1355, 2010.

[24] K. S. Reddy and N. Sendhil Kumar, "An improved model for natural convection heat loss from modified cavity receiver of solar dish concentrator", *Sol. Energy*, vol. 83, no. 10, pp. 1884–1892, 2009.

[25] P. Le Quere, J. A. Humphery and F. S. Sherman, "Numerical calculation of thermally driven two-dimensional unsteady laminar flow in cavities of rectangular cross section", *Numer. Heat Transf.*, vol. 4, pp. 249–283, 1981.

[26] F. Penot, "Numerical calculation of two-dimensional natural convection in isothermal open cavities", *Numer. Heat Transf.*, vol. 5, pp. 421–437, 1982.

[27] A. M. Clausing, "An analysis of convective losses from cavity solar central receivers", *Sol. Energy*, vol. 27, no. 4, pp. 295–300, 1981.

[28] A. M. Clausing, "Convective losses from cavity solar receivers – comparisons between analytical predictions and experimental results", *ASME J. Sol. Energy Eng.*, vol. 105, no. 1, pp. 29–33, 1983.

[29] A. M. Clausing, J. M., Waldvogel and L. D., Lister, "Natural convection from isothermal cubical cavities with a variety of side-facing apertures", *J. Heat Transfer*, vol. 109, no. 2, pp. 407–412, 1987.

[30] J. A. Harris and T. G. Lenz, "Thermal performance of solar concentrator/cavity receiver systems", *Sol. Energy*, vol. 34, no. 2, pp. 135–142, 1985.

[31] P. Siangsukone and K. Lovegrove, "Modelling of a 400m steam based paraboloidal dish concentrator for solar thermal power production", no. November, pp. 79–85, 2003.

[32] N. Sendhil Kumar and K. S. Reddy, "Numerical investigation of natural convection heat loss in modified cavity receiver for fuzzy focal solar dish concentrator", *Sol. Energy*, vol. 81, no. 7, pp. 846–855, 2007.

[33] N. Sendhil Kumar and K. S. Reddy, "Comparison of receivers for solar dish collector system", *Energy Convers. Manag.*, vol. 49, no. 4, pp. 812–819, 2008.

[34] S. Y. Wu, L. Xiao and Y. R. Li, "Effect of aperture position and size on natural convection heat loss of a solar heat-pipe receiver", *Appl. Therm. Eng.*, vol. 31, no. 14–15, pp. 2787–2796, 2011.

[35] S. Paitoonsurikarn, K. Lovegrove, G. Hughes and J. Pye, "Numerical investigation of natural convection loss from cavity receivers in solar dish applications", *J. Sol. Energy Eng.*, vol. 133, no. 2, p. 021004, 2011.

[36] L. Xiao, S-Y. Wu and Y-R. Li, "Natural convection heat loss estimation of solar cavity receiver by incorporating a modified aperture ratio", *IET Renew. Power Gener.*, vol. 6, no. 2, p. 122, 2012.

[37] M. Prakash, S. B. Kedare and J. K. Nayak, "Numerical study of natural convection loss from open cavities", *Int. J. Therm. Sci.*, vol. 51, pp. 23–30, 2012.

[38] J. O. Juárez, J. F. Hinojosa, J. P. Xamán and M. P. Tello, "Numerical study of natural convection in an open cavity considering temperature-dependent fluid properties", *Int. J. Therm. Sci.*, vol. 50, no. 11, pp. 2184–2197, 2011.

[39] M. Pavlović and F. Penot, "Experiments in the mixed convection regime in an isothermal open cubic cavity", *Exp. Therm. Fluid Sci.*, vol. 4, no. 6, pp. 648–655, 1991.

[40] H. Skok, S. Ramadhyani and R. J. Schoenhals, "Natural convection in a side-facing open cavity", *Int. J. Heat Fluid Flow*, vol. 12, no. 1, pp. 36–45, 1991.

[41] M. Prakash, S. B. Kedare and J. K. Nayak, "Investigations on heat losses from a solar cavity receiver", *Sol. Energy*, vol. 83, no. 2, pp. 157–170, 2009.

[42] M. Prakash, S. B. Kedare and J. K. Nayak, "Determination of stagnation and convective zones in a solar cavity receiver", *Int. J. Therm. Sci.*, vol. 49, no. 4, pp. 680–691, 2010.

[43] W. Chakroun, M. M Elsayed and S. F. Al-Fahed , "Experimental measurements of heat transfer coefficient in a partially/fully opened tilted cavity", *Sol. Energy Eng.*, no. 119, pp. 298–302, 1997.

[44] T. Taumoefolau and K. Lovegrove, "An experimental study of natural convection heat loss from a solar concentrator cavity receiver at varying orientation", *Proceedings of Solar – Australian and New Zealand Solar Energy Society Paper 1*, 2002.

[45] T. Taumoefolau, S. Paitoonsurikarn, G. Hughes and K. Lovegrove, "Experimental investigation of natural convection heat loss from a model solar concentrator cavity receiver", *J. Sol. Energy Eng.*, vol. 126, no. 2, p. 801, 2004.

[46] D. J. Reynolds, M. J. Jance, M. Behnia and G. L. Morrison, "An experimental and computational study of the heat loss characteristics of a trapezoidal cavity absorber", *Sol. Energy*, vol. 76, no. 1–3, pp. 229–234, 2004.

[47] T. Melchior, C. Perkins, A. W. Weimer and A. Steinfeld, "A cavity-receiver containing a tubular absorber for high-temperature thermochemical processing using concentrated solar energy", *Int. J. Therm. Sci.*, vol. 47, no. 11, pp. 1496–1503, 2008.

[48] M. S. Patil, R. S. Jahagirdar and E. R. Deore, "Experimental investigation of heat loss from hemispherical solar concentrator receiver", *Front. Heat Mass Transf.*, vol. 3, no. 3, pp. 1–5, 2012.

[49] S-Y. Wu, J-Y. Guan, L. Xiao, Z-G. Shen and L-H. Xu, "Experimental investigation on heat loss of a fully open cylindrical cavity with different boundary conditions", *Exp. Therm. Fluid Sci.*, vol. 45, pp. 92–101, 2013.

[50] Q. Zhang, X. Li, Z. Wang, C. Chang and H. Liu, "Experimental and theoretical analysis of a dynamic test method for molten salt cavity receiver", *Renew. Energy*, vol. 50, pp. 214–221, 2013.

[51] C-X. Lin, S-Y. Ko and M-D. Xin, "Effects of surface radiation on turbulent free convection in an open-ended cavity", *Int. Commun. Heat Mass Transf.*, vol. 21, no. 1, pp. 117–129, 1994.

[52] C. Balaji and S. P. Venkateshan, "Interaction of surface radiation with free convection in a square cavity", *Int. J. Heat Fluid Flow*, vol. 14, no. 3, pp. 260–267, 1993.

[53] C. Balaji and S. P. Venkateshan, "Interaction of radiation with free convection in an open cavity", *Int. J. Heat Fluid Flow*, vol. 15, no. 4, pp. 317–324, 1994.

[54] C. Balaji and S. P. Venkateshan, "Combined conduction, convection and radiation in a slot", *Int. J. Heat Fluid Flow*, vol. 16, no. 2, pp. 139–144, 1995.

[55] S. Singh and S. Venkateshan, "Numerical study of natural convection with surface radiation in side-vented open cavities", *Int. J. Therm. Sci.*, vol. 43, no. 9, pp. 865–876, 2004.

[56] J. F. Hinojosa, R. E. Cabanillas, G. Alvarez and C. E. Estrada, "Nusselt number for the natural convection and surface thermal radiation in a square tilted open cavity", *Int. Commun. Heat Mass Transf.*, vol. 32, no. 9, pp. 1184–1192, 2005.

[57] J. F. Hinojosa, C. Estrada, R. E. Cabanillas and G. Alvarez, "Numerical study of transient and steady-state natural convection and surface thermal radiation in a horizontal square open cavity", *Numer. Heat Transf. Part A Appl.*, vol. 48, no. 2, pp. 179–196, 2005.

[58] K. S. Reddy and N. Sendhil Kumar, "Combined laminar natural convection and surface radiation heat transfer in a modified cavity receiver of solar parabolic dish", *Int. J. Therm. Sci.*, vol. 47, no. 12, pp. 1647–1657, 2008.

[59] N. Sendhil Kumar and K.S. Reddy, "Investigation of convection and radiation heat losses from modified cavity receiver of solar parabolic dish using asymptotic computational fluid dynamics", *Heat Transf. Eng.*, vol. 31, no. 7, pp. 597–607, 2010.

[60] M. M. Gonzalez, J. H. Palafox and C. A. Estrada, "Numerical study of heat transfer by natural convection and surface thermal radiation in an open cavity receiver", *Sol. Energy*, vol. 86, no. 4, pp. 1118–1128, 2012.

[61] S. K. Natarajan, K. S. Reddy and T. K. Mallick, "Heat loss characteristics of trapezoidal cavity receiver for solar linear concentrating system", *Appl. Energy*, vol. 93, pp. 523–531, 2012.

[62] S-Y. Wu, F. H. Guo and L. Xiao, "Numerical investigation on combined natural convection and radiation heat losses in one side open cylindrical cavity with constant heat flux", *Int. J. Heat Mass Transf.*, vol. 71, pp. 573–584, 2014.

[63] K. S. Reddy and Ravi Kumar, "Estimation of convective and radiative heat losses from an inverted trapezoidal cavity receiver of solar linear Fresnel reflector system", *Int. J. Therm. Sci.*, vol. 80, pp. 48–57, 2014.

[64] M. Dehghan and A. Behnia, "Combined natural convection – conduction and radiation heat transfer in a discretely heated open cavity", *Heat Transf.*, vol. 118, no. 1, pp. 56–64, 1996.

[65] N. Ramesh and W. Merzkirch, "Combined convective and radiative heat transfer in side-vented open cavities", *Int. J. Heat Fluid Flow*, vol. 22, no. 2, pp. 180–187, 2001.

[66] A. Kribus, P. Doron, R. Rubin, J. Karni, R. Reuven, S. Duchan and E. Taragan, "A multistage solar receiver", *Sol. Energy*, vol. 67, no. 1–3, pp. 3–11, 1999.

[67] T. Hahm, H. Schmidt-Traub and B. Lebmann, "A cone concentrator for high-temperature solar cavity-receivers", *Sol. Energy*, vol. 65, no. 1, pp. 33–41, Jan. 1999.

[68] R. Rubin, J. Karni and A. Kribus, "The 'porcupine': a novel high-flux absorber for volumetric solar receivers", *J. Sol. Energy Eng. ASME*, vol. 120, no. 2, pp. 85–95, 1998.

[69] K. S. Reddy and N. Sendhil Kumar, "Convection and surface radiation heat losses from modified cavity receiver of solar parabolic dish collector with two-stage concentration", *Heat Mass Transf.*, vol. 45, no. 3, pp. 363–373, 2008.

[70] F. Cui, Y. He, Z. Cheng and Y. Li, "Study on combined heat loss of a dish receiver with quartz glass cover", *Appl. Energy*, vol. 112, pp. 690–696, 2013.

[71] M. J. Montes, A. Rovira, J. M. Martínez-Val and A. Ramos, "Proposal of a fluid flow layout to improve the heat transfer in the active absorber surface of solar central cavity receivers", *Appl. Therm. Eng.*, vol. 35, pp. 220–232,. 2011.

[72] I. Hischier, D. Hess, W. Lipiński, M. Modest and A. Steinfeld, "Heat transfer analysis of a novel pressurized air receiver for concentrated solar power via combined cycles", *J. Therm. Sci. Eng. Appl.*, pp. 1–041002–1, 2010.

[73] N. Boerema, G. Morrison, R. Taylor and G. Rosengarten, "Liquid sodium versus Hitec as a heat transfer fluid in solar thermal central receiver systems", *Sol. Energy*, vol. 86, no. 9, pp. 2293–2305, 2012.

[74] M. Behnia, J. A. Reizes and G. De Vahl Davis, "Combined radiation and natural convection in a rectangular cavity with a transparent wall and containing a non-participating fluid", vol. 10, no. 3, pp. 305–325, 1990.

[75] J. Leibfried and U. Ortjohann, "Convective heat loss from upward and downward-facing cavity solar receivers: measurements and calculations", *Sol. Energy Eng.*, vol. 117, no. 2, pp. 75–84, 1995.

[76] C. Stine, W. B. McDonald, "Cavity receiver convective heat-loss", *Congress of the International Solar Energy Soc: Clean and Safe Energy Forever*, pp. 1318–1322, 1989.

[77] J. B. Fang, N. Tu and J. J. Wei, "Numerical investigation of start-up performance of a solar cavity receiver", *Renew. Energy*, vol. 53, pp. 35–42, 2013.

[78] R. Ben-Zvi, M. Epstein and A. Segal, "Simulation of an integrated steam generator for solar tower", *Sol. Energy*, vol. 86, no. 1, pp. 578–592, 2012.

[79] M. Neber and H. Lee, "Design of a high temperature cavity receiver for residential scale concentrated solar power", *Energy*, vol. 47, no. 1, pp. 481–487, 2012.

[80] N. Tu, J. Wei and J. Fang, "Numerical study on thermal performance of a solar cavity receiver with different depths", *Appl. Therm. Eng.*, 2014.

[81] F. Q. Cui, Y. L. He, Z. D. Cheng and Y-S. Li, "Modeling of the dish receiver with the effect of inhomogeneous radiation flux distribution", *Heat Transf. Eng.*, vol. 35, no. 6–8, pp. 780–790, 2014.

[82] L. W. F. Zhilin, Z. Yaoming, L. Deyou, W. Jun, "Discussion of mechanical design for pressured cavity-air-receiver in solar power tower system", *Proceedings of ISES World Congress*, pp. 1869–72, 2007.

[83] Q. Yu, Z. Wang and E. Xu, "Simulation and analysis of the central cavity receiver's performance of solar thermal power tower plant", *Sol. Energy*, vol. 86, no. 1, pp. 164–174, 2012.

[84] J. B. Fang, J. J. Wei, X. W. Dong and Y. S. Wang, "Thermal performance simulation of a solar cavity receiver under windy conditions", *Sol. Energy*, vol. 85, no. 1, pp. 126–138, 2011.

[85] A. Bejan and D. Kraus Allan, *Heat Transfer Handbook*. Wiley, 2003.

[86] J. Holman, *Heat Transfer*. McGraw Hill, 2001.

[87] Y. A. Cengel, *Heat Transfer*, 2nd ed.. McGraw-Hill, 2003.

[88] K. A. S. Abdulmaged, "The Interaction between radiation and turbulent natural convection in square and rectangular enclosures", University of Sheffield, 2013.

[89] Y. A. Cengel, *Heat Tansfer- Practical Approach*, 2nd ed.. McGraw-Hill, 2002.

[90] CD-adapco, "STAR CCM+ user guide", 2012.

[91] Y. L. He, W. Q. Tao, T. S. Zhao and Z. Q. Chen, "Steady natural convection in a tilted long cylindrical envelope with lateral adiabatic surface, Part 1: theoretical modeling and numerical treatments", *Numer. Heat Transf.*, no. 50276046, pp. 375–397, 2003.

[92] A. I. Zografos, W. A. Martin and J. E. Sunderland, "Equations of properties as a function of temperature for seven fluids", *Comput. Methods Appl. Mech. Eng.*, vol. 61, no. 2, pp. 177–187, 1987.

[93] J. Siegel and R. Howel, *Thermal Radiation Heat Transfer*, 3rd ed.. Hemisphere Publishing, 1992.

[94] H. K. Versteeg and W. Malalasekra., *An introduction to computational-fluid-dynamics*, 2nd ed.. Prentice Hall, 2007.

[95] N. Chase, M. Rademacher, E. Goodman, R. Averill and R. Sidhu, "A benchmark study of optimization search algorithms", pp. 1–15, 2010.

[96] Red Cedar Technology, "Hierarchical Evolutionary Engineering Design System (HEEDS). Getting Started Manual", 2011.

[97] A. M. Clausing, "Convective Losses from cavity solar receivers – comparisons between analytical predictions and experimental results", *ASME J. Sol. Energy Eng.*, vol. 105, no. 1, pp. 29–33, 1983.

[98] W. G. Le Roux, T. Bello-Ochende and J. P. Meyer, "Operating conditions of an open and direct solar thermal Brayton cycle with optimised cavity receiver and recuperator", *Energy*, vol. 36, no. 10, pp. 6027–6036, 2011.

[99] W. G. Le Roux, T. Bello-Ochende and J. P. Meyer, "Optimum performance of the small-scale open and direct solar thermal Brayton cycle at various environmental conditions and constraints", *Energy*, vol. 46, no. 1, pp. 42–50, 2012.

[100] A. Mwesigye, T. Bello-Ochende and J. P. Meyer, "Numerical investigation of entropy generation in a parabolic trough receiver at different concentration ratios", *Energy*, vol. 53, pp. 114–127, 2013.

[101] J. M. Khubeiz, E. Radziemska, and W. M. Lewandowski, "Natural convective heat-transfers from an isothermal horizontal hemispherical cavity", *Appl. Energy*, vol. 73, no. 3–4, pp. 261–275, 2002.

[102] R. Bertocchi, J. Karni and A. Kribus, "Experimental evaluation of a non-isothermal high temperature solar particle receiver", *Energy*, vol. 29, no. 5–6, pp. 687–700, 2004.

[103] R. Ben-Zvi and J. Karni, "Simulation of a volumetric solar reformer", *J. Sol. Energy Eng.*, vol. 129, no. 2, p. 197, 2007.

[104] S. Shakerin, M. Bohn and R. I. Loehrke, "Natural convection in an enclosure with discrete roughness elements on a vertical heated wall", *Int. J. Heat Mass Transf.*, vol. 31, no. 7, pp. 1423–1430, 1988.

[105] R. L. Frederick, "Natural convection in an inclined square enclosure with a partition attached to its cold wall", *Int. J. Heat Mass Transf.*, vol. 32, no. 1, pp. 87–94, 1989.

[106] A. Nag, A. Sarkar and V. M. K. Sastri, "Natural convection in a differentially heated square cavity with a horizontal partition plate on the hot wall", *Comput. Methods Appl. Mech. Eng.*, vol. 110, no. 1–2, pp. 143–156, 1993.

[107] E. Bilgen, "Natural convection in cavities with a thin fin on the hot wall", *Int. J. Heat Mass Transf.*, vol. 48, no. 17, pp. 3493–3505, 2005.

[108] O. Polat and E. Bilgen, "Conjugate heat transfer in inclined open shallow cavities", *Int. J. Heat Mass Transf.*, vol. 46, no. 9, pp. 1563–1573, 2003.

[109] A. Muftuoglu and E. Bilgen, "Heat transfer in inclined rectangular receivers for concentrated solar radiation", *Int. Commun. Heat Mass Transf.*, vol. 35, no. 5, pp. 551–556, 2008.

[110] É. Fontana, A. Da Silva and V. C. Mariani, "Natural convection in a partially open square cavity with internal heat source: an analysis of the opening mass flow", *Int. J. Heat Mass Transf.*, vol. 54, no. 7–8, pp. 1369–1386, 2011.

[111] V. A. F. Costa, M. Oliveira and C. M. Sousa, "Control of laminar natural convection in differentially heated square enclosures using solid inserts at the corners", *Int. J. Heat Mass Transf.*, vol. 46, no. 18, pp. 3529–3537, 2003.

[112] A. K. Sharma, A. Pradeep, K. Velusamy, P. Chellapandi and B. Raj, "Interaction of natural convection flow in multiple open cavities formed due to horizontal fins", *Ann. Nucl. Energy*, vol. 38, no. 9, pp. 1906–1915, 2011.

[113] T. N. Anderson, M. Duke and J. K. Carson, "Suppression of natural convection heat transfer coefficients in an attic shaped enclosure", *Int. Commun. Heat Mass Transf.*, vol. 37, no. 8, pp. 984–986, 2010.

[114] S. A. Nada, "Natural convection heat transfer in horizontal and vertical closed narrow enclosures with heated rectangular finned base plate", *Int. J. Heat Mass Transf.*, vol. 50, no. 3–4, pp. 667–679, 2007.

[115] Y. Varol, H. F. Oztop and A. Varol, "Effects of thin fin on natural convection in porous triangular enclosures", *Int. J. Therm. Sci.*, vol. 46, no. 10, pp. 1033–1045, 2007.

[116] A. Ben-Nakhi and A. J. Chamkha, "Conjugate natural convection in a square enclosure with inclined thin fin of arbitrary length", *Int. J. Therm. Sci.*, vol. 46, no. 5, pp. 467–478, 2007.

[117] Y. Shiina, K. Fujimura, T. Kunugi, and N. Akino, "Natural convection in a hemispherical enclosure heated from below", *Int. J. Heat Mass Transf.*, vol. 37, no. 11, pp. 1605–1617, 1994.

[118] W. J. Kraus and A. Aziz, *Extended surface heat transfer*. Wiley, 2007.

[119] K. S. Reddy and N. Sendhil Kumar, "Convection and surface radiation heat losses from modified cavity receiver of solar parabolic dish collector with two-stage concentration", *Heat Mass Transf.*, vol. 45, no. 3, pp. 363–373, 2008.

[120] M. M. Gonzalez, J. H. Palafox and C. A. Estrada, "Numerical study of heat transfer by natural convection and surface thermal radiation in an open cavity receiver", *Sol. Energy*, vol. 86, no. 4, pp. 1118–1128, 2012.

[121] R. Rubin J. Karni and A. Kribus, "The 'porcupine': a novel high-flux absorber for volumetric solar receivers", *J. Sol. Energy Eng. ASME*, vol. 120, no. 2, pp. 85–95, 1998.

[122] F. Cui, Y. He, Z. Cheng and Y. Li, "Study on combined heat loss of a dish receiver with quartz glass cover", *Appl. Energy*, vol. 112, pp. 690–696, 2013.

[123] M. J. Montes, A. Rovira, J. M. Martínez-Val and A. Ramos, "Proposal of a fluid flow layout to improve the heat transfer in the active absorber surface of solar central cavity receivers", *Appl. Therm. Eng.*, vol. 35, pp. 220–232, 2011.

[124] A. Steinfeld and M. Schubnell, "Optimum aperture size and operating temperature of a solar cavity-receiver", *Sol. Energy*, vol. 50, no. 1, pp. 19–25, 1993.

[125] L. C. Ngo, T. Bello-Ochende and J. P. Meyer, "Numerical modelling and optimisation of natural convection heat loss suppression in a solar cavity receiver with plate fins", *Renew. Energy*, vol. 74, pp. 95–105, 2015.

Appendix A: Summary report of simulation of a receiver at 30 degrees with fins and temperature 1000K

Session Summary	
Date	04 Feb 2015 10:51:59 AM
Simulation	E:\StarCCM Simulations 2013\Simulations with fins\Temperature 1000K\Receiver_30_Degrees_with_fins_1000K.sim
File size	46 MB
Number of Partitions	1
Number of Restored Partitions	1
Software Summary	
Version	BuildArch: win64 BuildEnv: intel12.1-r8 ReleaseDate: Thu Jun 5 00:00:00 UTC 2014 ReleaseNumber: 9.04.009
Hardware Summary	
Hosts	Controller: dfc-jo7222-01.ad.uj.ac.za Number of Workers: 0

Simulation Properties

1 **Receiver_30_Degrees_with_fins_1000K**		
+-1 Filters		
+-2 Parts		
| `-1 **Body 2**	Metadata	{}
| |	Index	1
| |	Descriptions	[Ljava.lang.String;@5eb23d
| |	Face Count	12678
| +-1 Surfaces		
| | +-1 **Aperture inner surface**	Metadata	{}
| | +-2 **Aperture inner surface with fins**	Metadata	{}
| | +-3 **Aperture outer surface**	Metadata	{}
| | +-4 **Aperture thickness**	Metadata	{}
| | +-5 **Atmosphere**	Metadata	{}
| | +-6 **Receiver inner surface**	Metadata	{}
| | `-7 **Receiver outer surface**	Metadata	{}
| `-2 Curves		
| `-1 **Default**		

+-3 3D-CAD Models		
| `-1 **3D-CAD Model 1**		
+-4 Tags		
+-5 Operations		
+-6 Descriptions	Number of Children	2
| +-1 Root	Described Parts	Body 2
| `-2 Latest	Described Parts	Body 2
|	Faces	12678
|	Vertices	6343
+-7 Contacts		
+-8 Continua	Continua	2
| +-1 **Mesh 1**	Regions	[Region 1]
| | |	Interfaces	[]
| | |	Interpolation Option	Nearest neighbor
| | +-1 Models		
| | | +-1 Polyhedral Mesher	Enable Mesh Expansion Control	true
| | | |	Run Optimizer	true
| | | |	Include Refinement	true
| | | |	Optimization Cycles	1
| | | |	Quality Threshold	0.4
| | | +-2 Prism Layer Mesher	Stretching Function	Geometric Progression
| | | |	Stretching Mode	Stretch Factor
| | | |	Gap Fill Percentage	25.0
| | | |	Minimum Thickness Percentage	10.0
| | | |	Layer Reduction Percentage	50.0
| | | |	Boundary March Angle	50.0
| | | |	Concave Angle Limit	0.0
| | | |	Convex Angle Limit	360.0
| | | |	Near Core Layer Aspect Ratio	0.0
| | | |	Improve Subsurface Quality	true
| | | `-3 Surface Remesher	Do Curvature Refinement	true
| | |	Do Proximity Refinement	true
| | |	Do Compatibility Refinement	false
| | |	Retain Geometric Features	true
| | |	Create Aligned Meshes	true
| | |	Minimum Face Quality	0.05
| | |	Enable Automatic Surface Repair	true
| | +-2 Reference Values		
| | | +-1 Base Size	Value	0.08 m
| | | +-2 Automatic Surface Repair	Connected Surface Count Limit	None
| | | | |	Connected Surface Size Limits	None

| | | | +-1 Minimum Proximity	Minimum Proximity	0.05
| | | | `-2 Minimum Quality	Minimum Quality	0.01
| | | +-3 CAD Projection	Project to CAD	true
| | | +-4 Number of Prism Layers	Number of Prism Layers	4
| | | +-5 Prism Layer Stretching	Prism Layer Stretching	1.5
| | | +-6 Prism Layer Thickness	Size Type	Relative to base
| | | | `-1 Relative Size	Percentage of Base	4.0
| | | |	Absolute Size	0.0032 m
| | | +-7 Refinement Level	Refinement Level	1
| | | +-8 Surface Curvature	Enable Curvature Deviation Distance	false
| | | | `-1 Basic Curvature	# Pts/circle	36.0
| | | +-9 Surface Growth Rate	Surface Growth Rate	1.3
| | | +-10 Surface Proximity	Search Floor	0.0 m
| | | |	# Points in gap	2.0
| | | |	Enable Search Ceiling	false
| | | +-11 Surface Size	Relative/Absolute	Relative to base
| | | | |	Size Method	Min and Target
| | | | +-1 Relative Minimum Size	Percentage of Base	5.0
| | | | |	Absolute Size	0.004 m
| | | | `-2 Relative Target Size	Percentage of Base	35.0
| | | |	Absolute Size	0.028000000000000004 m
| | | +-12 Tet/Poly Density	Density	1.0
| | | |	Growth Factor	1.0
| | | +-13 Tet/Poly Expansion Max Cell Size	Size Type	Relative to base
| | | | `-1 Relative Size	Percentage of Base	200.0
| | | |	Absolute Size	0.16 m
| | | +-14 Tet/Poly Expansion Rate	Expansion Rate	1.5
| | | `-15 Tet/Poly Volume Blending	Blending Factor	1.0
| | `-3 Volumetric Controls		
| `-2 **Physics 1**	Regions	[Region 1]
| |	Interfaces	[]
| +-1 Models		
| | +-1 Cell Quality Remediation		
| | +-2 Gas		
| | | `-1 **Air**	Database Material	Air (Air) [Standard/Gases]
| | | `-1 Material Properties		
| | | +-1 Dynamic Viscosity	Method	Polynomial in T
| | | +-2 Polynomial Density	Method	Polynomial in T
| | | | `-1 Polynomial in T	Polynomial	[4][150.0, 1000.0][3.650770719734535, -0.012366426160457, 1.648713418E-5, -7.499189E-9][0.0, 1.0, 2.0, 3.0][K][kg/m^3]
| | | +-3 Specific Heat	Method	Polynomial in T
| | | | `-1 Polynomial in T	Polynomial	[5][250.0, 1000.0][1034.09, -0.284887, 7.816818E-4, -4.970786E-7, 1.077024E-10][0.0, 1.0, 2.0, 3.0, 4.0][K][J/kg-K]
| | | +-4 Standard State Temperature	Method	Constant
| | | | `-1 Constant	Value	298.15 K

| || `-5 Thermal Conductivity	Method	Constant
| || `-1 Polynomial	Method	Polynomial in T
| +-3 Gradients	Gradient Method	Hybrid Gauss-LSQ
| ||	Limiter Method	Venkatakrishnan
| ||	Custom Accuracy Level Selector	2.0
| ||	Verbose	false
| ||	Least-Squares Quality Criterion	true
| ||	Flat Cells Curvature Criterion	true
| ||	Cell Skewness Criterion	true
| ||	Chevron-Cell Criterion	true
| ||	Least-Squares Tensor Minimum Eigenvalues Ratio	0.1
| ||	Normalized Flat Cells Curvature Factor	1.0
| ||	Maximum Safe (Positive) Skewness Angle (deg)	75.0
| ||	Minimum Unsafe (Positive) Skewness Angle (deg)	88.0
| ||	Use TVB Gradient Limiting	false
| ||	Acceptable Field Variation (Factor)	0.05
| +-4 Gravity		
| +-5 Laminar		
| +-6 Polynomial Density		
| +-7 Segregated Flow	Minimum Absolute Pressure	1000.0 Pa
| ||	Flow Boundary Diffusion	true
| ||	Unsteady Flux Dissipation Corrections	false
| ||	Limit Acoustic-CFL Option	Per-Model
| ||	Secondary Gradients	On
| ||	Convection	2nd-order
| ||	Delta-V Dissipation	Off
| +-8 Segregated Fluid Temperature	Secondary Gradients	On
| ||	Convection	2nd-order
| ||	Flow Boundary Diffusion	true
| +-9 Steady		
| `-10 Three Dimensional		
+-2 Reference Values		
| +-1 Gravity	Value	[0.0, - 3.4345, 0.0]
| +-2 Reference Altitude	Value	[0.0, 0.0, 0.0] m
| +-3 Reference Density	Value	1.222206844797435 kg/m^3
| +-4 Minimum Allowable Temperature	Value	100.0 K
| +-5 Maximum Allowable Temperature	Value	5000.0 K

| | `-6 Reference Pressure	Value	101325.0 Pa
| `-3 Initial Conditions		
| +-1 Pressure	Method	Constant
| | `-1 Constant	Value	0.0 Pa
| +-2 Static Temperature	Method	Constant
| | `-1 Constant	Value	300.0 K
| `-3 Velocity	Method	Constant
| |	Coordinate System	Laboratory
| `-1 Constant	Value	[0.0, 0.0, 0.0] m/s
+-9 Regions	Regions	1
| `-1 **Region 1**	Index	0
| |	Mesh Continuum	Mesh 1
| |	Physics Continuum	Physics 1
| |	Type	Fluid Region
| +-1 Boundaries	Boundaries	7
| | +-1 **Body 2.Aperture inner surface**	Index	11
| | | |	Interfaces	
| | | |	Type	Wall
| | | +-1 Mesh Conditions		
| | | | +-1 Custom Surface Curvature	Custom Curvature	Use Continuum Values
| | | | +-2 Custom Surface Proximity	Custom Proximity	Use Continuum Values
| | | | +-3 Custom Surface Size	Custom Surface Size	Disabled
| | | | +-4 Customize Prism Mesh	Customize Prism Mesh	Use Default Values
| | | | `-5 Customize Surface Remeshing	Disable Surface Remeshing	Disabled
| | | +-2 Physics Conditions		
| | | | +-1 Shear Stress Specification	Method	No-Slip
| | | | +-2 Tangential Velocity Specification	Method	None
| | | | |	Reference Frame	Relative To Mesh
| | | | +-3 Thermal Specification	Condition	Temperature
| | | | `-4 User Wall Heat Flux Coefficient Specification	Method	None
| | | `-3 Physics Values		
| | | `-1 Static Temperature	Method	Constant
| | | `-1 Constant	Value	1000.0 K
| | +-2 **Body 2.Aperture inner surface with fins**	Index	13
| | | |	Interfaces	
| | | |	Type	Wall
| | | +-1 Mesh Conditions		
| | | | +-1 Custom Surface Curvature	Custom Curvature	Use Continuum Values
| | | | +-2 Custom Surface Proximity	Custom Proximity	Use Continuum Values
| | | | +-3 Custom Surface Size	Custom Surface Size	Disabled
| | | | +-4 Customize Prism Mesh	Customize Prism Mesh	Use Default Values
| | | | `-5 Customize Surface Remeshing	Disable Surface Remeshing	Disabled
| | | +-2 Physics Conditions		
| | | | +-1 Shear Stress Specification	Method	No-Slip
| | | | +-2 Tangential Velocity Specification	Method	None
| | | | |	Reference Frame	Relative To Mesh
| | | | +-3 Thermal Specification	Condition	Temperature
| | | | `-4 User Wall Heat Flux Coefficient Specification	Method	None

| | \`-3 Physics Values		
| | \`-1 Static Temperature	Method	Constant
| | \`-1 Constant	Value	1000.0 K
| +-3 **Body 2.Aperture outer surface**	Index	9
| | |	Interfaces	
| | |	Type	Wall
| | +-1 Mesh Conditions		
| | | +-1 Custom Surface Curvature	Custom Curvature	Use Continuum Values
| | | +-2 Custom Surface Proximity	Custom Proximity	Use Continuum Values
| | | +-3 Custom Surface Size	Custom Surface Size	Disabled
| | | +-4 Customize Prism Mesh	Customize Prism Mesh	Use Default Values
| | | \`-5 Customize Surface Remeshing	Disable Surface Remeshing	Disabled
| | +-2 Physics Conditions		
| | | +-1 Shear Stress Specification	Method	No-Slip
| | | +-2 Tangential Velocity Specification	Method	None
| | | |	Reference Frame	Relative To Mesh
| | | +-3 Thermal Specification	Condition	Temperature
| | | \`-4 User Wall Heat Flux Coefficient Specification	Method	None
| | \`-3 Physics Values		
| | \`-1 Static Temperature	Method	Constant
| | \`-1 Constant	Value	1000.0 K
| +-4 **Body 2.Aperture thickness**	Index	10
| | |	Interfaces	
| | |	Type	Wall
| | +-1 Mesh Conditions		
| | | +-1 Custom Surface Curvature	Custom Curvature	Use Continuum Values
| | | +-2 Custom Surface Proximity	Custom Proximity	Use Continuum Values
| | | +-3 Custom Surface Size	Custom Surface Size	Disabled
| | | +-4 Customize Prism Mesh	Customize Prism Mesh	Use Default Values
| | | \`-5 Customize Surface Remeshing	Disable Surface Remeshing	Disabled
| | +-2 Physics Conditions		
| | | +-1 Shear Stress Specification	Method	No-Slip
| | | +-2 Tangential Velocity Specification	Method	None
| | | |	Reference Frame	Relative To Mesh
| | | +-3 Thermal Specification	Condition	Temperature
| | | \`-4 User Wall Heat Flux Coefficient Specification	Method	None
| | \`-3 Physics Values		
| | \`-1 Static Temperature	Method	Constant
| | \`-1 Constant	Value	1000.0 K
| +-5 **Body 2.Atmosphere**	Index	7
| | |	Interfaces	
| | |	Type	Pressure Outlet
| | +-1 Mesh Conditions		
| | | +-1 Custom Surface Curvature	Custom Curvature	Use Continuum Values
| | | +-2 Custom Surface Proximity	Custom Proximity	Use Continuum Values
| | | +-3 Custom Surface Size	Custom Surface Size	Enabled
| | | +-4 Customize Prism Mesh	Customize Prism Mesh	Use Default Values
| | | \`-5 Customize Surface Remeshing	Disable Surface Remeshing	Disabled

| | +-2 Mesh Values		
| | | `-1 Surface Size	Relative/Absolute	Relative to base
| | | |	Size Method	Min and Target
| | | +-1 Relative Minimum Size	Percentage of Base	25.0
| | | |	Absolute Size	0.02 m
| | | `-2 Relative Target Size	Percentage of Base	200.0
| | |	Absolute Size	0.16 m
| | +-3 Physics Conditions		
| | | +-1 Backflow Direction Specification	Method	Boundary-Normal
| | | +-2 Pressure Jump Option	Option	None
| | | +-3 Pressure Specification	Pressure Specification	Environmental
| | | +-4 Reference Frame Specification	Option	Lab Frame
| | | `-5 Target Mass Flow Option	Target Mass Flow Option	Disabled
| | `-4 Physics Values		
| | +-1 Pressure	Method	Constant
| | | `-1 Constant	Value	0.0 Pa
| | `-2 Static Temperature	Method	Constant
| | `-1 Constant	Value	300.0 K
| +-6 **Body 2.Receiver inner surface**	Index	12
| | |	Interfaces	
| | |	Type	Wall
| | +-1 Mesh Conditions		
| | | +-1 Custom Surface Curvature	Custom Curvature	Use Continuum Values
| | | +-2 Custom Surface Proximity	Custom Proximity	Use Continuum Values
| | | +-3 Custom Surface Size	Custom Surface Size	Disabled
| | | +-4 Customize Prism Mesh	Customize Prism Mesh	Use Default Values
| | | `-5 Customize Surface Remeshing	Disable Surface Remeshing	Disabled
| | +-2 Physics Conditions		
| | | +-1 Shear Stress Specification	Method	No-Slip
| | | +-2 Tangential Velocity Specification	Method	None
| | | |	Reference Frame	Relative To Mesh
| | | +-3 Thermal Specification	Condition	Temperature
| | | `-4 User Wall Heat Flux Coefficient Specification	Method	None
| | `-3 Physics Values		
| | `-1 Static Temperature	Method	Constant
| | `-1 Constant	Value	1000.0 K
| `-7 **Body 2.Receiver outer surface**	Index	8
| | |	Interfaces	
| | |	Type	Wall
| | +-1 Mesh Conditions		
| | | +-1 Custom Surface Curvature	Custom Curvature	Use Continuum Values
| | | +-2 Custom Surface Proximity	Custom Proximity	Use Continuum Values
| | | +-3 Custom Surface Size	Custom Surface Size	Disabled
| | | +-4 Customize Prism Mesh	Customize Prism Mesh	Use Default Values
| | | `-5 Customize Surface Remeshing	Disable Surface Remeshing	Disabled
| | `-2 Physics Conditions		
| | +-1 Shear Stress Specification	Method	No-Slip
| | +-2 Tangential Velocity Specification	Method	None
| | |	Reference Frame	Relative To Mesh

| | +-3 Thermal Specification	Condition	Adiabatic
| | `-4 User Wall Heat Flux Coefficient Specification	Method	None
| +-2 Feature Curves	Feature Curves	1
| |`-1 **Default Feature Curve**		
| | `-1 Mesh Conditions		
| | `-1 Custom Surface Size	Custom Surface Size	Disabled
| +-3 Mesh Conditions		
| |+-1 Customize Prism Mesh	Customize Prism Mesh	Use Default Values
| |+-2 Customize Tet/Poly Density	Customize Tet/Poly Density	Disabled
| |`-3 Customize Tet/Poly Expansion	Customize Tet/Poly Expansion	Disabled
| +-4 Physics Conditions		
| |+-1 Energy Source Option	Energy Source Option	None
| |+-2 Initial Condition Option	Option	Use Continuum Values
| |+-3 Mass Source Option	Mass Source Option	Disabled
| |`-4 Momentum Source Option	Momentum Source Option	None
| `-5 Physics Values		
| +-1 Axis	Coordinate System	Laboratory
| |	Origin	[0.0, 0.0, 0.0] m
| |	Direction	[0.0, 0.0, 1.0]
| `-2 Motion Specification	Motion	Stationary
|	Reference Frame	Lab Reference Frame
+-10 Derived Parts	Derived Parts	1
| `-1 **plane section**	Origin	[0.0, 0.0, 0.0] m,m,m
| |	Coordinate System	Laboratory
| |	Normal	[0.0, 0.0, 1.0] m,m,m
| |	Section Mode	Single Section
| |	Displayed Index	-1
| `-1 Single section	Offset	0.0 m
+-11 Solvers		
| +-1 Partitioning	Solver Frozen	false
| |	Partitioning Method	Per-Region
| +-2 Segregated Flow	Solver Frozen	false
| | |	Reconstruction Frozen	false
| | |	Reconstruction Zeroed	false
| | |	Temporary Storage Retained	false
| | |	Continuity Initialization	false
| | +-1 Velocity	Under-Relaxation Factor	0.7
| | | |	Dynamic Local Under-Relaxation	false
| | | +-1 Under-Relaxation Factor Ramp	Ramp Method	No Ramp
| | | `-2 AMG Linear Solver	Max Cycles	30
| | | |	Verbosity	None
| | | |	Parallel Migration Limit	25
| | | |	Subdomain Coarsening Enabled	true

| | | |	Enable Direct Solver	false
| | | |	Maximum Direct Solver Equations	32
| | | |	Convergence Tolerance	0.1
| | | |	Epsilon	0.0
| | | |	Cycle Type	Flex Cycle
| | | |	Group Size Control	Auto
| | | |	Group Size	4
| | | |	Relaxation Scheme	Gauss-Seidel
| | | |	Acceleration Method	None
| | | |	Scaling	Disabled
| | | `-1 Flex Cycle	Restriction Tolerance	0.9
| | |	Prolongation Tolerance	0.5
| | |	Sweeps	1
| | `-2 Pressure	Under-Relaxation Factor	0.3
| | |	Pressure Reference Location	Automatic Selection
| | +-1 Under-Relaxation Factor Ramp	Ramp Method	No Ramp
| | `-2 AMG Linear Solver	Max Cycles	30
| | |	Verbosity	None
| | |	Parallel Migration Limit	25
| | |	Subdomain Coarsening Enabled	true
| | |	Enable Direct Solver	false
| | |	Maximum Direct Solver Equations	32
| | |	Convergence Tolerance	0.1
| | |	Epsilon	0.0
| | |	Cycle Type	V Cycle
| | |	Group Size Control	Auto
| | |	Group Size	4
| | |	Relaxation Scheme	Gauss-Seidel
| | |	Acceleration Method	Conjugate Gradient
| | |	Scaling	Auto
| | `-1 V Cycle	Pre-Sweeps	1
| |	Post-Sweeps	1
| |	Max Levels	50
| `-3 Segregated Energy	Solver Frozen	false
| |	Fluid Under-Relaxation Factor	0.8
| |	Solid Under-Relaxation Factor	0.99
| +-1 Fluid Under-Relaxation Factor Ramp	Ramp Method	No Ramp
| +-2 Solid Under-Relaxation Factor Ramp	Ramp Method	No Ramp
| `-3 AMG Linear Solver	Max Cycles	30
| |	Verbosity	None
| |	Parallel Migration Limit	25
| |	Subdomain Coarsening Enabled	true
| |	Enable Direct Solver	false

| |	Maximum Direct Solver Equations	32
| |	Convergence Tolerance	0.1
| |	Epsilon	0.0
| |	Cycle Type	V Cycle
| |	Group Size Control	Auto
| |	Group Size	4
| |	Relaxation Scheme	Gauss-Seidel
| |	Acceleration Method	None
| |	Scaling	Disabled
| `-1 V Cycle	Pre-Sweeps	1
|	Post-Sweeps	1
|	Max Levels	50
+-12 Stopping Criteria		
| +-1 **Energy Criterion**	Enabled	true
| | |	Criterion Option	Minimum
| | |	Logical Rule	And
| | |	Stop Inner Iterations	true
| | |	Stop Outer Iterations	false
| | |	Criterion Satisfied	false
| | `-1 Minimum Limit	Minimum Value	1.0E-6
| +-2 **Maximum Steps**	Enabled	true
| |	Maximum Steps	1000
| |	Logical Rule	And
| |	Criterion Satisfied	true
| `-3 **Stop File**	Enabled	true
|	Stop Inner Iterations	true
|	Path	ABORT
|	Logical Rule	Or
|	Criterion Satisfied	false
+-13 Solution Histories		
+-14 Solution Views		
| `-1 **Current Solution**	Iteration	1015
|	Time Step	0
|	Solution Time	0.0
+-15 Reports	Reports	2
| +-1 **Heat Transfer 1**	Units	W
| |	Representation	Volume Mesh
| `-2 **Nusselt number**	Units	
|	Representation	Volume Mesh
|	Smooth Values	false
+-16 Monitors	Monitors	10
| |	Monitors To Print	[Energy, Z-momentum, Y-momentum, X-momentum, Continuity, Heat Transfer 1 Monitor]
| |	Output Direction	Horizontal
| |	Heading Print Frequency	10
| +-1 **Heat Transfer 1 Monitor**	Report	Heat Transfer 1
| | |	Enabled	true
| | |	Trigger	Iteration
| | |	Normalization Option	Off

| | |	Maximum Plot Samples	5000
| | `-1 Iteration Frequency	Iteration Frequency	1
| |	Start Iteration	0
| |	Enable Stop	false
| |	Stop Iteration	0
| +-2 **Iteration**	Maximum Plot Samples	5000
| +-3 **Physical Time**	Maximum Plot Samples	5000
+-17 Representations		
| +-1 **Geometry**		
| | `-1 **Latest**		
| +-2 **Initial Surface**	Faces	12678
| | |	Edges	644
| | `-1 Regions		
| | `-1 Region 1	Faces	12678
| | |	Edges	644
| | +-1 Boundaries		
| | | +-1 Body 2.Aperture inner surface	Faces	92
| | | +-2 Body 2.Aperture inner surface with fins	Faces	1012
| | | +-3 Body 2.Aperture outer surface	Faces	92
| | | +-4 Body 2.Aperture thickness	Faces	92
| | | +-5 Body 2.Atmosphere	Faces	9408
| | | +-6 Body 2.Receiver inner surface	Faces	946
| | | `-7 Body 2.Receiver outer surface	Faces	1036
| | `-2 Feature Curves		
| | `-1 Default Feature Curve	Edges	644
| +-3 **Remeshed Surface**	Faces	6828
| | |	Edges	1210
| | `-1 Regions		
| | `-1 Region 1	Faces	6828
| | |	Edges	1210
| | +-1 Boundaries		
| | | +-1 Body 2.Aperture inner surface	Faces	131
| | | +-2 Body 2.Aperture inner surface with fins	Faces	2532
| | | +-3 Body 2.Aperture outer surface	Faces	386
| | | +-4 Body 2.Aperture thickness	Faces	179
| | | +-5 Body 2.Atmosphere	Faces	1338
| | | +-6 Body 2.Receiver inner surface	Faces	1614
| | | `-7 Body 2.Receiver outer surface	Faces	648
| | `-2 Feature Curves		
| | `-1 Default Feature Curve	Edges	1210
| `-4 **Volume Mesh**	Cells	320203
| |	Interior Faces	723176
| |	Vertices	426422
| +-1 Finite Volume Regions		
| | `-1 Region 1	Cells	320203
| | |	Interior Faces	723176
| | |	Vertices	426422
| | `-1 Finite Volume Boundaries		
| | +-1 Body 2.Aperture inner surface	Faces	393

| | +-2 Body 2.Aperture inner surface with fins	Faces	7088
| | +-3 Body 2.Aperture outer surface	Faces	860
| | +-4 Body 2.Aperture thickness	Faces	447
| | +-5 Body 2.Atmosphere	Faces	2707
| | +-6 Body 2.Receiver inner surface	Faces	3363
| | `-7 Body 2.Receiver outer surface	Faces	1341

Solution

Accumulated CPU Time over all processes (s)	80473.98199999977
Elapsed Time (s)	80473.9749999998
Iterations	1015